

ATOMISTIC SIMULATIONS OF THERMAL TRANSPORT ACROSS  
INTERFACES

A Dissertation

Submitted to the Faculty

of

Purdue University

by

Jingjing Shi

In Partial Fulfillment of the

Requirements for the Degree

of

Doctor of Philosophy

December 2018

Purdue University

West Lafayette, Indiana

**THE PURDUE UNIVERSITY GRADUATE SCHOOL**  
**STATEMENT OF DISSERTATION APPROVAL**

Dr. Xiulin Ruan, Co-Chair

School of Mechanical Engineering

Dr. Timothy S. Fisher, Co-Chair

School of Mechanical Engineering

Dr. Gerhard Klimeck

School of Electrical and Computer Engineering

Dr. Ajit K. Roy

School of Mechanical Engineering

**Approved by:**

Dr. Jay P. Gore

Head of the School Graduate Program

## ACKNOWLEDGMENTS

I'm very grateful to my advisor Professor Xiulin Ruan and Professor Timothy S. Fisher for their patience, guidance, knowledge and insight. My time at Purdue is great with their countless help, and I have learned a lot from them. The other members of my committee, Prof. Gerhard Klimeck and Dr. Ajit Roy, have provided support and helpful advice during my research process. I also would like to thank Prof. Mark Lunstrom, Prof. Supriyo Datta, and Prof. Paul Muzikar, I benefited a lot from their courses and books.

Dr. Jonghoon Lee helped me a lot to successfully apply the wave packet method on carbon nanotube, and kindly hosted me a visit to Dayton, OH. Dr. Vikas Varshney gave me some helpful suggestions with the construction of turning carbon nanotube. I would like to thank Dr. Tillmann Kubis for his help during our collaboration, and I benefited a lot from the discussion with him. I also enjoyed the collaboration with Yuanchen Chu and Kai Miao, from whom I learned about the nonequilibrium Green's function method. I want to express my sincere appreciation to former Purdue students Yan Wang, Yalin Dong, Rajib Paul, Bo Qiu, Liangliang Chen for their countless help. Yan Wang and Lei Cao offered me a lot of good advice in both career and life. In addition, I have met a lot of great people at Purdue and received much help from them, I would like to acknowledge Tianli Feng, Zexi Lu, Xiangyu Li, Xiaolong Yang, Zuyuan Wang, Yang Zhong, Xintong Xu, Prabudhya Roychowdhury, Dedeepya Valluripally, Wenjun Yao and Yixiu Luo. I am very lucky to work with all of them.

Last but not the least, I would like to thank my parents and my husband for their love and support. During my PhD life, every time I have difficulties or stress, they offered unconditional support. The encouragement from my family keeps me going and gives me confidence.

## TABLE OF CONTENTS

	Page
LIST OF TABLES . . . . .	vi
LIST OF FIGURES . . . . .	vii
ABSTRACT . . . . .	xii
1. INTRODUCTION . . . . .	1
1.1 Motivation . . . . .	1
1.2 Thermal Transport in CNT-graphene Networks . . . . .	7
1.3 Methodology . . . . .	8
1.3.1 Classical Molecular Dynamics . . . . .	8
1.3.2 Landauer Approach . . . . .	9
1.4 Objective and Organization . . . . .	11
2. THERMAL TRANSPORT ACROSS CNT-GRAPHENE COVALENT AND VAN DER WAALS JUNCTIONS . . . . .	13
2.1 Introduction . . . . .	13
2.2 MD SIMULATION METHOD . . . . .	15
2.3 RESULTS AND DISCUSSION . . . . .	17
2.3.1 Temperature Distribution and Junction Resistance . . . . .	17
2.3.2 Decomposition of the Junction Resistance . . . . .	21
2.3.3 Phonon Density of States . . . . .	24
2.3.4 Network Model . . . . .	27
2.4 Summary . . . . .	29
3. DECOMPOSITION OF THERMAL BOUNDARY RESISTANCE ACROSS CARBON NANOTUBE-GRAPHENE JUNCTIONS . . . . .	31
3.1 Introduction . . . . .	31
3.2 Methodology . . . . .	33
3.3 Results and discussion . . . . .	36
3.3.1 Junction resistance of different interfaces . . . . .	36
3.3.2 Error analysis . . . . .	38
3.3.3 Relation between resistance and the number of defects . . . . .	39
3.3.4 Relation between resistance and turning angle . . . . .	43
3.4 Conclusion . . . . .	45
4. PHONON POLARIZATION CONVERSION ACROSS DIMENSIONALLY MISMATCHED INTERFACES: CARBON NANOTUBE-GRAPHENE JUNC- TION . . . . .	46

	Page
4.1 Introduction . . . . .	46
4.2 Methodology . . . . .	47
4.3 Results and Discussion . . . . .	52
4.4 Summary . . . . .	64
5. NONEQUILIBRIUM LANDAUER APPROACH FOR THERMAL INTER- FACES . . . . .	65
5.1 Introduction . . . . .	65
5.2 Failure of the conventional Landauer approach on the CNT-graphene Junction . . . . .	67
5.3 Si/heavy-Si interface . . . . .	78
5.4 The nonequilibrium Landauer approach . . . . .	81
5.4.1 The nonequilibrium Landauer approach at Si/heavy-Si interface	81
5.4.2 The nonequilibrium Landauer approach at CNT-graphene junction	86
5.4.3 A chart to estimate the TBC correction . . . . .	89
5.5 Comparison with Experiments . . . . .	90
5.6 Summary . . . . .	92
6. SUMMARY . . . . .	93
REFERENCES . . . . .	96
VITA . . . . .	105

## LIST OF TABLES

Table	Page
3.1 The interface thermal resistance results from NEMD of different interfaces.	38
3.2 The NEMD interface thermal resistance results of different number of defects.	43
4.1 The CNT-graphene interface thermal conductance results predicted from Landauer approach with transmission functions from wave packet (WP) method (without and with polarization conversion) and AMM of incident LA, TA, TW, and RB branches. . . . .	62

## LIST OF FIGURES

Figure	Page
1.1 For the past five decades, the number of transistors per microprocessor chip a rough measure of processing power has doubled about every two years, in step with Moores law. [5] . . . . .	3
1.2 Thermal properties of carbon allotropes and their derivatives. [13] Top: Diagram based on average values reported in literature. The axis is not to scale. Bottom: Thermal conductivity of bulk carbon allotropes as a function of T. . . . .	4
1.3 (a) phonons transport between 1D material and 2D material; (b) phonons transport between 1D material and 3D material (1D material is perpendicular to 3D material); (c) phonons transport between 1D material and 3D material (1D material is parallel to 3D material); (d) phonons transport between 2D material and 3D material. . . . .	5
1.4 The pillared graphene network structure with $sp^2$ covalent bonds at junctions. . . . .	6
2.1 (a) The pillared graphene structure with $sp^2$ covalent bonds at junctions. (b) Schematic of the network model. Intrinsic thermal resistances of CNTs and graphene are neglected; then the system can be simplified as junction resistances in parallel and series networks. (c) The small pillared graphene cell of the simulation domain. Periodic boundary conditions are applied in $x$ and $y$ directions, while fixed boundary conditions are applied in the $z$ direction. The three important geometric parameters are pillar length ( $PL$ ), minimum inter-pillar distance ( $MIPD$ ) and the distance from the junction to the thermal reservoir (or reservoir distance, $RD$ ). Four important regions are the CNT center region, CNT interfacial region, graphene interfacial region, and graphene bulk. These regions are defined because they have different LDOS, and the details are given in sections III.B and III.C. . . . .	14

Figure	Page	
2.2	A typical temperature profile of two graphene sheets and the CNT pillar in between with $sp^2$ junctions. The temperature jump at the junction can be decomposed into three components. As a result, the junction resistance $R_j$ can be decomposed into: boundary resistance $R_B$ , CNT interfacial region resistance $R_{\text{CNT,IR}}$ , and the graphene interfacial region resistance $R_{\text{gra,IR}}$ . The decomposition details are discussed starting section III.B. Here IR means interfacial regions. . . . .	16
2.3	(a) Total junction resistance $R_j$ , boundary resistance $R_B$ , and CNT interfacial region resistances $R_{\text{CNT,IR}}$ as functions of CNT pillar length $PL$ . The details of how $R_j$ is decomposed into $R_B$ and $R_{\text{CNT,IR}}$ will be given in Section III.B.(b) The dependence of junction thermal resistance on minimum inter-pillar distance and reservoir distance. . . . .	18
2.4	A typical temperature profile from CNT pillar to graphene sheet across the van der Waals junction. The interfacial regions almost disappear, and the junction resistance is dominated by the boundary resistance. . . . .	20
2.5	(a) Temperature profile of short CNT pillar structures. Note the absence of a linear part in the CNT pillar's temperature profile. (b) Temperature profile of extremely short CNT pillar. . . . .	23
2.6	(a) Local density of states of a short CNT pillar over CNT center region, CNT interfacial region, and graphene interfacial region. (b) Local density of states of an extremely short CNT pillar over CNT and CNT interfacial region, and graphene interfacial region. (CNT center region and CNT interfacial region have merged into CNT and CNT interfacial region because of the extremely short pillar.) (c) LDOS overlap factor for different $PL$ . . . . .	25
2.7	Comparison of system thermal conductivity predicted from our network model and from direct MD simulations in Ref.13. The black and red curves represent predictions of two <i>MIPD</i> cases for different $PL$ without CNT resistances, the pink and blue curves represent those with CNT resistances, while the three symbols represent direct MD simulation results. $PL_m$ - $MIPD_n$ indicates that $PL$ equals $m$ Angstrom, and $MIPD$ equals $n$ Angstrom. . . . .	28
3.1	Orthogonal front view (a) and perspective view (b) of the detailed structure of a single CNT-graphene junction in pillared graphene. Red atoms form a heptagon. . . . .	32
3.2	Interface structure of single-vacancy defect (a), Stone-Wales defect (b), unzipped (6,6) CNT (c), and the left side view, front view, right side view of 30-degree turning CNT (d) and 90-degree turning CNT (e). . . . .	35
3.3	The temperature profile of 90-degree turning CNT in NEMD simulation. . . . .	36

Figure	Page
3.4 (a) The thermal boundary resistance (TBR) results and the corresponding deviation percentage from the average at a Stone-Wales defect in (6,6) CNT with different initial velocities from NEMD simulations (the left axis is the scale of thermal boundary resistance, the right axis is the scale of deviation percentage). The red dashed-line is the average thermal boundary resistance of the six trials. (b) The thermal boundary resistance results at a Stone-Wales defect in (6,6) CNT with different domain sizes in NEMD simulations. $L$ is the length of CNT along the heat transfer direction between reservoirs. . . . .	40
3.5 (a) Two single-vacancy defects in series, (b) four single-vacancy defects in parallel, (c) two Stone-Wales defects in series, (d) three Stone-Wales defects in parallel. Pink atoms are directly affected by defects. . . . .	41
3.6 The CNT-nanocone-graphene structures with different carbon nanocone apex angles. . . . .	44
4.1 (a) Schematic of the pillared graphene structure used in this work. Top view (b) and front view (c) of the detailed junction structure. (d) Detailed junction structure with perspective, where the heptagon defects are highlighted with red. . . . .	48
4.2 Typical wave packet propagation process for an incident LA mode from CNT. Atom velocity (the left axis is the scale of atom velocity in CNT, the right axis is the scale of atom velocity in graphene) plot before the wave packet reaches the interface (a), when the wave packet just reaches the interface (b), after transmission (c). (d) In-plane displacements (amplified by 600 times) of graphenen atoms. (e) Out-of-plane displacements (amplified by 600 times) of graphene atoms. . . . .	50
4.3 The wave packet in $k$ -space. . . . .	53
4.4 The phonon dispersion relation of CNT and graphene. . . . .	53
4.5 The out-of-plane velocity of atoms in graphene sheet during the incident LA mode wave packet transmission process. The phonon frequency is about $355 \text{ cm}^{-1}$ . . . . .	54
4.6 All the directions included for the averaging calculation of overall transmission coefficient. . . . .	55

Figure	Page
4.7 An incident CNT LA wave packet (a) and its transmitted graphene LA and ZA wave packets (b) in $k$ -space, and the corresponding identified modes on CNT LA branch (c) and graphene LA and ZA branches (d), respectively. An incident CNT TA wave packet (e) and its transmitted graphene LA, TA, and ZA wave packets (f) in $k$ -space, and the corresponding identified modes on CNT TA branch (g) and graphene LA, TA, and ZA branches (h), respectively. . . . .	57
4.8 Transmission coefficients of incident LA (a), TA (b), TW (c), and RB polarization (d). . . . .	59
5.1 (a) The general structure of thermal transport considered in Landauer approach. (b) The CNT-graphene structure with a dimensionally mismatched 1D-2D interface. . . . .	68
5.2 The transmission coefficients as a function of phonon frequency of different branches from CNT to graphene from acoustic and diffuse mismatch models. The AMM transmission curves of acoustic branches have been highlighted. The green curve is the DMM transmission coefficient. . . . .	76
5.3 The directional thermal conductance contribution from NEGF at Si/heavy-Si interface. . . . .	79
5.4 (a) The temperature profile from NEMD compared to $T_\lambda$ from Landauer approach at Si/heavy-Si interface. $\lambda$ is the phonon mode. The emitted temperatures $T_{e,1}$ and $T_{e,2}$ are carefully selected to make equivalent equilibrium temperatures $T_1$ and $T_2$ match the temperature jump at the interface from NEMD simulations. (b) The schematic of emitted temperature $T_e$ and modal equivalent equilibrium temperature $T_\lambda$ . (c) The details of temperatures near the interface at Si/heavy-Si interface. . . . .	80
5.5 The intrinsic thermal boundary conductance $G_{iLD}$ , dressed thermal boundary conductance $G_{dLD}$ , and conventional thermal boundary conductance $G_{cLD}$ from Landauer approach with Bose-Einstein distribution, and NEMD thermal boundary conductance $G_{NEMD}$ from nonequilibrium molecular dynamics at Si/heavy-Si interface. . . . .	81
5.6 The intrinsic thermal boundary conductance $G_{iLD}$ , dressed thermal boundary conductance $G_{dLD}$ , and conventional thermal boundary conductance $G_{cLD}$ from Landauer approach with classical Boltzmann distribution, and NEMD thermal boundary conductance $G_{NEMD}$ from nonequilibrium molecular dynamics at Si/heavy-Si interface. . . . .	84

Figure	Page
5.7 (a) Modal conductance and (b) spectral conductance accumulation of intrinsic TBC $G_{iLD}$ , dressed TBC $G_{dLD}$ , and conventional TBC $G_{cLD}$ from Landauer approach with Bose-Einstein distribution at Si/heavy-Si interface with $M_2/M_1 = 0.6$ . . . . .	87
5.8 The conductance ratio $r_G$ plot with different mass ratio and phonon group velocity ratio of material 1 and 2. . . . .	89
5.9 The comparison between TBC at ZnO/GaN interface from experiments and Landauer formula. . . . .	91

## ABSTRACT

Shi, Jingjing Ph.D., Purdue University, December 2018. Atomistic Simulations of Thermal Transport across Interfaces. Major Professors: Xiulin Ruan and Timothy S. Fisher, School of Mechanical Engineering.

The rapid advance in modern electronics and photonics is pushing device design to the micro- and nano-scale, and the resulting high power density imposes immense challenges to thermal management. Promising materials like carbon nanotubes (CNTs) and graphene offer high thermal conductivity in the axial (or in-plane) directions, but their thermal transport in the radial (or cross-plane) directions are poor, limiting their applications. Hierarchical structures like pillared graphene, which is composed of many CNT-graphene junctions, have been proposed. However, thermal interfacial resistance is a critical issue for thermal management of these systems. In this work, we have systematically explored thermal transport across interfaces, particularly in pillared graphene and silicon/heavy-silicon.

First, by recognizing that thermal resistance of the 3D pillared graphene architecture primarily comes from CNT-graphene junctions, a simple network model of thermal transport in pillared graphene structure is developed. Using non-equilibrium molecular dynamics (NEMD), the resistance across an individual CNT-graphene junction with  $sp^2$  covalent bonds is found to be around  $6 \times 10^{-11}$  m<sup>2</sup>K/W, which is significantly lower than typical values reported for planar interfaces between dissimilar materials. Interestingly, when the CNT pillar length is small, the interfacial resistance of the  $sp^2$  covalent junction is found to decrease as the CNT pillar length decreases, suggesting the presence of coherence effects. The junction resistance  $R_j$  is eventually used in the network model to estimate the effective thermal conductivity, and the results agree well with direct MD simulation data, demonstrating the effectiveness of our model.

Then we identify three different mechanisms which can lead to thermal resistances across the pillared graphene junction: the material mismatch (phonon propagates from CNT to graphene), the non-planar junction (the phonon propagation direction must change), and defects (there are six heptagons at each junction). The NEMD results show that three mechanisms lead to similar resistance at the CNT-graphene junction, each at around  $2.5 \times 10^{-11} \text{ m}^2\text{K/W}$ .

Further, we have predicted the transmission function of individual phonon mode using the wave packet method at CNT-graphene junction. Intriguing phonon polarization conversion behavior is observed for most incident phonon modes. It is found that the polarization conversion dominates the transmission and is more significant at larger phonon wavelength. We attribute such unique phonon polarization conversion behavior to the dimensional mismatch across CNT-graphene interface. It is found that the transmission functions at the junction cannot be predicted by the conventional acoustic mismatch models due to the existence of dimensional mismatch. Further analysis shows that, the dimensionally mismatched interface, on one hand tends to reduce the transmission and conductance due to defects and the change of phonon propagation direction at the interface, while on the other hand tends to enhance the transmission and conductance due to the new phonon transport channel introduced by polarization conversion.

Finally, we address that many recent experiments have shown that the measured thermal boundary conductances (TBCs) significantly exceed those calculated using the Landauer approach. We identify that a key assumption that an interface is a local equilibrium system (different modes of phonons on each side of the interfaces are at the emitted phonon temperature  $T_e$ ), is generally invalid and can contribute to the discrepancy. We show that the measurable temperature for each individual mode is the "modal equivalent equilibrium temperature"  $T_\lambda$  rather than  $T_e$ . Also, due to the vast range of transmission functions, different phonon modes are out of local thermal equilibrium. Hence, the total conductance cannot be simply calculated as a summation of individual modal conductance. We modify the Landauer approach

to include these effects and name it the "Nonequilibrium Landauer approach". Our approach has been used on the carbon nanotube (CNT)/graphene and Si/heavy-Si interfaces which are matched interfaces, and it gives 310% increases in TBC as compared to the conventional Landauer approach at CNT-graphene junction and even higher increase for Si/heavy-Si with small mass ratios. A convenient chart is created to estimate the conductance correction based on our approach, and it yields quite accurate results. Our work indicate that the measured high TBCs in experiments can be due to this nonequilibrium effect rather than the other proposed mechanisms, like inelastic phonon transmission and cross-interface electron-phonon coupling.

The results obtained in this study will provide a deeper understanding of nanoscale thermal transport across interfaces. This research also provides new perspectives of atomic- and nano-scale engineering of materials and structures to enhance performance of thermal management.

## 1. INTRODUCTION

### 1.1 Motivation

Over the past few decades, the size of electronic devices has decreased to nanoscale dimensions as shown in Fig. 1.1, and thermal management of these devices has become a significant issue to ensure high performance and reliability [1–5]. Dielectric materials and semiconductors with high thermal conductivity [6–13], like diamond, boron nitride, gallium arsenide, are extremely needed to effectively dissipate thermal energy. Among those materials, carbon nanotubes (CNTs) [14–16] and graphene [17–20] are promising high thermal conductivity materials as shown in fig. 1.2, and at the same time they offer high electron mobility and low mass density. However, both of them suffer from anisotropy in thermal transport, i.e. the thermal conductivity of CNT axial direction and graphene in-plane directions is two order higher than in other directions. Hence, the idea of constructing three-dimensional interconnected structures, with CNT, graphene or both as building blocks, such as pillared graphene [21], carbon nanotubes with intramolecular junctions [22], and CNT networks [23], has been proposed. These structures offer potential utility in thermal management of electronic devices. However, because of the combination of materials, thermal interfacial resistance at the CNT-graphene, CNT-CNT junctions is a critical issue for thermal management of these systems. Thermal resistances from interfaces were previously reported to be comparable to or dominant over those of the materials. For example, the thermal boundary resistance (TBR) at the CNT-graphene junction is comparable to the resistance of a 200 nm long pure CNT [24, 25]. Hence, understanding thermal interfacial transport and designing interfaces with high thermal conductance are urgent problems to study. Other than interfaces in carbon-based materials, interfaces are also very important in widely used advanced technological devices with semi-

conductor heterostructures, like quantum cascade lasers [26–28], transistors [29–31], thermoelectric devices [32–35], and light emitting diodes [36–38].

The importance of interfaces in heat dissipation is related to the phonon transport. There is an interruption on the regular crystalline lattice at the interface, and as a result, phonon propagation will be affected. Since not all phonons can transmit through the interface, there will be thermal resistance from reflection. The existence of the interface thermal resistance makes the thermal management in devices even harder as the sizes of devices become smaller and smaller from time to time. Because of the significance of interfaces in energy transportation, people have studied the thermal properties at interfaces based on theories, simulations, and experiments. However, the thermal transport at interfaces is not fully understood.

As mentioned above, in order to dissipate heat three dimensionally (3D) in devices and systems, those low dimensional, high thermal conductivity materials, like CNT, graphene, boron nitride, molybdenum disulfide, black phosphorous, need to be interconnected. With the application of these low dimensional materials, dimensionally mismatched non-planar interfaces, such as 1D-2D [21, 23, 24, 39, 40], 1D-3D [41–45], and 2D-3D [16, 46, 47] interfaces, are emerging. As a result, more interfaces and junctions with dimensional mismatch will appear from now on. It will be more and more important to understand and control heat transfer at interfaces and junctions as shown in Fig. 1.3. The thermal transport through interfaces and junctions with dimensional mismatch is not only critical in applications, but also introduces new energy transfer mechanisms and physics as well. , but existing theories may not describe their thermal interfacial transport correctly due to new physics introduced by the dimensional mismatch. Even for the planar interfaces, though have been extensively studied, existing theories such as Landauer approach with the acoustic mismatch model (AMM) or diffuse mismatch model (DMM) [48] cannot accurately predict the resistances at interfaces, while computational methods like nonequilibrium molecular dynamics (NEMD) and atomistic Green’s function (AGF) are very time-consuming. For the dimensionally mismatched non-planar interfaces, attempt

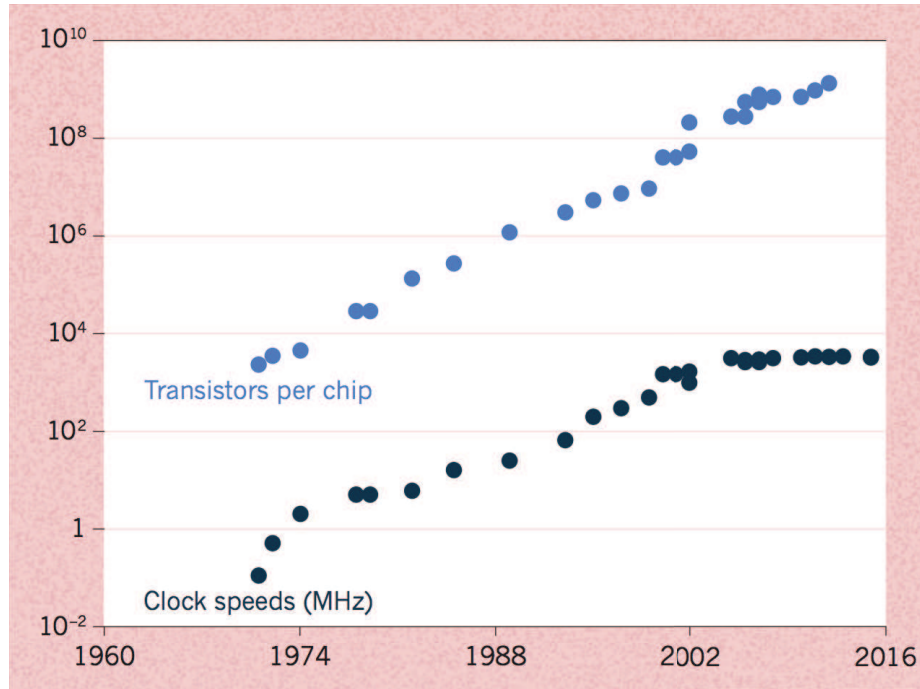


Figure 1.1. For the past five decades, the number of transistors per microprocessor chip a rough measure of processing power has doubled about every two years, in step with Moores law. [5]

of modified acoustic mismatch model has been made at 1D-3D interface [45], but has not been compared with simulation or experimental results. For the planar interfaces, many recent experiments have shown that the measured TBCs significantly exceed those calculated using the Landauer approach, or even exceed the "radiation limit" which is believed to be the upper bound of TBC. Two mechanisms have been proposed to explain the discrepancy, including inelastic phonon transmission and cross-interface electron-phonon coupling, but no consensus has been reached due to the lack of reliable methods to quantify these mechanisms To address these limitations, our current work will consider CNT-graphene junction (as shown in Fig. 1.4) as an example of dimensionally mismatched non-planar interfaces and Si/heavy-Si interface as an example of planar interfaces. In this study, we will use CNT-graphene and Si/heavy-Si as the representative interfaces to systematically explore the thermal transport across interfaces.

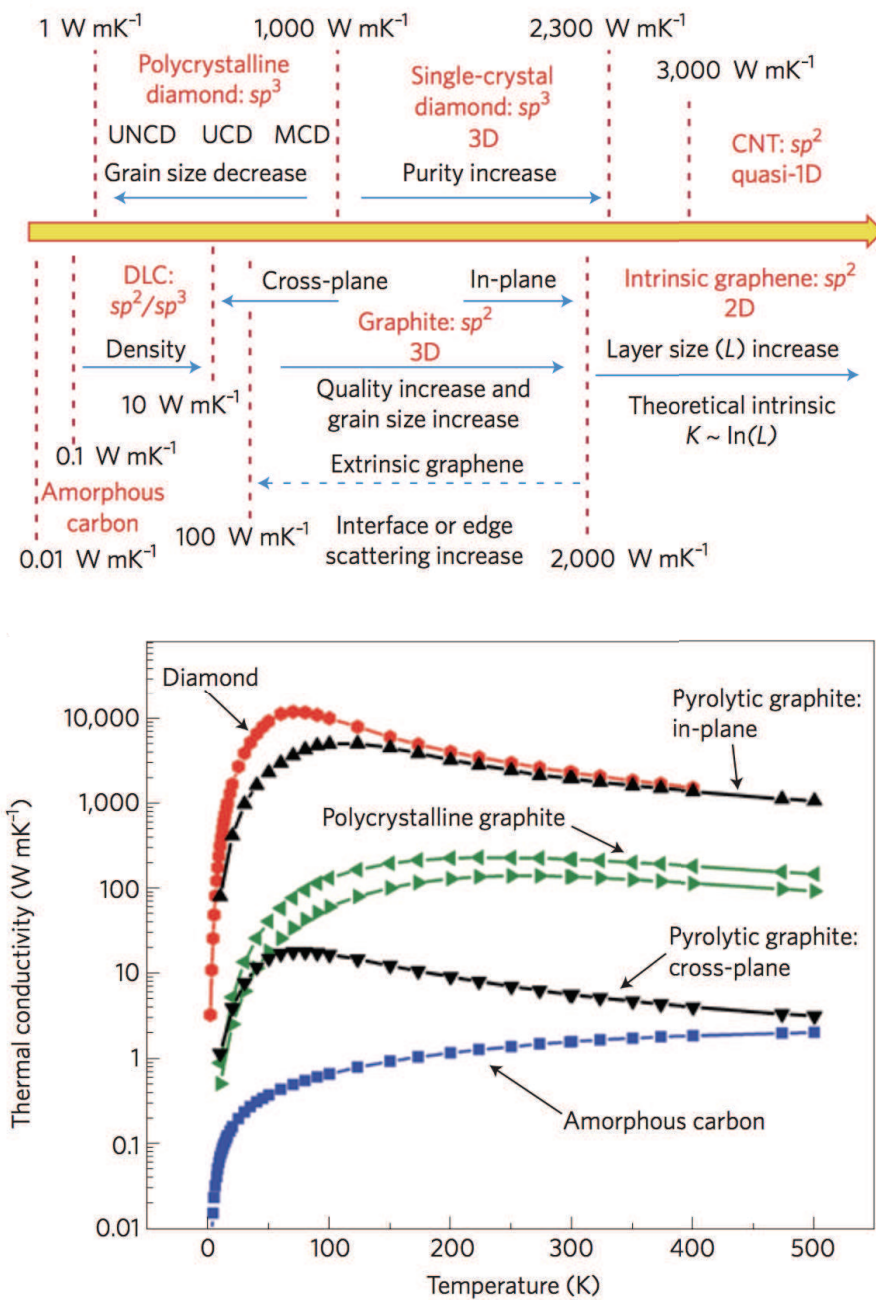


Figure 1.2. Thermal properties of carbon allotropes and their derivatives. [13] Top: Diagram based on average values reported in literature. The axis is not to scale. Bottom: Thermal conductivity of bulk carbon allotropes as a function of  $T$ .

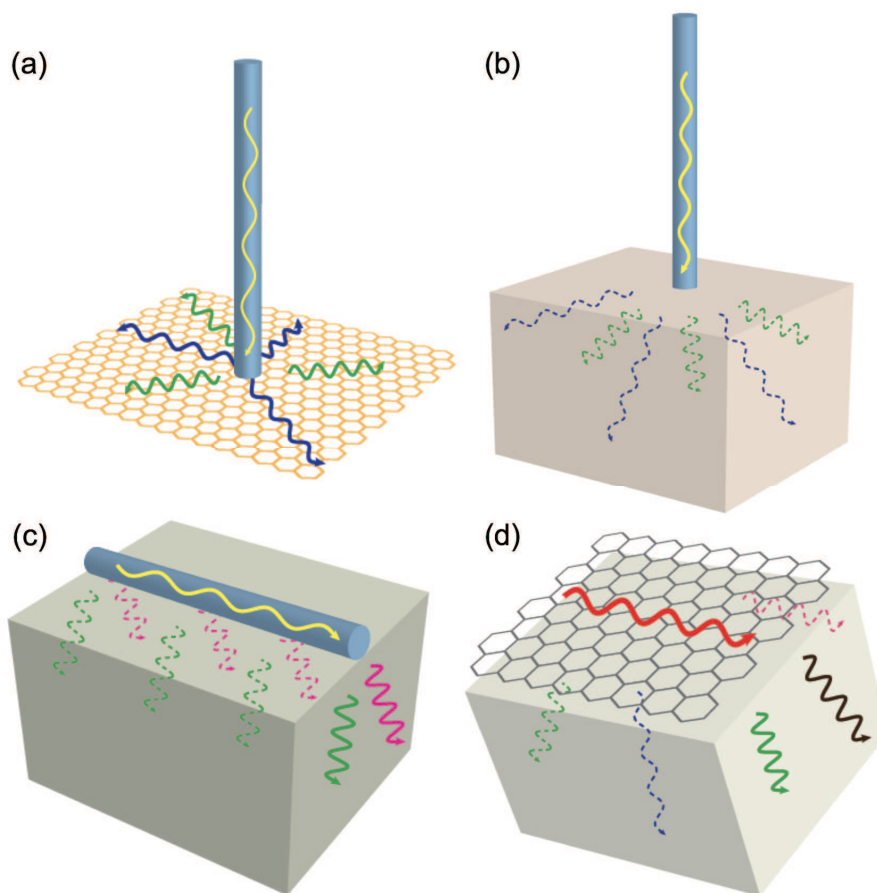


Figure 1.3. (a) phonons transport between 1D material and 2D material; (b) phonons transport between 1D material and 3D material (1D material is perpendicular to 3D material); (c) phonons transport between 1D material and 3D material (1D material is parallel to 3D material); (d) phonons transport between 2D material and 3D material.

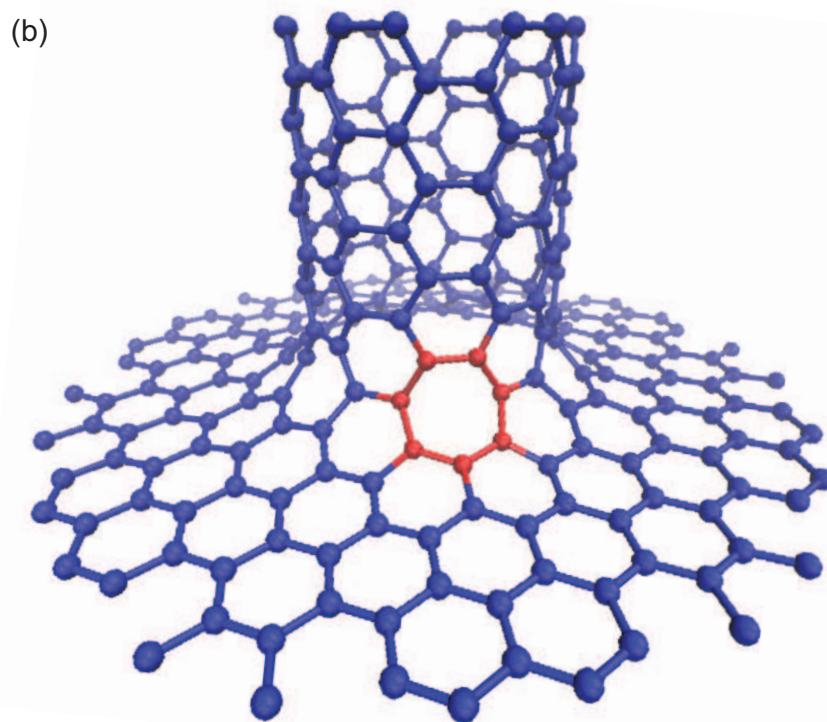
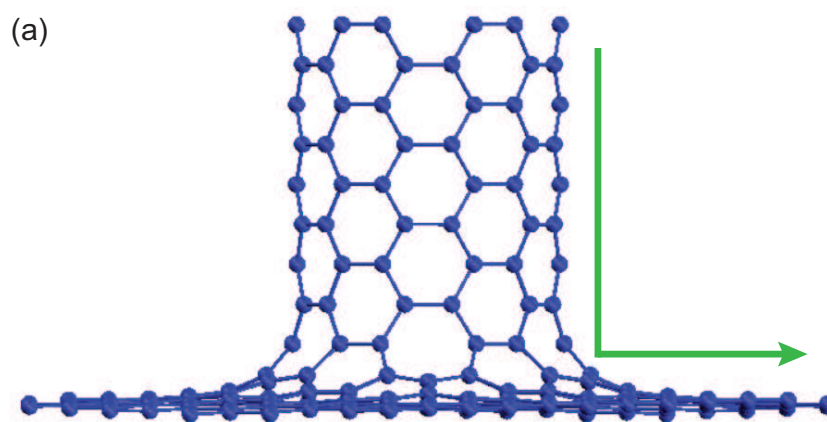


Figure 1.4. The pillared graphene network structure with  $sp^2$  covalent bonds at junctions.

## 1.2 Thermal Transport in CNT-graphene Networks

As mentioned in the last section, the thermal conductivities of both carbon nanotubes and graphene are very high. The measured thermal conductivity of suspended single layer graphene at room temperature can be about 1500 to 3000 W/mK, and the measured thermal conductivity of the single layer graphene on substrates is about 600 W/mK. The measured thermal conductivity of suspended CNT at room temperature can be about 3000 to 3500 W/mK [49, 50]. The extremely high thermal conductivity of CNT and graphene (Fig. 1.2) is the result of strong C-C  $sp^2$  covalent bonds and the low-dimension structure. However, as mentioned above, both of them suffer from anisotropy in thermal transport. The thermal conductivity of graphene stacks or graphite in the cross-plane direction is two or more orders of magnitude lower than that of the in-plane direction [51]. CNT bundles also show similar behavior in the radial direction [52]. Hence, the idea of constructing three-dimensional interconnected structures, with CNT, graphene or both as building blocks has been proposed to enhance the heat dissipation in all three directions.

The thermal transport through pillared graphene with  $sp^2$  covalent bonds at junctions, as shown in Fig. 1.4, has been modeled recently by Varshney et al. [53] using non-equilibrium molecular dynamics (NEMD) method. They calculated the thermal conductivity of both in-plane and cross-plane directions to fall in the range of about 1 to 20 W/(mK). Their results suggest that the hierarchical structures can help to reduce thermal anisotropy. Lee et al. used a wave packet method to explore phonon energy transmission at the CNT-graphene junction [39]. Park and Prakash presented reverse NEMD (RNEMD) simulations of thermal transport in two pillared graphene architectures with different symmetries [54]. These MD simulations were done on the entire 3D network, and can only give the thermal conductivity of one particular architecture at a time. On the other hand, the thermal transport across an individual junction, which should be important, is still not well understood.

## 1.3 Methodology

### 1.3.1 Classical Molecular Dynamics

Classical MD simulations model the movements of atoms based on the Newton's second law of motion and interatomic potentials. In this way, phonon transport can be simply modeled and nanoscale detailed structure like defects can be simply captured by modifying atom type and position. As a result, the atomic level phenomena can be simulated directly. Due to the rising interest in thermal management issues in nano-scale devices, MD simulations attract a lot of attentions because of its capability to study thermal transport in solids. On the other hand, molecular dynamics method also shows some limitations. The accuracy of MD is limited by the quality of empirical interatomic potentials, and the development of potentials is time-consuming and the quality might not be good. What's more, MD is a classical method, which means quantum effects are not considered. Without quantum effects, the results from MD calculation can have inaccurate especially at very low temperature or when the simulation structure size is very small.

Several MD methods have been used for the modeling of thermal transport, like nonequilibrium molecular dynamics (NEMD) [55], reverse NEMD (RNEMD) [56], equilibrium MD (EMD) [55], and wave-packet method [57–59]. NEMD and RNEMD methods [55, 56] are commonly used methods to calculate the thermal conductivity of materials or thermal boundary resistance at the interface. In NEMD simulation, the heat flux is fixed, and the resulting temperature profile can be used to calculate thermal conductivity and thermal resistance at the interface. In RNEMD simulation, the temperatures of the heat source and the heat sink are fixed, like NEMD, using the calculated heat flux and temperature profile, the thermal properties can be obtained. Based on the Fourier's law, the thermal conductivity  $k$  is given by

$$k = -\frac{q}{A\nabla T}, \quad (1.1)$$

and the interface thermal resistance  $R$  is given by

$$R = \frac{A\Delta T}{q}. \quad (1.2)$$

Here  $q$  is the heat flow rate,  $A$  is the cross-sectional area,  $\nabla T$  is the temperature gradient, and  $\Delta T$  is the temperature jump at the interface.

The molecular dynamics phonon wave packet method is an accurate spectral phonon transmission simulation method. Typically classical MD is limited by its classical nature which cannot reproduce the correct Bose-Einstein distribution of different phonon modes, however in the wavepacket method, since only a single mode wave packet is launched in each simulation, such drawback is irrelevant. To create a wave packet for a specific phonon mode, the initial displacement from equilibrium and velocity of the  $i$ th base atom in the  $n$ th unit cell along the  $\alpha$  direction are [39],

$$u_{ni\alpha}^\gamma = \frac{A}{\sqrt{M}} \sum_q \exp \left[ -\frac{(q - q_0)^2}{2\sigma^2} \right] \varepsilon_{i\alpha}^\gamma(q) \exp [iq(z_n - z_0)], \quad (1.3)$$

$$v_{ni\alpha}^\gamma = \frac{A}{\sqrt{M}} \sum_q -i2\pi v^\gamma(q) \exp \left[ -\frac{(q - q_0)^2}{2\sigma^2} \right] \varepsilon_{i\alpha}^\gamma(q) \exp [iq(z_n - z_0)], \quad (1.4)$$

where  $A$  is the amplitude of the wave packet,  $M$  is the carbon atom mass,  $q_0$  is the wavenumber of the packet,  $z_0$  and  $z_n$  are the positions of the packet center and the  $n$ th unit cell in the CNT along the propagation path  $\hat{s}$ , and  $\varepsilon$  is the eigenvector of the phonon with wavenumber  $q$  and polarization  $\gamma$ . Using the wave packet method, mode-resolved phonon transmission coefficients  $\Gamma$  across an interface can be calculated as transmitted energy over the total incident energy.

### 1.3.2 Landauer Approach

Landauer formula is based on the particle description of energy or electricity carriers. For the thermal transport problems, phonons and electrons are usually

considered as energy carriers. In our carbon-based systems, thermal transport by electrons can be neglected. Hence, the heat flow rate from Landauer formula is usually in the form below [60],

$$q = \frac{1}{2\pi} \int_0^{+\infty} M(\omega)\tau(\omega)\hbar\omega[f(T_1) - f(T_2)]d\omega, \quad (1.5)$$

where  $M(\omega)$  is the number of modes at a given frequency  $\omega$ ,  $\tau(\omega)$  is the transmission coefficient at the interface from one material to the other. The number of modes can be obtained through lattice dynamics calculation, which is an approach to compute the normal modes in a harmonic crystal lattice at zero Kelvin. However, this form is for the calculation of a device between the same material. In our system, since the interface is between two different materials with dimensional mismatch, the number of modes of CNT and graphene are different. Hence, the form of Landauer formula below should be used for our system,

$$q = \frac{1}{2\pi} \int_0^{+\infty} \hbar\omega[M_1(\omega)\tau_{1\rightarrow 2}(\omega)f(T_1) - M_2(\omega)\tau_{2\rightarrow 1}(\omega)f(T_2)]d\omega. \quad (1.6)$$

As the heat flow rate can be calculated, the thermal boundary conductance (TBC) can be calculated like what we did in NEMD calculation,

$$G = \frac{q}{A\Delta T}. \quad (1.7)$$

However, experimental and molecular dynamics simulation results [61–63] often exceed the TBC predicted from the Landauer formula. Two possible mechanisms have been proposed, including inelastic scattering at the interface [64, 65] and cross-interface electron-phonon coupling [66–70]. However, before involving these mechanisms, Landauer formula is based on an important assumption that an interface is a local thermal equilibrium system, where the measurable temperatures of all phonon modes are the emitted phonon temperature  $T_e$ . Such an assumption may be reasonable for electron and photon interfacial transport, for which the Landauer approach was originally developed, since the temperature reservoirs can be held right adjacent to the interface or surface. However, it is questionable for phonons, since in standard

measurements of interfacial thermal conductance such as the two-bar method [71], the reservoirs are placed far away from the interface, so as in molecular dynamics simulations of interfacial thermal transport [55]. Hence the nonequilibrium effect needs to be incorporated in the Landauer approach to give more accurate predictions.

## 1.4 Objective and Organization

The major objective of this research is to understand the thermal transport across interfaces. The results can be used to guide the design of solid-state devices to enhance their heat dissipation. This dissertation is organized as follows.

In Chapter 2, by recognizing that thermal resistance of the 3D pillared graphene architecture primarily comes from CNT-graphene junctions, a simple network model of thermal transport in pillared graphene structure is developed. Using non-equilibrium molecular dynamics, the resistance across an individual CNT-graphene junction with  $sp^2$  covalent bonds and across a van der Waals junction is calculated. Interestingly, the interfacial resistance of the  $sp^2$  covalent junction is found to be related to the CNT pillar length, suggesting the presence of coherence effects. The junction resistance  $R_j$  is eventually used in the network model to estimate the effective thermal conductivity, and the results are compared with direct MD simulation data.

In Chapter 3, we study three different mechanisms which can lead to thermal resistances across the pillared graphene junction: the material mismatch (phonon propagates from CNT to graphene), the non-planar junction (the phonon propagation direction must change), and defects (there are six heptagons at each junction). The contributions of different mechanisms to the total junction thermal resistances are not clear from the previous NEMD simulation, which can only give an overall resistance. To understand the effects on the resistance of different mechanisms, we have decomposed the junction thermal resistance of pillared-graphene junction to different mechanisms and calculated the thermal resistance caused by each mechanism. We performed NEMD simulations to compare five types of different junctions corre-

sponding for different mechanisms: unzipped CNT to isolate the effects of materials mismatch; CNT with single vacancy and Stone-Wales defects to isolate the effects of defects; vertical CNT-CNT junction, and 30 degree CNT-CNT junction to capture the effects of non-planar junction and other mechanisms. The relations between thermal boundary resistance and both defect number and turning angle at the interface are also studied.

In Chapter 4, we have predicted the transmission function across pillared graphene interface (between 1D CNT and 2D graphene) of individual phonon mode using the wave packet method. Some surprising phenomena are found and attributed to the dimensional mismatch across the unique CNT-graphene interface. The polarization conversion behavior at the dimensionally mismatched interface adds an additional channel to dissipate heat.

In Chapter 5, we first apply the conventional Landauer approach to the CNT-graphene interface which is a matched interface. A comparison to the results from nonequilibrium molecular dynamics (NEMD) method shows that the conventional Landauer formula underestimates the TBC. To verify our observation, a Si/heavy-Si system is studied with both Landauer formula and NEMD method, and it is found that with increased similarity between the two materials, the under-estimation from the conventional Landauer approach increases. The underestimation is identified to come from the assumption that all phonon modes are at the emitted temperatures  $T_e$ . To modify the Landauer approach, we use the modal equivalent equilibrium temperature to calculate the modal conductance and show the local thermal nonequilibrium; we then define the overall equivalent lattice temperature to calculate the total thermal conductance. Our "nonequilibrium Landauer approach" is applied for the Si/heavy-Si interface, CNT-graphene junction, and ZnO/GaN interface, and the results agree much better with the NEMD method and experimental results [63]. A chart is also created to quickly estimate the correction of the interfacial conductance as a function of the mass ratio, and it will help determine whether our approach is needed for a given interface.

## 2. THERMAL TRANSPORT ACROSS CNT-GRAPHENE COVALENT AND VAN DER WAALS JUNCTIONS

### 2.1 Introduction

Over the past few decades, the size of electronic devices has decreased to nanoscale dimensions, and thermal management of these devices has become a significant issue to ensure high performance and reliability. Materials with high thermal conductivity are needed to effectively dissipate thermal energy. Carbon nanotubes (CNTs) [14–16] and graphene [17–20] are promising high thermal conductivity materials, and at the same time they offer low mass density. However, both suffer from anisotropy in thermal transport. The thermal conductivity of graphene stacks or graphite in the cross-plane direction is two or more orders of magnitude lower than that of the in-plane direction. [51] CNT bundles also show similar behavior in the radial direction. [52] Hence, the idea of constructing three-dimensional interconnected structures, with CNT, graphene or both as building blocks, such as pillared graphene [21], carbon nanotubes with intramolecular junctions [22], and CNT networks [23], has been proposed. These structures offer potential utility in thermal management of electronic devices.

The thermal transport through pillared graphene with  $sp^2$  covalent bonds at junctions, as shown in Fig. 2.1(a), has been modeled recently by Varshney et al. [53] using non-equilibrium molecular dynamics (NEMD). They calculated the thermal conductivity of both in-plane and cross-plane directions to fall in the range of about 1 to 20 W/(mK). Their results suggest that the hierarchical structures can help to reduce thermal anisotropy. Lee et al. used a wave packet method to explore phonon energy transmission at the CNT-graphene junction. [39] Park and Prakash presented reverse NEMD (RNEMD) simulations of thermal transport in two pillared graphene architec-

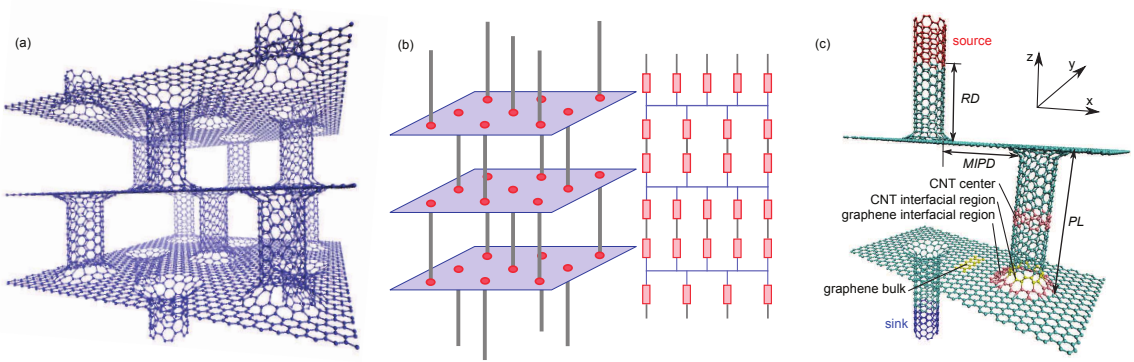


Figure 2.1. (a) The pillared graphene structure with  $sp^2$  covalent bonds at junctions. (b) Schematic of the network model. Intrinsic thermal resistances of CNTs and graphene are neglected; then the system can be simplified as junction resistances in parallel and series networks. (c) The small pillared graphene cell of the simulation domain. Periodic boundary conditions are applied in  $x$  and  $y$  directions, while fixed boundary conditions are applied in the  $z$  direction. The three important geometric parameters are pillar length ( $PL$ ), minimum inter-pillar distance ( $MIPD$ ) and the distance from the junction to the thermal reservoir (or reservoir distance,  $RD$ ). Four important regions are the CNT center region, CNT interfacial region, graphene interfacial region, and graphene bulk. These regions are defined because they have different LDOS, and the details are given in sections III.B and III.C.

tures with different symmetries. [54] These MD simulations were done on the entire 3D network, and can only give the thermal conductivity of one particular architecture at a time. On the other hand, the thermal transport across an individual junction is not well understood.

We assume that the thermal resistance of the complex 3D architecture is dominated by the CNT-graphene junction resistance, while the resistances of the graphene sheets and CNT pillars are relatively small in comparison. Therefore, a simple thermal network model is proposed, shown in Fig. 2.1(b) as an effective and efficient thermal transport design tool for such pillared graphene networks. NEMD simulation is first used to predict the thermal resistance across an individual CNT-graphene junction

with respect to different structural parameters. Trends between junction resistance  $R_j$  and geometric parameters are found, and are then explained using the local density of states (LDOS) concepts. Finally the junction resistance  $R_j$  is used in the network model to predict the thermal conductivity of the 3D pillared graphene structure, and the results are compared to direct MD simulations. The thermal conductivity of a network model including CNT resistance is also calculated as a comparison.

## 2.2 MD SIMULATION METHOD

In previous predictions of thermal transport in a pillared graphene structure [53, 54], the thermal conductivity in the cross-plane direction was found to depend strongly on the CNT-graphene junction, whereas the in-plane conductivity was less sensitive. Hence, in this work, we focus on the cross-plane thermal properties. Because of the high thermal conductivity of both CNTs and graphene, the assumption that the thermal resistance in the cross-plane direction mainly comes from junction resistance is made. Therefore, a network model is constructed, as shown in Fig. 2.1(b), composed of junction resistances in parallel and series. Once the junction resistance is calculated, the thermal network can be used to easily find the total resistance of the structure, from which the thermal conductivity can be derived. This approach can save significant computation time and can give insights to thermal transport in such complex structures.

In order to obtain the junction thermal resistance, the NEMD [55] is performed on just a small cell of the pillared graphene structure. The small cell is composed of three (6,6) CNT pillars and two graphene sheets, as shown schematically in Fig. 2.1(c). The CNT is oriented in the  $z$  direction, while the graphene sheets are in the  $x$ - $y$  plane. Three important geometric parameters exist in the simulation domain: the length of CNT pillar between two graphene sheets called pillar length ( $PL$ ), the minimum graphene length between two CNT pillars called minimum inter-pillar distance ( $MIPD$ ) [53], and the distance from the thermal reservoir to the junction (here

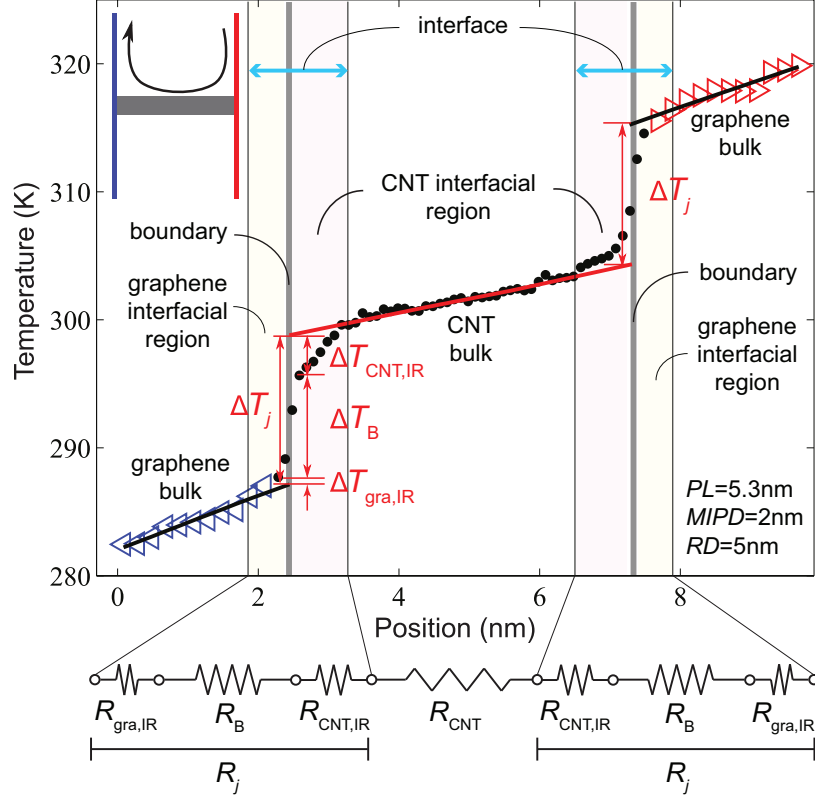


Figure 2.2. A typical temperature profile of two graphene sheets and the CNT pillar in between with  $sp^2$  junctions. The temperature jump at the junction can be decomposed into three components. As a result, the junction resistance  $R_j$  can be decomposed into: boundary resistance  $R_B$ , CNT interfacial region resistance  $R_{CNT,IR}$ , and the graphene interfacial region resistance  $R_{gra,IR}$ . The decomposition details are discussed starting section III.B. Here IR means interfacial regions.

we call it "reservoir distance", or  $RD$ ). Periodic boundary conditions are imposed in the  $x$  and  $y$  directions, and fixed boundary conditions are used for the cross-plane ( $z$ ) direction. Interactions between carbon atoms are described by the AIREBO potential [53, 72, 73], and the potential parameters are from Ref. 17. The same structure but with van der Waals interaction at the junction is also investigated. The Lennard-Jones 12-6 potential with  $\epsilon = 4.7483 \times 10^{-22}$  J and  $\sigma = 0.3407$  nm [74] is used in this case.

In our simulation, the  $PL$  varies from 0.4 to 100 nm, the  $MIPD$  varies from 1 to 5 nm, and the  $RD$  varies from 1 to 100 nm. The thermal reservoirs (heat source and sink regions) have lengths of 5 nm each, as marked in Fig. 2.1(c). At first, an NPT ensemble is run for 2 ns to relax the structure and allow it to reach thermal equilibrium at 300 K. Then it is switched to the NVE ensemble. The simulation time step is 0.4 fs. A heat flux of 1 eV/ps is then added to the source and extracted from the sink for 20 ns. After the system reaches steady state, the temperature of each small cell is obtained by averaging over ten million time steps over the last 4 ns. Such temperature profiles are used to obtain the thermal transport results.

## 2.3 RESULTS AND DISCUSSION

### 2.3.1 Temperature Distribution and Junction Resistance

#### *sp*<sup>2</sup> covalent junctions

Figure 2.2 shows a typical temperature profile of the middle CNT pillar and two graphene sheets with *sp*<sup>2</sup> covalent junctions. The temperature distributions in both CNT and graphene are nearly linear, while at the junction an abrupt temperature jump exists. Hence after linear fitting, the temperature jump  $\Delta T_j$  at the junction can be calculated. The junction thermal resistance  $R_j$  is given by

$$R_j = \frac{A_c \Delta T_j}{q}. \quad (2.1)$$

Here  $q$  is the heat flow rate.  $A_c = 8.57 \times 10^{-19} \text{ m}^2$  is the cross-sectional area of a CNT, approximated as a circular ring of thickness 0.335 nm and of radius (average of inner and outer radius) which equals to the radius of CNT.

The junction resistance  $R_j$  is predicted as a function of  $PL$ , and the results are shown in Figure 2.3(a).  $R_j$  ranges from  $4.1 \times 10^{-11}$  to  $7.2 \times 10^{-11} \text{ m}^2\text{K/W}$ . As a comparison, we also calculate the diffusive limit of  $R_{j,d}$  by using a junction with very long CNT and large graphene, and the value is  $7.5 \times 10^{-11} \text{ m}^2\text{K/W}$ . These values are very low compared to typical thermal boundary resistances across other dissimilar

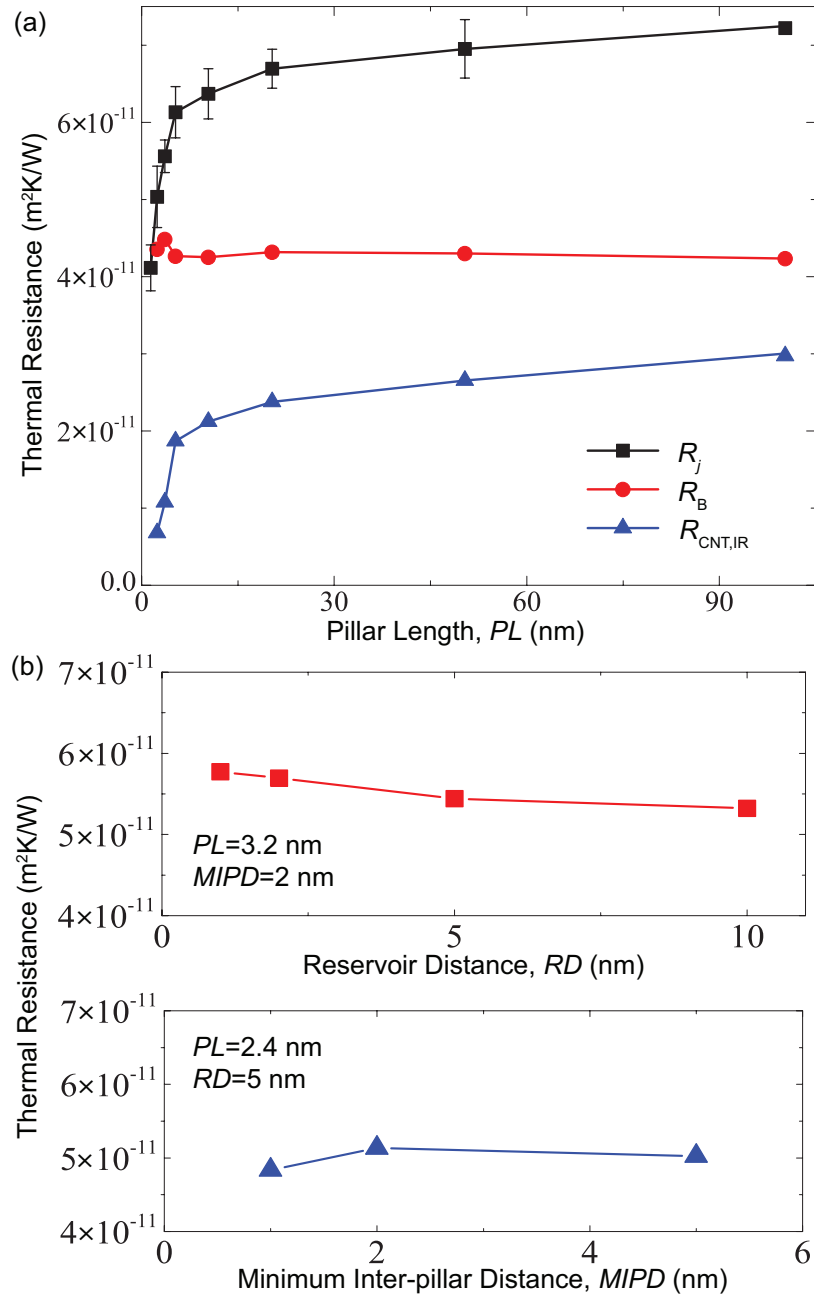


Figure 2.3. (a) Total junction resistance  $R_j$ , boundary resistance  $R_B$ , and CNT interfacial region resistances  $R_{\text{CNT,IR}}$  as functions of CNT pillar length  $PL$ . The details of how  $R_j$  is decomposed into  $R_B$  and  $R_{\text{CNT,IR}}$  will be given in Section III.B.(b) The dependence of junction thermal resistance on minimum inter-pillar distance and reservoir distance.

materials, which are often in the range of  $10^{-10}$  to  $10^{-8}$   $\text{m}^2\text{K}/\text{W}$ . [43, 44, 75, 76] This fact can probably be attributed to no mismatch in atomic mass, and small mismatch in bonding and phonon dispersion across the CNT-graphene junction. Also,  $R_j$  for finite  $PL$  is smaller than the diffusive limit  $R_{j,d}$ , and it decreases as  $PL$  decreases, in contrast to the common case where  $R_j$  is a constant. This behavior indicates that the two junctions are coupled but not independent. Similar coherent behaviors have been observed in superlattices with small periods. [35] It will be discussed in more depth in Section III.B. Using the temperature drop of CNT bulk region in Eq. 2.1, we can calculate the CNT resistance in a similar way. It is typically in the range of  $2.5 \times 10^{-11}$  to  $3.3 \times 10^{-11}$   $\text{m}^2\text{K}/\text{W}$  for  $1.4 < PL < 5.3$  nm, and this weak dependence on  $PL$  is due to the ballistic transport in CNT. Since each CNT is associated with two junctions, the CNT resistance is indeed smaller than the total resistance of two junctions. Therefore, our hypothesis that neglecting the CNT resistance for estimation of the network thermal conductivity is reasonable, noting that the network thermal conductivity will be overestimated a bit by doing so. Nevertheless, we will compare the final results with and without CNT resistance in Section III.D.

Figure 2.3(b) shows the dependence of  $R_j$  on  $MIPD$  and  $RD$ , and the dependencies are very weak, indicating that our calculations are converged on these parameters.

### van der Waals junctions

A typical temperature profile for a van der Waals junction is shown in Fig. 2.4, and the calculated  $R_j$  is  $4.0 \times 10^{-8}$   $\text{m}^2\text{K}/\text{W}$ , which is much higher than that of the covalent junction and is the result of weak bonding. This is consistent with previous experimental observations of bonding effects on thermal interfacial transport. [77] Also, it has little dependence on  $PL$ , indicating the absence of coherence effects. Moreover, this resistance becomes orders of magnitude higher than the CNT bulk

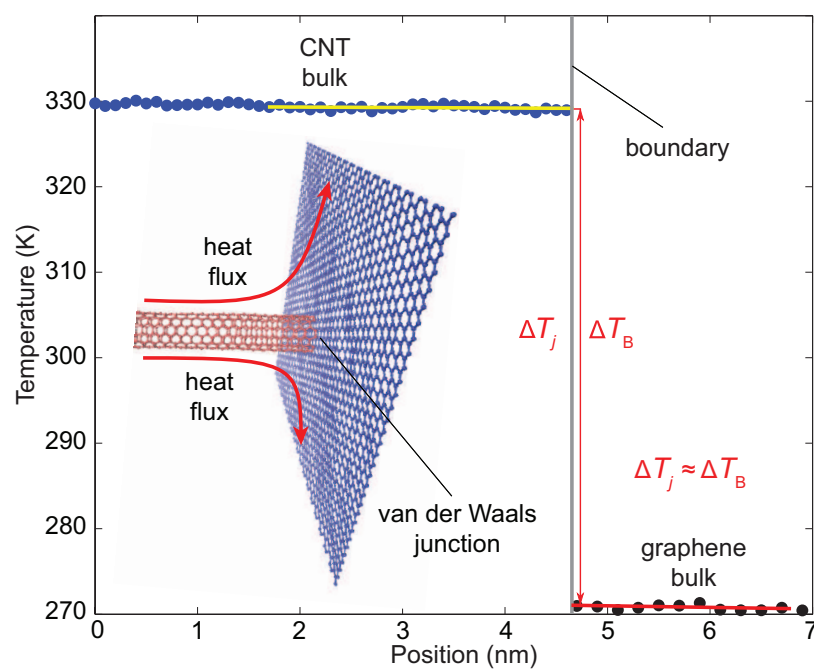


Figure 2.4. A typical temperature profile from CNT pillar to graphene sheet across the van der Waals junction. The interfacial regions almost disappear, and the junction resistance is dominated by the boundary resistance.

resistance, hence in this case neglecting CNT and graphene resistance will not affect the accuracy of our network model.

### 2.3.2 Decomposition of the Junction Resistance

#### *sp*<sup>2</sup> covalent junctions

The dependence of  $R_j$  of *sp*<sup>2</sup> covalent junction on  $PL$  is intriguing. Under the well-known acoustic and diffuse mismatch theories, interfacial thermal resistance can be attributed to the mismatch of phonon impedance or number of modes between the two dissimilar materials constituting the interface. Therefore, the temperature distribution is expected to show linear trends in two materials, with an abrupt jump at the boundary. However, Fig. 2.2 indicates that although the temperature profile in CNT is linear when away from the boundary, it shows a clear nonlinear region near the boundary. In particular, the slope is higher than in the linear region, implying higher local resistance when approaching the boundary. Such nonlinear regions have also been observed for planar interfaces [78], and have been attributed to a distinct interfacial influence. That is, the atoms in such interfacial regions interact with atoms on the other side of the boundary, resulting in deviations in the local density of states (LDOS) relative to the bulk DOS. [61] In Fig. 2.2, the "interface" is defined as the region composed of the CNT interfacial region, the boundary, and the graphene interfacial region.

The effect of the interfacial region on thermal interfacial resistance is two-fold. On one hand, the interfacial region introduces additional resistance inside the region relative to conventional mismatch concepts, and we term this additional resistance as the interfacial region resistance. On the other hand, the existence of interfacial regions will make the mismatch right across the boundary smaller than the conventional mismatch models, hence reducing the boundary resistance. In other words, in the conventional theory the mismatch only exists at the boundary, but now it exists over a transition space that includes the boundary and two interfacial regions.

Hence, as shown in Fig. 2.2,  $\Delta T_j$  can be divided into three parts: (1) the temperature drop between CNT temperature linear fitting and the true CNT temperature at the boundary  $\Delta T_{\text{CNT,IR}}$ ; (2) the temperature drop between the true CNT and graphene temperatures at the boundary  $\Delta T_{\text{B}}$ ; and (3) the temperature drop between graphene temperature and graphene temperature linear fitting at the boundary  $\Delta T_{\text{gra,IR}}$ . Therefore, from the decomposition of  $\Delta T_j$ , the corresponding  $R_j$  can also be divided into three parts as shown in Fig. 2.2: (1) graphene interfacial region resistance  $R_{\text{gra,IR}}$  due to the phonon DOS mismatch between bulk graphene and the graphene interfacial region; (2) the boundary resistance  $R_{\text{B}}$  due to the mismatch between the CNT interfacial region and graphene interfacial region; and (3) the CNT interfacial region resistance  $R_{\text{CNT,IR}}$  due to the mismatch between the CNT bulk and CNT interfacial region. [78] It is obvious that

$$R_j = R_{\text{gra,IR}} + R_{\text{B}} + R_{\text{CNT,IR}}. \quad (2.2)$$

The temperature jump  $\Delta T_{\text{B}}$  due to boundary resistance  $R_{\text{B}}$  is the largest among the three.

When the middle CNT pillar becomes short ( $1 < PL < 3$  nm), the temperature distribution in the CNT does not exhibit a linear portion any more, but only nonlinear profiles, as shown in Fig. 2.5(a). This phenomenon implies that the local phonon DOS never reaches the bulk DOS even at the center of the CNT due to its short length, and hence the two junctions are coupled. When the CNT pillar becomes extremely short ( $PL < 1$  nm), the interfacial regions disappear entirely, and the two junctions are directly coupled as shown in Fig. 2.5(b). The CNT pillar now behaves essentially as one scatterer between the two graphene sheets. Hence, the decomposition of the junction resistance is not shown.

The decomposed boundary and CNT interfacial region resistances for different CNT pillar lengths described above have been calculated, and the results are shown in Fig. 2.3(a). Because the graphene interfacial region resistance is very low and negligible compared to others, it is not plotted in the figure. Importantly, the boundary resistance does not change much for different pillar lengths, which means the

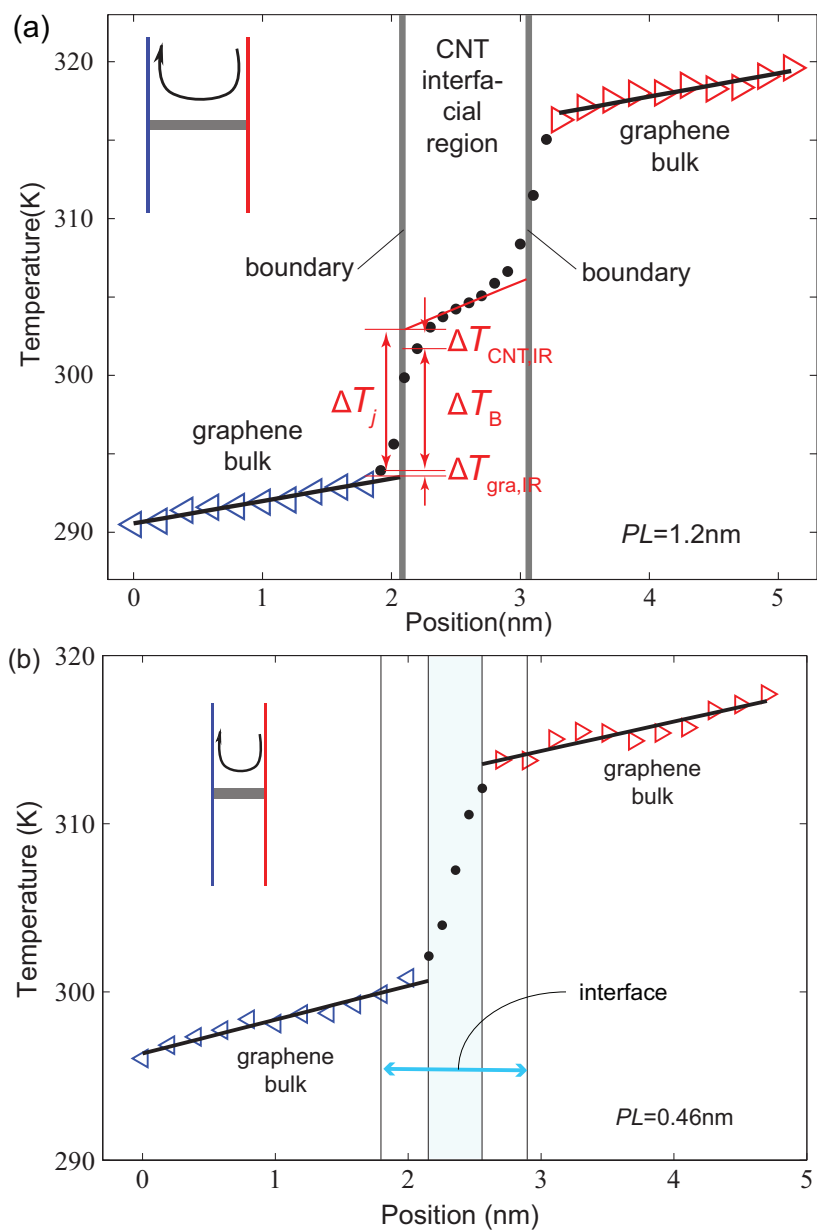


Figure 2.5. (a) Temperature profile of short CNT pillar structures. Note the absence of a linear part in the CNT pillar's temperature profile. (b) Temperature profile of extremely short CNT pillar.

mismatch between the CNT interfacial region and graphene interfacial region is insensitive to  $PL$ . However, the CNT interfacial resistance exhibits a similar trend as the total junction resistance, i.e., decreasing as the pillar length decreases. This implies that changes in the overall junction resistance with respect to  $PL$  are largely dictated by the CNT interfacial region resistance.

### van der Waals junctions

Unlike  $sp^2$  covalent junctions, the temperature profile of the van der Waals junction shows no clear interfacial regions as shown in Fig. 2.4. The temperature jump at the junction nearly equals to the boundary temperature jump. Using the decomposition approach employed for  $sp^2$  covalent junctions, the boundary resistance  $R_B$  is found to dominate the junction resistance  $R_j$ , while the interfacial region resistances are negligible. As mentioned above, the interfacial region by definition possesses a modified DOS. For van der Waals junctions, the atoms near the boundary have very weak interactions with atoms on the other side of the junction, and therefore their local DOS is little modified, in contrast to the  $sp^2$  covalent junction.

### 2.3.3 Phonon Density of States

As mentioned above, the three decomposed resistances correspond to different regions of the structure. Here the local density of states (LDOS) [79] is calculated at different regions of  $sp^2$  covalent junction structure for three different  $PLs$ . The phonon density of states is calculated by taking the Fourier transform of the velocity autocorrelation function (VAC).

$$\text{VAC}(t) = \frac{1}{N} \sum_{i=1}^N \frac{\langle \vec{v}_i(t) \cdot \vec{v}_i(0) \rangle}{\langle \vec{v}_i(0) \cdot \vec{v}_i(0) \rangle}, \quad (2.3)$$

where

$$\langle \vec{v}_i(t) \cdot \vec{v}_i(0) \rangle = \frac{1}{M} \sum_{j=1}^M \vec{v}_i(t_j) \cdot \vec{v}_i(t_j + t), \quad (2.4)$$

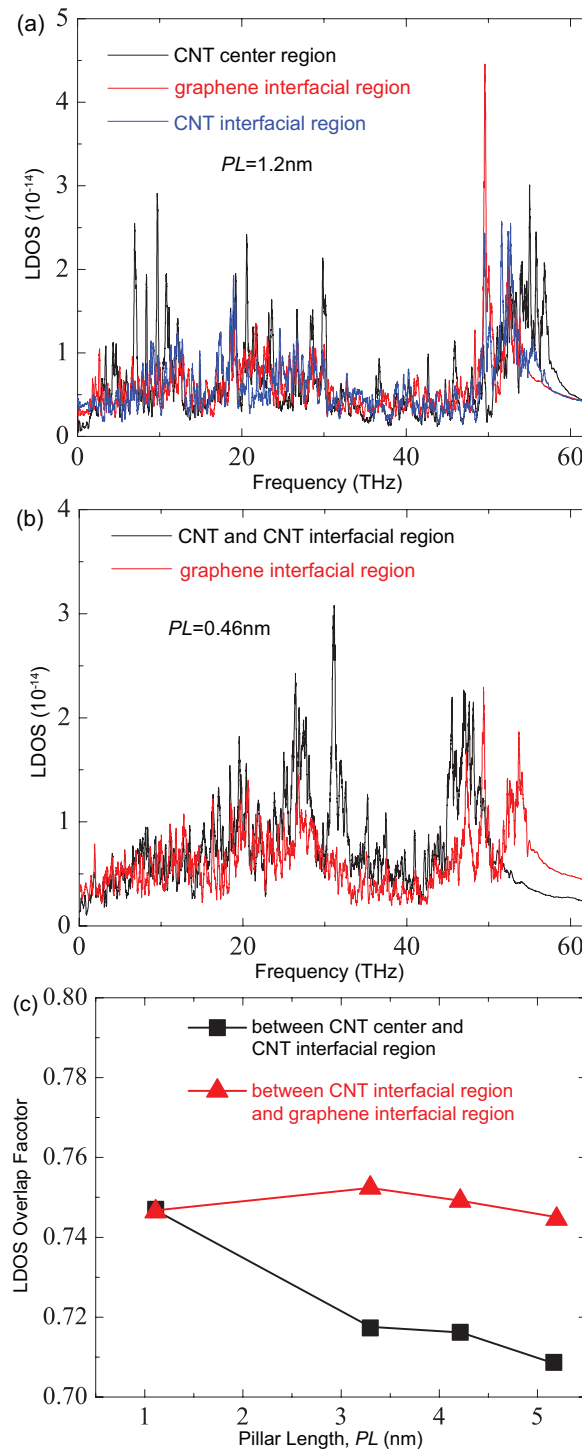


Figure 2.6. (a) Local density of states of a short CNT pillar over CNT center region, CNT interfacial region, and graphene interfacial region. (b) Local density of states of an extremely short CNT pillar over CNT and CNT interfacial region, and graphene interfacial region. (CNT center region and CNT interfacial region have merged into CNT and CNT interfacial region because of the extremely short pillar.) (c) LDOS overlap factor for different  $PL$ .

and  $t$  is the correlation time. The  $i$ -sum is over the number of atoms in the chosen domain, while the  $j$ -sum is over different starting time of the correlation. The Fourier transform of the VAC is

$$f(\omega) \propto \int_{-\infty}^{+\infty} \text{VAC}(t) e^{-i2\pi t\omega} dt, \quad (2.5)$$

and is computed by the MATLAB fast Fourier transform (FFT) function. After the FFT results are normalized, the LDOS of different regions can be assessed.

In our results, it is found that the LDOS of the graphene interfacial region is not sensitive to  $PL$ . Hence, the graphene interfacial region resistance will be little affected by changes in  $PL$ .

Figure 2.6(a) and (b) shows the LDOS of different regions. When the CNT pillar is long, the LDOS of CNT center region is like the LDOS of CNT bulk, and the LDOS of the CNT interfacial region and that of the CNT center region can be distinguished. However, as  $PL$  decreases, the phonon spectrum does not fully reach the bulk spectrum at the center of CNT as shown in Fig. 2.6(a). As a result the mismatch between the CNT interfacial region and the center region is less than the mismatch between CNT interfacial region and CNT bulk, and the mismatch becomes smaller with decreased  $PL$ . When the CNT pillar becomes extremely short, the LDOS of the center of CNT pillar develops similar features to these of the CNT interfacial region as shown in Fig. 2.6(b). As a result the CNT interfacial region resistance  $R_{\text{CNT,IR}}$  diminishes. Therefore, the junction thermal resistance  $R_j$  will be lower than that in other cases.

To show these arguments more quantitatively, an overlap factor  $\eta$  is defined between the LDOS of two different regions named region 1 and region 2 as

$$\eta = \frac{\int_0^{+\infty} \min\{D_1(\omega), D_2(\omega)\} d\omega}{\int_0^{+\infty} D_1(\omega) d\omega}, \quad (2.6)$$

where  $D_1$  and  $D_2$  are the normalized LDOS of region 1 and region 2. The numerator of Eq. 2.6 means the overlap area between region 1 and region 2, while the denominator means the normalized LDOS area of a region. Hence a high overlap factor  $\eta$  means a small mismatch between two regions.

We have calculated the LDOS overlap factor  $\eta$  between CNT interfacial region and center region, as well as  $\eta$  between graphene interfacial region and CNT interfacial region as a function of  $PL$ .  $\eta$  between CNT center and CNT interfacial regions determines the CNT interfacial region resistance  $R_{\text{CNT,IR}}$ , and  $\eta$  increases with the decrease of  $PL$  as shown in Fig. 2.6(c). It indicates that  $R_{\text{CNT,IR}}$  will decrease when  $PL$  decreases. Conversely,  $\eta$  between the graphene interfacial and CNT interfacial regions, which dictates the boundary resistance  $R_{\text{B}}$ , changes little with the decrease of  $PL$  as shown in Fig. 2.6(c). These results are consistent with our decomposition results, and elucidate why as  $PL$  decreases,  $R_{\text{CNT,IR}}$  decreases, while  $R_{\text{B}}$  remains nearly the same. Here we show the overlap factor  $\eta$  for  $PL \leq 5.2$  nm, because  $\eta$  does not change noticeably for longer  $PL$ .

### 2.3.4 Network Model

After the junction thermal resistance is obtained, the thermal resistance of the entire pillared graphene structure ( $R_{\Sigma}$ ) can be calculated with a network model. The cross-plane thermal conductivity of the structure can be calculated based on Fourier's Law,

$$k = \frac{L}{R_{\Sigma}A_n}, \quad (2.7)$$

where  $A_n$  is the cross-sectional area of the network, and  $L$  is the length of the system in  $z$  direction.

Figure 2.7 provides a thermal conductivity comparison between our network model prediction and prior direct MD simulation results. [53] Both results with and without the CNT resistance are shown. Our prediction based on the network without CNT resistance agrees well with the MD results, and that with CNT resistance is lower than the direct MD result. This is a bit surprising since the former is supposed to over-predict the thermal conductivity, and the latter to agree with direct MD data. However, our simulation domain is only one cell of pillared graphene, and the junction resistance would be slightly overvalued because of the simulation domain

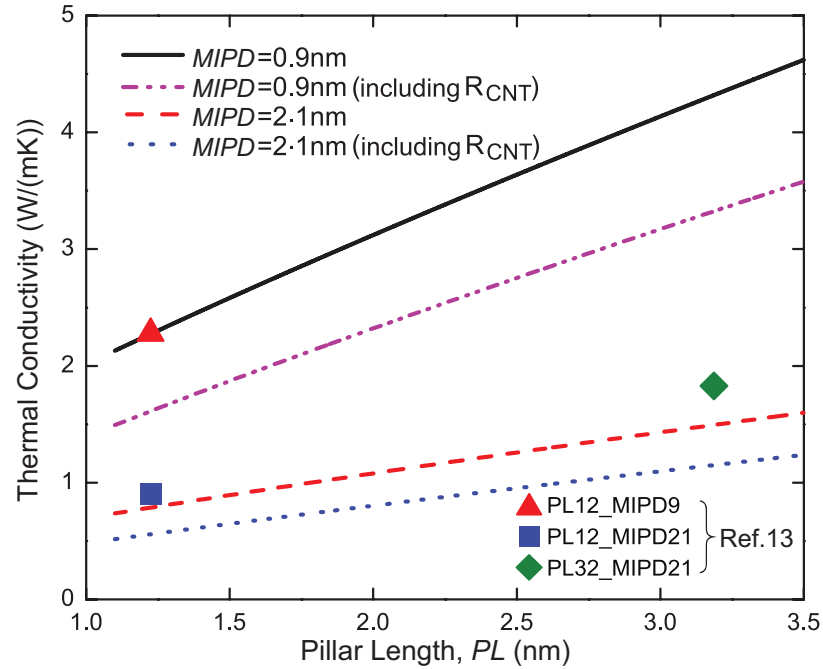


Figure 2.7. Comparison of system thermal conductivity predicted from our network model and from direct MD simulations in Ref.13. The black and red curves represent predictions of two  $MIPD$  cases for different  $PL$  without CNT resistances, the pink and blue curves represent those with CNT resistances, while the three symbols represent direct MD simulation results.  $PLm\_MIPDn$  indicates that  $PL$  equals  $m$  Angstrom, and  $MIPD$  equals  $n$  Angstrom.

size effect. This factor contributes to a reduction of thermal conductivity, making the results without the CNT resistance matching with direct MD data, while those with CNT resistance are under-estimated. Nevertheless, the network prediction results are reasonable even when the CNT resistance is neglected. However, when  $PL$  or  $MIPD$  becomes large, our assumption that the CNT and graphene resistances can be neglected will not be appropriate anymore. Instead these resistance should be included in the network model.

## 2.4 Summary

Because of the high thermal conductivity of both CNT and graphene, we show that the thermal resistance of pillared graphene structure is dominated by the CNT-graphene junction resistance, which can be confirmed by the large temperature jump at the junction and small temperature fall in CNT and graphene. Therefore, we have proposed to use the network model with junction thermal resistance as building blocks to find the total resistance of the structure. The non-equilibrium molecular dynamics is used to predict the junction thermal resistance, and the resistance of  $sp^2$  covalent junction is obtained to be about  $6 \times 10^{-11} \text{ m}^2\text{K/W}$ , which is much lower than typical thermal boundary resistance across other dissimilar materials. In contrast, the resistance across an individual CNT-graphene junction with van der Waals force is about  $4 \times 10^{-8} \text{ m}^2\text{K/W}$ . The  $sp^2$  covalent junction resistance is found to be primarily related to the pillar length  $PL$  of CNT and less to the inter-pillar distance  $MIPD$  or the reservoir distance  $RD$ , and it decreases as CNT pillar length  $PL$  decreases. To explore the underlying mechanism of this behavior, the junction resistance  $R_j$  is decomposed into one boundary resistance and two interfacial region resistances. We observed that the CNT interfacial region resistance  $R_{\text{CNT,IR}}$  decreases as  $PL$  decreases, while the boundary resistance  $R_B$  barely changes. This implies that change in the overall junction resistance with respect to  $PL$  is largely dictated by the CNT interfacial region resistance. We then used a local density of states (LDOS)

approach to further investigate this phenomenon, and found that the phonon spectra mismatch between the CNT interfacial region and the CNT center region decreases when the PL decreases, while the mismatch between graphene interfacial region and CNT interfacial region changes little, which is consistent with our decomposition result. The junction resistances are then put in series and parallel networks to easily interpret the thermal conductivity of such complicated and hierarchical structure. The thermal conductivity of the pillared graphene structure predicted by the network model agrees well with the direct simulation results. This indicates that our simple network model is effective in estimating thermal transport in hierarchical structures. Our work has revealed the critical role of junction resistance to thermal transport in pillared graphene structures, and the developed network model offers several orders of magnitude higher computation speed.

### 3. DECOMPOSITION OF THERMAL BOUNDARY RESISTANCE ACROSS CARBON NANOTUBE-GRAPHENE JUNCTIONS

#### 3.1 Introduction

Materials with high thermal conductivity are needed to effectively dissipate heat from electronic devices as we discussed in previous chapters. The properties of CNTs and graphene and their combination have been mentioned in Chapter 2, that although carbon nanotubes (CNTs) [14–16] and graphene [17–20, 80, 81] are promising high thermal conductivity materials, they both suffer from anisotropy in thermal transport [24]. Hence, the idea of constructing three-dimensional interconnected structures with CNT, graphene, or both as building blocks has been proposed to achieve good thermal conductivity in all directions [21, 53]. These structures are also attractive for potential energy storage applications due to their large surface area [21, 82–85], and it is timely to investigate their thermal properties. A pillared graphene system is one of these structures that has been synthesized recently [40]. Previous nonequilibrium molecular dynamics (NEMD) simulations in last chapter indicate that its thermal resistance primarily derives from CNT-graphene junctions [24]. However, the NEMD method gives only an overall thermal boundary resistance with few physical insights, and the thermal transport across an individual junction is not well understood.

In this paper, we attempt to identify the different mechanisms and decompose the thermal resistance across a single CNT-graphene junction. We construct a series of structures to associate with each mechanism, and the NEMD method is used to calculate the thermal boundary resistances. The relation between thermal boundary resistance and number of defects at the interface is studied. The turning angle dependence of boundary resistance is also explored.

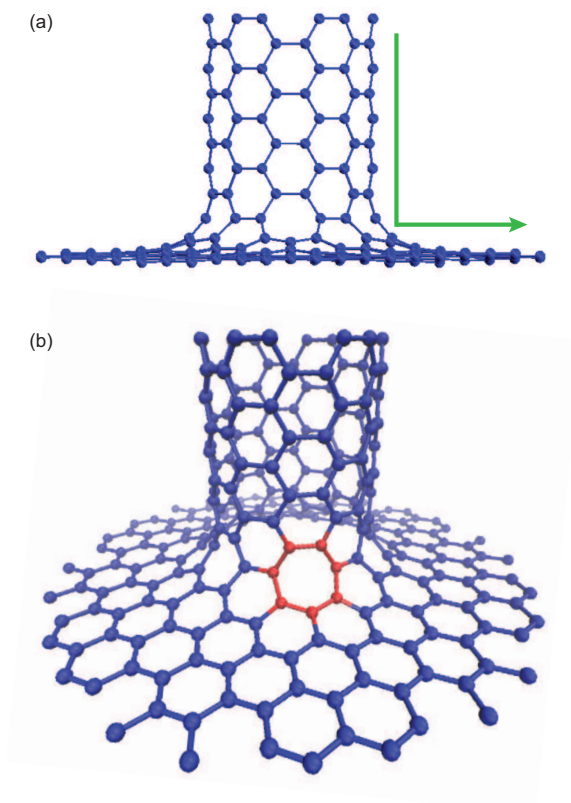


Figure 3.1. Orthogonal front view (a) and perspective view (b) of the detailed structure of a single CNT-graphene junction in pillared graphene. Red atoms form a heptagon.

### 3.2 Methodology

In earlier work [24], it is found that the resistance in pillared graphene mainly originates from the CNT-graphene junction, and the diffusive limit of the junction resistance is about  $7.5 \times 10^{-11} \text{ m}^2\text{K/W}$ . This value is very low compared to other interfaces because of the strong  $sp^2$  covalent bonding and absence of atomic mass mismatch. However, the junctions still introduce considerable overall resistance to the CNT-graphene network because of the extremely high thermal conductivity of CNTs and graphene. After inspecting the structure, we identified three possible mechanisms to investigate: materials mismatch, defects, and non-planar interfaces.

Material mismatch involves phonons transport from one material (CNT) to a different material (graphene) as shown in Fig. 4.1(a), and the resistance comes from different phonon dispersion relations of CNT and graphene. Defects arise from six heptagons at the CNT-graphene junctions as shown in Fig. 4.1(b) that introduce phonon-defect scattering. Non-planar junctions require phonons to change the propagation direction by  $90^\circ$  as shown in Fig. 4.1(a), and the resistance comes from the change of phonon momentum. These mechanisms are coupled, and NEMD simulations can only give the overall resistance at the junction but not isolate different mechanisms. Hence, we have designed a series of related structures to decouple these mechanisms.

To isolate the defects mechanism, the single-vacancy defect [86] shown in Fig. 4.2(a) and Stone-Wales defect [87] shown in Fig. 4.2(b), in a (6,6) CNT are considered where the non-planar interface and material mismatch mechanisms are absent. To isolate the material mismatch mechanism, the interface in an unzipped (6,6) CNT [88], as shown in Fig. 4.2(c), is considered since it involves only material mismatch across CNT and graphene interface, and does not involve any non-planar junction or defect mechanisms. For the non-planar interface mechanism, a 30-degree turning interface between a (6,6) CNT and (10,0) CNT [22], as shown in Fig. 4.2(d), and a 90-degree turning interface between a (6,6) CNT and (10,0) CNT, as shown in Fig. 4.2(e), are

considered. It should be noted that these turning CNTs also involve some degree of materials mismatch (from chirality) and defects (pentagon and heptagon) due to the difficulty of identifying model CNT or graphene systems with the non-planar interface mechanism only.

At the single-vacancy defect (Fig. 4.2(a)), one carbon atom is missing. At the Stone-Wales defect (Fig. 4.2(b)), one carbon-carbon bond turns vertically, and as a result, two pentagons and two heptagons are introduced into the pure (6,6) CNT previously with only hexagons. At the interface of an unzipped CNT (Fig. 4.2(c)), the (6,6) CNT gradually transitions to a flat graphene nanoribbon. For the 30-degree turning CNT (Fig. 4.2(d)), a pentagon gives a positive Gaussian curvature, while a heptagon gives a negative Gaussian curvature on the opposite side. The non-zero Gaussian curvature introduced by the heptagon and pentagon gives the cylindrical CNT a 30-degree turning. The interface of the 90-degree turning CNT (Fig. 4.2(e)) is three 30-degree turning interfaces in series.

In order to obtain the interface thermal resistances of five different structures, NEMD simulations [24,53,55] with the LAMMPS package are performed. The lengths of these structures along the heat transfer direction between two reservoirs are 100 nm, and the interface is at the center of the simulation domain. The lengths of the heat source and sink are both 10 nm. Interactions among carbon atoms are described by the AIREBO potential [72], and the simulation time step is 0.4 fs. In a previous comparison study of different potentials [89], it is found that the optimized Tersoff potential [90] is more accurate to describe phonon thermal properties of CNT and graphene. Here we use the AIREBO potential because we want to compare to the previous results [24,53] without any inconsistency of atomic potentials. In the simulation, a canonical NVT ensemble is run for 1.2 ns to relax the structure at first, allowing it to reach thermal equilibrium at 300 K. Then it is switched to the microcanonical NVE ensemble. A constant heat flux is then added to the heat source and extracted from the heat sink for the next 8 ns. After the system reaches steady state, the temperature of each small bin is obtained by averaging over ten million

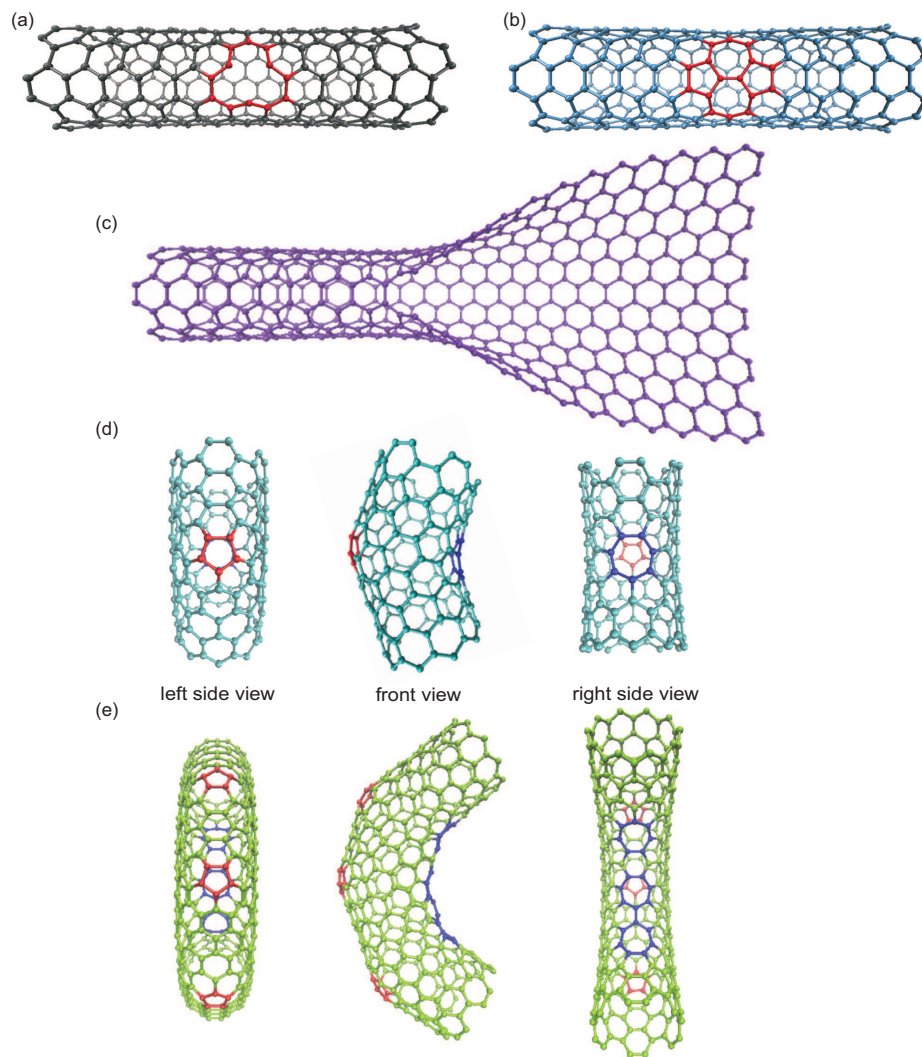


Figure 3.2. Interface structure of single-vacancy defect (a), Stone-Wales defect (b), unzipped (6,6) CNT (c), and the left side view, front view, right side view of 30-degree turning CNT (d) and 90-degree turning CNT (e).

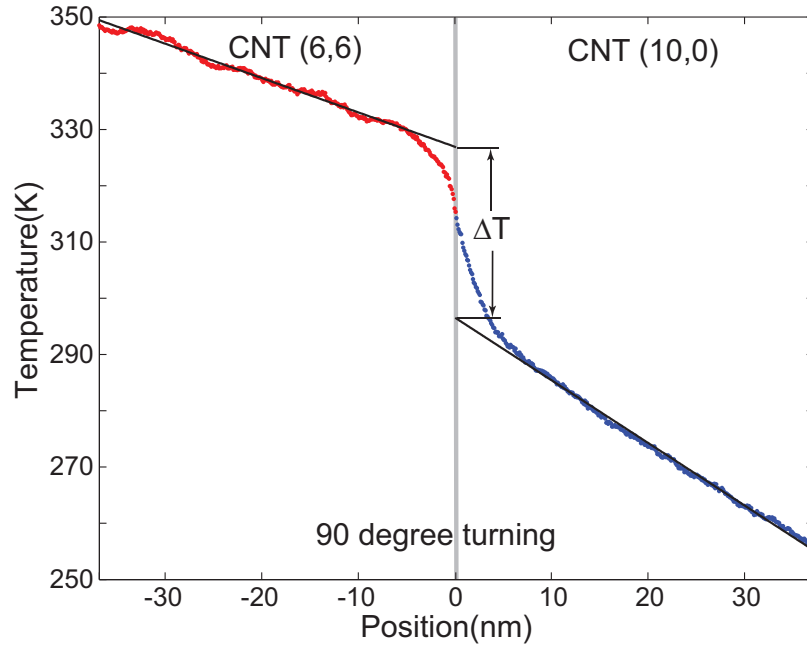


Figure 3.3. The temperature profile of 90-degree turning CNT in NEMD simulation.

time steps in the last 4 ns. The total number of temperature bins of (6,6) CNT from the reservoir to the interface is 406 and there is a half primitive cell (12 atoms) in each bin. For the graphene nanoribbon, the same number of temperature bins is used and there are 12 atoms in each bin since it is the unzipped (6,6) CNT. For the (10,0) CNT the number of temperature bins from the reservoir to the interface is 234 and there is a half primitive cell of (10,0) CNT (20 atoms) in each bin. Such temperature profiles are used to obtain thermal properties.

### 3.3 Results and discussion

#### 3.3.1 Junction resistance of different interfaces

Figure 4.7 shows the temperature profile of the 90-degree turning CNT in our simulation, and it is a typical temperature profile from NEMD. The temperature distributions in both the (6,6) and (10,0) CNTs are nearly linear, while at the interface

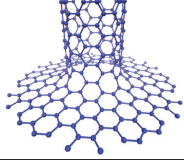
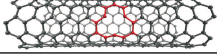
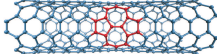
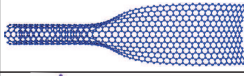
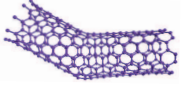
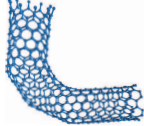
an abrupt temperature jump exists. Hence after linear fitting, the temperature jump  $\Delta T_j$  at the junction can be calculated. The junction thermal resistance  $R_j$  is given by

$$R_j = \frac{A_c \Delta T_j}{q}. \quad (3.1)$$

Here  $q$  is the heat flow rate,  $A_c$  is the cross-sectional area of a CNT. The value of  $A_c$  is  $8.57 \times 10^{-19} \text{ m}^2$  for all five junctions, approximated as a circular ring of thickness 0.335 nm and radius 4.07 nm (average of inner and outer radius) which equals to the radius of the (6,6) CNT.

The thermal resistances of all the interfaces studied are shown in Table 3.1. The junction resistances of the single-vacancy and Stone-Wales are  $2.3 \times 10^{-11} \text{ m}^2\text{K/W}$  and  $1.9 \times 10^{-11} \text{ m}^2\text{K/W}$  respectively, which are approximately 1/3 of the resistance of the CNT-graphene junction. The resistance of a single-vacancy is larger since one atom is missing, and three C-C bonds disappear because of the missing atom, while the number of C-C bonds does not change with the existence of Stone-Wales defect. The heptagonal defect (Fig. 4.1(b)) at the CNT-graphene junction is similar to the Stone-Wales defect since the number of C-C bonds does not decrease. The unzipped CNT junction shows a resistance of  $2.8 \times 10^{-11} \text{ m}^2\text{K/W}$ , which is also around 1/3 of the CNT-graphene junction resistance, again due to the fact that it only has one resistance mechanism (materials mismatch) out of the three. At the interface of unzipped CNT, only the material mismatch mechanism between (6,6) CNT and graphene exists. Hence, the resistance introduced by the material mismatch mechanism is also about 1/3 of the pillared graphene interface. The resistance from the 30-degree turning CNT junction is about  $5.3 \times 10^{-11} \text{ m}^2\text{K/W}$ , which is larger than those from the single-vacancy defect, Stone-Wales defect and unzipped CNT junction. This is probably because it involves not only the non-planar interface mechanism, but also defects (heptagon and pentagon) and material mismatch (from (6,6) CNT to (10,0) CNT). The resistance at the junction of the 90-degree turning CNT is about  $1.6 \times 10^{-10} \text{ m}^2\text{K/W}$ , which is three times that of the 30-degree turning junction. This result is reasonable since the 90-degree turning interface is just three 30-degree turning inter-

Table 3.1. The interface thermal resistance results from NEMD of different interfaces.

name	structure	defects	non-planar	material mismatch	NEMD $R''$ (m <sup>2</sup> K/W)
pillared graphene		X	X	X	$7.5 \times 10^{-11}$
single-vacancy		X			$2.3 \times 10^{-11}$
Stone-Wales		X			$2.0 \times 10^{-11}$
unzipped CNT				X	$2.8 \times 10^{-11}$
turning CNT		X	X	X	$5.3 \times 10^{-11}$
vertically turning CNT		X	X	X	$1.6 \times 10^{-10}$

faces in series, and it shows that three 30-degree turning interfaces are not coupled. Our calculation indicates that all three mechanisms (defect, material mismatch, non-planar interface) contribute nearly equally to the CNT-graphene junction resistance.

### 3.3.2 Error analysis

There are statistical and systematic errors in the NEMD simulations [91]. The statistical error of thermal boundary resistance from NEMD simulations is usually considered small. To verify that our results are reliable, six separate NEMD simulations were conducted on the same (6,6) CNT with Stone-Wales defect structure with different initial atom velocities in the MD simulations generated from different seeds. The results of the thermal boundary resistance at a Stone-Wales defect from six trials are shown in Fig. 3.4(a). The results from different trials are very similar to each other and close to the average. The standard deviation for this sample of six

independent simulations is only 5.4% of the average resistance, and the uncertainty should be small.

The most important systematic error in NEMD simulations of thermal boundary resistance comes from the finite-size effect [24,55,92,93]. The domain-size dependence of thermal boundary resistance in NEMD simulations is because that the largest phonon wavelength is directly determined by the domain size, and long mean free path phonon can ballistically transport through if the mean free path is larger than or comparable to the domain size. Hence, to find the diffusive limit, a domain size which is large enough is needed. The relation between the domain size and the thermal boundary resistance at the Stone-Wales defect is studied to find the proper simulation domain length. The results of boundary resistance with different domain sizes are shown in Fig. 3.4(b). From the results it can be seen that when  $L$ , the CNT length between two reservoirs, is larger than 80 nm, the resistance nearly does not change with the increase of  $L$ . In our simulation,  $L$  is 100 nm, and it should be reasonable to assume that the results from our NEMD simulations reach the diffusive limit.

### 3.3.3 Relation between resistance and the number of defects

The relation between the junction thermal resistance and the number of defects is studied here since there are six heptagon defects at the CNT-graphene junction. The defects can be either in series (defects are distributed along CNT axial direction) or in parallel (defects are distributed evenly perpendicular to CNT axial direction) as shown in Fig. 3.5, and both cases with single-vacancy or Stone-Wales defect have been explored.

As shown clearly in Table 3.2, the relation between total resistance of defects in series and the number of defects follows a similar trend for both single-vacancy and Stone-Wales defect. The total resistance of two and three single-vacancy defects in series are 1.4 and 2.2 times the resistance of one single-vacancy defect respectively,

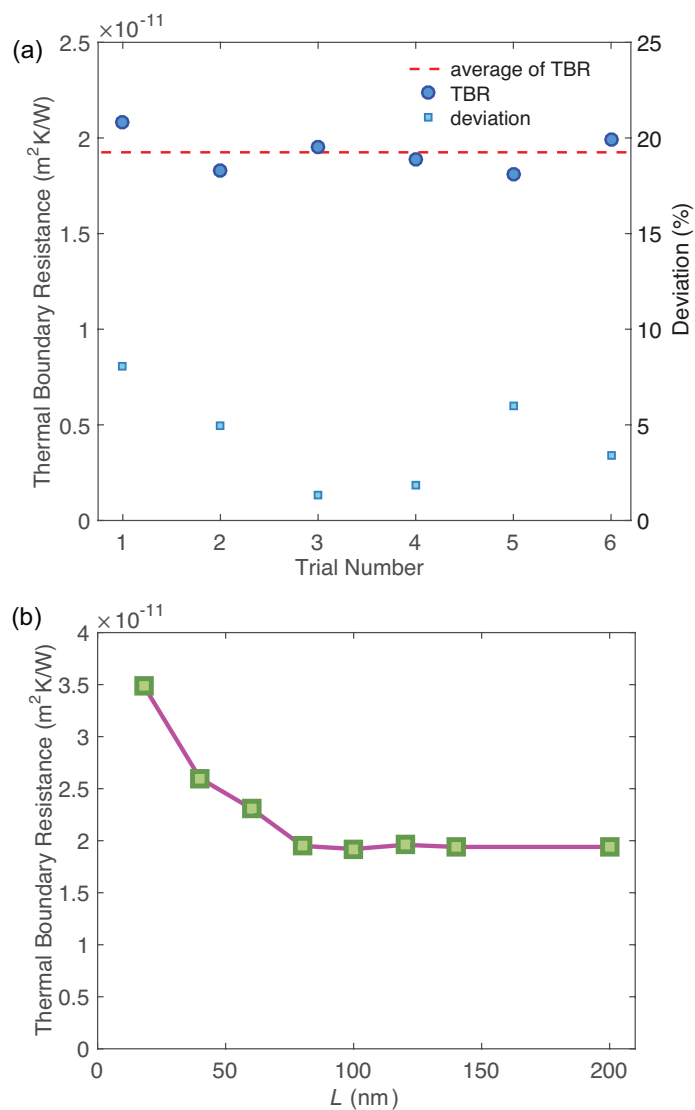


Figure 3.4. (a) The thermal boundary resistance (TBR) results and the corresponding deviation percentage from the average at a Stone-Wales defect in (6,6) CNT with different initial velocities from NEMD simulations (the left axis is the scale of thermal boundary resistance, the right axis is the scale of deviation percentage). The red dashed-line is the average thermal boundary resistance of the six trials. (b) The thermal boundary resistance results at a Stone-Wales defect in (6,6) CNT with different domain sizes in NEMD simulations.  $L$  is the length of CNT along the heat transfer direction between reservoirs.

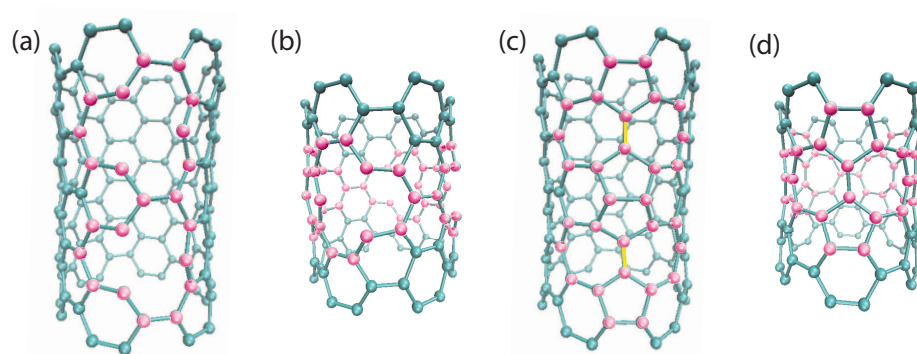


Figure 3.5. (a) Two single-vacancy defects in series, (b) four single-vacancy defects in parallel, (c) two Stone-Wales defects in series, (d) three Stone-Wales defects in parallel. Pink atoms are directly affected by defects.

while the total resistance of two and three Stone-Wales defects in series are 1.3 and 2.1 times the resistance of one Stone-Wales defect respectively. It indicates that these defects in series are coupled when they are very close to each other, and as a result, the total resistance is smaller than the number of defects times the resistance of a single defect.

For the defects in parallel, the total resistance of two and three single-vacancy defects in parallel are 1.7 and 3.2 times the resistance of one single-vacancy defect respectively, and the resistance of two and three Stone-Wales defects in parallel are 1.9 and 3.9 times the resistance of one Stone-Wales defect respectively. Unlike the defects in series, the total resistance of defects in parallel can be larger than the resistance of a single defect times the number of defects. Moreover, as mentioned earlier that the resistance of one single-vacancy defect is larger than the resistance of one Stone-Wales defect because of the reduced number of C-C bonds. However, the total resistance of more than two single-vacancy defects is smaller than the corresponding resistance of Stone-Wales defect. These phenomena can be explained by that, as shown in Fig. 4.1 (a) and (b), there are 12 columns of hexagons in the axial direction of (6,6) CNT, and for one single-vacancy defect, 2 columns will be directly affected, while for one Stone-Wales defect, three columns will be directly affected. The total resistance of four and six single-vacancy defects in parallel are 4.5 and 7.3 times the resistance of one single-vacancy defect, respectively. If we consider the hexagon columns not directly affected, for 4 single-vacancy defects in parallel, only 4 columns (1/3 of the total) are not directly affected, while for 6 single-vacancy defects in parallel, all the columns are affected. Hence, with the existence of defects in parallel, the total resistance might be higher than the defect number times the resistance of a single defect. Also, since one more hexagon column will be affected by Stone-Wales defect than by single-vacancy, with the increase of defect number, the hexagon columns not directly affected by Stone-Wales defects will be much less than those by single-vacancy defect for the same number of defects. Therefore, it is reasonable that the total resistance of Stone-Wales defect exceeds that of single-vacancy defect when the defect number is large.

Table 3.2. The NEMD interface thermal resistance results of different number of defects.

defect type	number of defects	in series	in parallel	NEMD $R''$ ( $\text{m}^2\text{K}/\text{W}$ )
single-vacancy	2	X		$3.4 \times 10^{-11}$
	3	X		$5.2 \times 10^{-11}$
	2		X	$3.9 \times 10^{-11}$
	3		X	$7.5 \times 10^{-11}$
	4		X	$1.0 \times 10^{-10}$
	6		X	$1.7 \times 10^{-10}$
Stone-Wales	2	X		$2.6 \times 10^{-11}$
	3	X		$4.2 \times 10^{-11}$
	2		X	$3.7 \times 10^{-11}$
	3		X	$7.8 \times 10^{-11}$

At the CNT-graphene junction, each of the 6 heptagon defects in parallel only affects one column of C-C bonds, and as a result, the resistance from defects is relatively small compared to single-vacancy and Stone-Wales defect. Considering there are 6 columns of hexagons are affected at the CNT-graphene interface, the resistance from defects at the interface should be comparable to but smaller than that of 2 Stone-Wales defects in parallel (because 3 columns of hexagons are affected for each Stone-Wales defect), which is  $3.7 \times 10^{-11} \text{ m}^2\text{K}/\text{W}$ . Hence, the estimated value for the CNT-graphene junction thermal resistance from defects is about  $3 \times 10^{-11} \text{ m}^2\text{K}/\text{W}$ , which is about 1/3 of the total resistance at the CNT-graphene junction.

### 3.3.4 Relation between resistance and turning angle

Now we explore further how an abrupt versus gradual turning angle affects interface thermal resistance across the CNT-graphene junction by a CNT-nanocone-graphene structure. By changing the apex angle of the carbon nanocone between CNT and graphene, we can tune the phonon transport path as shown in Fig. 3.6. The NEMD method with the same simulation time step and number of steps has been used in our calculation. The length of the (6,6) CNT is 50 nm, the height of the

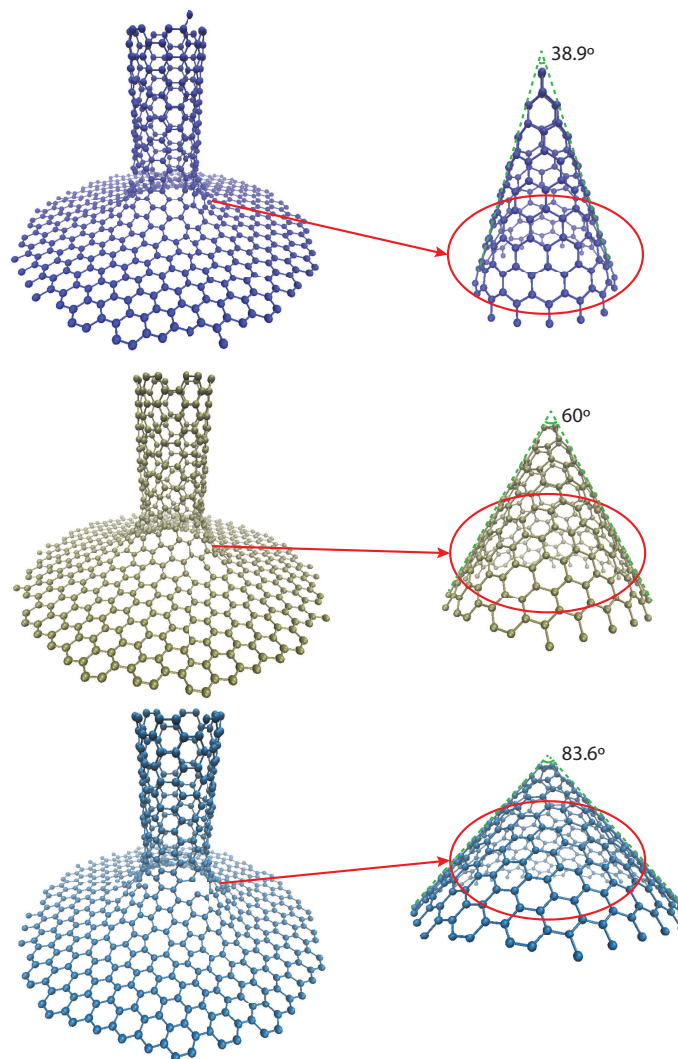


Figure 3.6. The CNT-nanocone-graphene structures with different carbon nanocone apex angles.

nanocone between CNT and graphene sheet is 0.6 nm, and the graphene is  $31 \times 31$  nm. The resistances of 38.9 degree, 60 degree, 83.6 degree apex angle nanocone interface are  $1.9 \times 10^{-10}$  m<sup>2</sup>K/W,  $1.8 \times 10^{-10}$  m<sup>2</sup>K/W, and  $1.9 \times 10^{-10}$  m<sup>2</sup>K/W, respectively. There is not much difference from different CNT-nanocone-graphene structures, probably because there are a lot of defects at the interface, rendering the main mechanism leading to resistance to be defects. As a result, the resistance is not sensitive to different nanocone apex angle.

### 3.4 Conclusion

To summarize, we have identified three mechanisms which can lead to thermal resistances across the pillared graphene junction: the material mismatch, the non-planar junction, and defects. NEMD simulations have been performed to compare five types of different junctions (unzipped CNT, CNT with single-vacancy, CNT with Stone-Wales defects, 30-degree CNT-CNT junction, and 90-degree CNT-CNT junction) corresponding to different mechanisms. The corresponding junction thermal resistance results from NEMD show that the junction resistances from different mechanisms are on the same order of magnitude. Both defect number and turning angle dependence of thermal boundary resistance have been explored. The results show that the defects in series are coupled and the total resistance is smaller than the defect number times the resistance of a single defect. For the defects in parallel, the total resistance is related to the number of CNT hexagon columns affected by the defects. If the defects are very dense, the resistance can be higher than the defect number times the resistance of a single defect. These findings can be used to estimate the resistance at the interface of carbon-based hierarchical structures.

## 4. PHONON POLARIZATION CONVERSION ACROSS DIMENSIONALLY MISMATCHED INTERFACES: CARBON NANOTUBE-GRAPHENE JUNCTION

### 4.1 Introduction

From the introduction and our own work as shown in the chapters before, we know that thermal interfacial resistance is a critical issue for thermal management of modern electronic devices. Planar interfaces have been extensively studied, and theories such as the acoustic mismatch model (AMM) [48] have been successfully developed to predict mode-resolved phonon transport. On the other hand, dimensionally mismatched non-planar interfaces, such as 1D-2D [21, 23, 24, 39, 40], 1D-3D [42–45], and 2D-3D [16, 46, 47] interfaces, are emerging for many applications, but existing theories may not describe their thermal interfacial transport correctly due to new physics introduced by the dimensional mismatch. Attempt of modified acoustic mismatch model has been made at 1D-3D interface [45], but has not been compared with simulation or experimental results. As an example of dimensionally mismatched interface, the current work will consider CNT-graphene junction, which is an interface between 1D and 2D materials and is the building block for CNT-graphene 3D networks recently proposed and synthesized [21, 23, 24, 39, 40]. Although CNTs [14–16] and graphene [17–20, 80] have very high thermal conductivity, they both suffer from anisotropy in thermal transport. The thermal conductivity of graphene stacks or graphite in the cross-plane direction is two or more orders of magnitude lower than that of the in-plane direction [51]. CNT bundles also show similar behavior in the radial direction [52]. Therefore, the above mentioned 3D CNT-graphene network was proposed to achieve high thermal conductivity in all directions. Our previous nonequilibrium molecular dynamics (NEMD) simulations indicate that the thermal resistance in the

network primarily comes from CNT-graphene junctions [24]. However, the NEMD method gives only an overall thermal boundary resistance without any physical insights associated with the unique dimensional mismatch nature. The CNT-graphene junctions have been synthesized in experiment [40], but interfacial thermal transport has not been measured yet. Hence, it is a timely task to understand interfacial thermal transport physics across the 1D-2D junction and assess the validity of the existing theoretical models. The results will lend useful insights for 1D-3D and 2D-3D interfaces as well.

We report the modal phonon transmission process at CNT-graphene junctions using the wave packet method [43, 57, 94, 95], which is an accurate spectral phonon transmission simulation method. The junction is between a (6, 6) CNT and graphene sheet with  $sp^2$  covalent bonds. The schematic of the simulated structure is shown in Fig. 4.1(a). We have found intriguing phonon polarization conversion behavior during the transmission process for all incident modes from CNT, i.e., they partially convert to different phonon polarizations in graphene after the transmission. Such surprising behavior cannot be captured by the conventional mismatch models.

## 4.2 Methodology

The molecular dynamics (MD) phonon wave packet method is implemented with the LAMMPS package. We used the classical molecular dynamics, since only a single mode wave packet is launched in each simulation and quantum factors are not important. The detailed structure of the CNT-graphene junction is shown in Fig. 4.1. The interactions between carbon atoms in lattice dynamics calculations and MD simulations are based on the polymer consistent force field (PCFF) [96, 97]. The phonon dispersion relation and mode eigenvectors of (6, 6) CNT are first calculated. To create a wave packet for a specific phonon mode, the initial displacement from equilibrium and velocity of the  $i$ th base atom in the  $n$ th unit cell along the  $\alpha$  direction are [39],

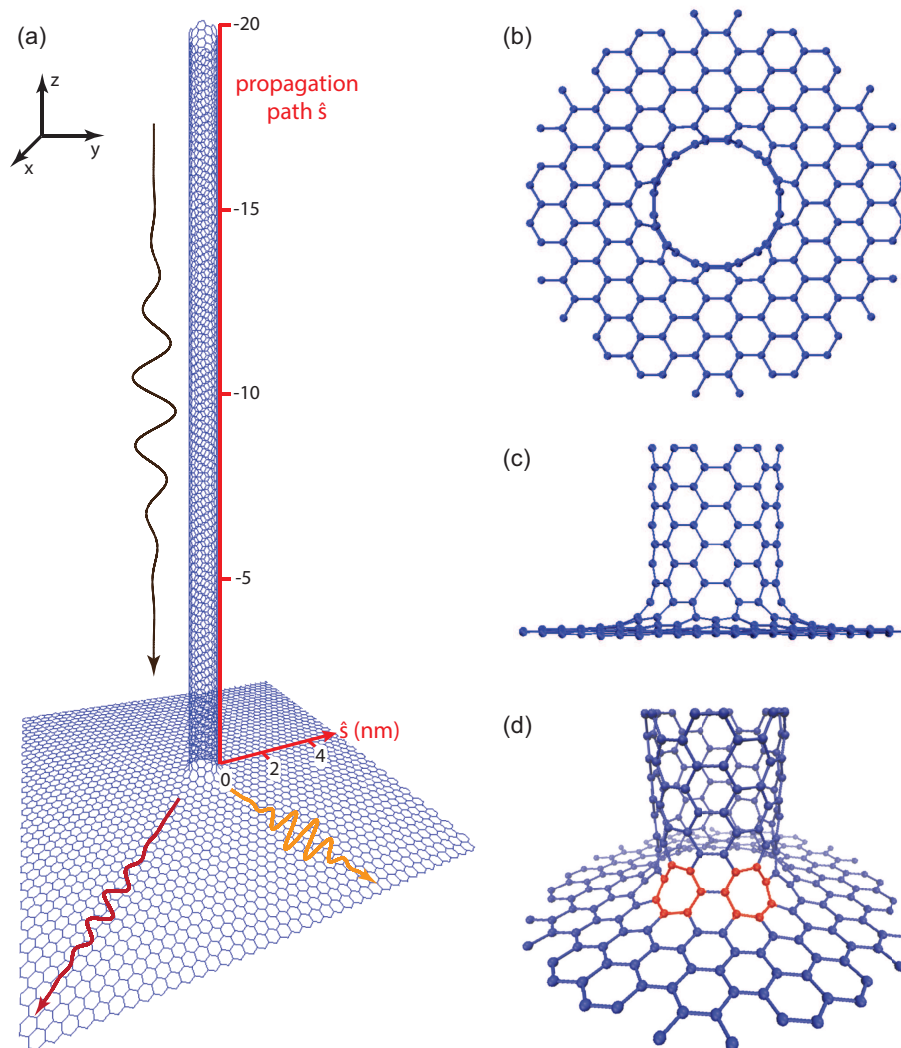


Figure 4.1. (a) Schematic of the pillared graphene structure used in this work. Top view (b) and front view (c) of the detailed junction structure. (d) Detailed junction structure with perspective, where the heptagon defects are highlighted with red.

$$u_{ni\alpha}^{\gamma} = \frac{A}{\sqrt{M}} \sum_q \exp \left[ -\frac{(q - q_0)^2}{2\sigma^2} \right] \varepsilon_{i\alpha}^{\gamma}(q) \exp [iq(z_n - z_0)], \quad (4.1)$$

$$v_{ni\alpha}^{\gamma} = \frac{A}{\sqrt{M}} \sum_q -i2\pi v^{\gamma}(q) \exp \left[ -\frac{(q - q_0)^2}{2\sigma^2} \right] \varepsilon_{i\alpha}^{\gamma}(q) \exp [iq(z_n - z_0)], \quad (4.2)$$

where  $A$  is the amplitude,  $M$  is the carbon atom mass,  $q_0$  is the wavenumber of the packet,  $z_0$  and  $z_n$  are the positions of the packet center and the  $n$ th unit cell in the CNT along the propagation path  $\hat{s}$ , and  $\varepsilon$  is the eigenvector of the phonon with wavenumber  $q$  and polarization  $\gamma$ . As shown in Fig. 4.1(a), the phonon wave packet is activated from the CNT with a specific polarization  $\gamma$  and propagates towards the graphene sheet.

After the wave packet reaches the junction, the transmitted part continues to propagate into graphene, and the reflected part propagates back to the CNT as shown in Fig. 4.2(a)-(c). Monitoring the amount of energy transmitted or reflected at the junction enables the calculation of the energy transmission coefficient of the specific phonon mode. For the reflected part, the wavenumber can be calculated using the Fourier transform of atom velocity at different positions, and the frequency can be calculated using the Fourier transform of atom velocity at different time. For the transmitted part in graphene, the energy propagates in the radial direction, so the velocity of an array of atoms along the radius scaled by the square root of radius  $v \cdot \sqrt{r}$  is used in the Fourier transform. According to Parseval's theorem, the energy of each transmitted wave packet with a specific wavenumber can be calculated by the integral over the square of the amplitude of Fourier transform result. Because of the anisotropy in graphene, the transmission coefficients are different along different radial directions. Hence, both the zigzag and armchair directions are used in the Fourier transform and are averaged to determine the overall transmission coefficient. The details of the calculation of transmission coefficient is shown below. For the

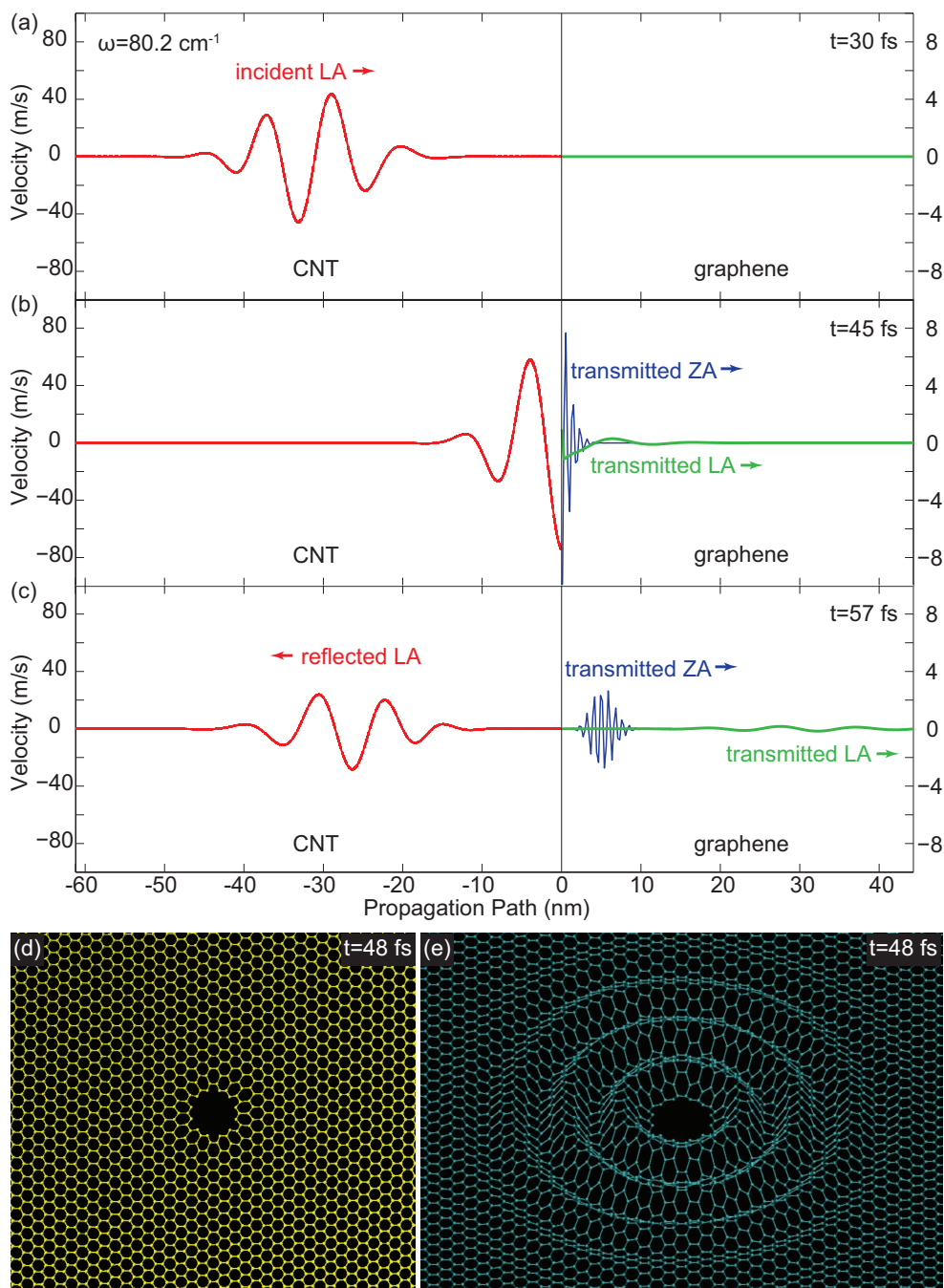


Figure 4.2. Typical wave packet propagation process for an incident LA mode from CNT. Atom velocity (the left axis is the scale of atom velocity in CNT, the right axis is the scale of atom velocity in graphene) plot before the wave packet reaches the interface (a), when the wave packet just reaches the interface (b), after transmission (c). (d) In-plane displacements (amplified by 600 times) of graphene atoms. (e) Out-of-plane displacements (amplified by 600 times) of graphene atoms.

calculation of reflected wave packet in  $k$ -space, the velocity of a row of equidistant atoms in CNT along the axial direction is used to do the Fourier transform. The Fourier transform of the atom velocity is

$$f(k) \propto \int_{-\infty}^{+\infty} v(z)e^{-i2\pi z} dz, \quad (4.3)$$

where  $k$  is the wave number, and  $z$  is the atom coordinate along the axial direction in CNT. The Fourier transform of the atom velocity is computed by the MATLAB fast Fourier transform (FFT) function. Because of Parseval's theorem, the kinetic energy of a specific mode  $Y$  is

$$E_Y = \int_{k_{\min,Y}}^{k_{\max,Y}} f(k)^2 dk, \quad (4.4)$$

where  $k_{\min,Y}$  and  $k_{\max,Y}$  are shown in Fig. 4.3.

For the calculation of transmitted wave packet in  $k$ -space, since the wave packet propagates in the radial direction in graphene, the kinetic energy will be diluted among atoms as the propagation distance increases. The kinetic energy of a single atom should be proportional to the reciprocal of the distance between the atom and the junction. Hence, to calculate the wave packet in  $k$ -space, the modified velocity of a row of equidistant atoms along the radial direction in graphene is used for Fourier transform. The modified velocity is

$$v'(r) = v(r) \cdot \sqrt{r}, \quad (4.5)$$

where  $r$  is the distance between the atom and the CNT center. The Fourier transform of the modified atom velocity is

$$f(k) \propto \int_{-\infty}^{+\infty} v'(r)e^{-i2\pi r} dr, \quad (4.6)$$

like the calculation of reflected part, the kinetic energy of a specific mode  $Y$  is

$$E_Y = \int_{k_{\min,Y}}^{k_{\max,Y}} f(k)^2 dk, \quad (4.7)$$

and the transmission coefficient from mode  $X$  to mode  $Y$  is

$$\Gamma_{X \rightarrow Y} = E_Y / E_{total}, \quad (4.8)$$

where  $E_{total}$  is the total kinetic energy of the incident wave packet.

From our simulation, it is found that the transmission coefficients are different along different directions. The different transmission coefficients are because of the anisotropy of graphene. The phonon dispersion relation curves of graphene based on polymer consistent force field (PCFF) [96,97] are different along different directions as shown in Fig. 4.4.  $\Gamma_{LA \rightarrow LA}$  along the zigzag and armchair directions in graphene are slightly different. However,  $\Gamma_{LA \rightarrow ZA}$  can be very different at high frequency. When the frequency of the incident wave packet is lower than the cutoff frequency from  $\Gamma$  point to K point (corresponding to zigzag direction), but higher than the cutoff frequency from  $\Gamma$  point to M point (corresponding to armchair direction) as shown by the cyan dashed line in Fig. 4.4, since the transmission process is elastic, zigzag and armchair directions will allow and forbid the ZA polarization propagation respectively. For instance, for the incident LA mode at  $355 \text{ cm}^{-1}$ , we plotted the out-of-plane velocity  $v_z$  (corresponding to the vibration of ZA branch) of atoms in graphene and found the out-of-plane vibration is indeed only in the zigzag directions but not the armchair directions as shown in Fig. 4.5. Therefore, the overall transmission coefficient is averaged over 12 different directions (6 zigzag directions and 6 armchair directions) as shown in Fig. 4.6.

We have confirmed energy conservation by checking that the sum of the transmitted and reflected energies equals the incident energy.

### 4.3 Results and Discussion

In the simulation, we launched wave packets of longitudinal acoustic (LA), transverse acoustic (TA), twisting (TW), and radial breathing (RB) polarizations with different wavenumbers in the CNT, because these acoustic polarizations and high group velocity polarizations are more important in thermal transport. These phonon modes are launched one at a time to predict mode-resolved transmission behavior. We find that the reflected phonon frequency, wavenumber and polarization remain

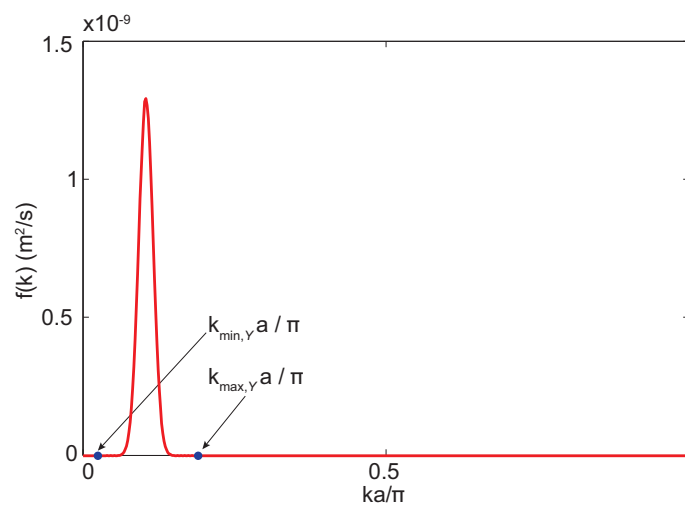


Figure 4.3. The wave packet in  $k$ -space.

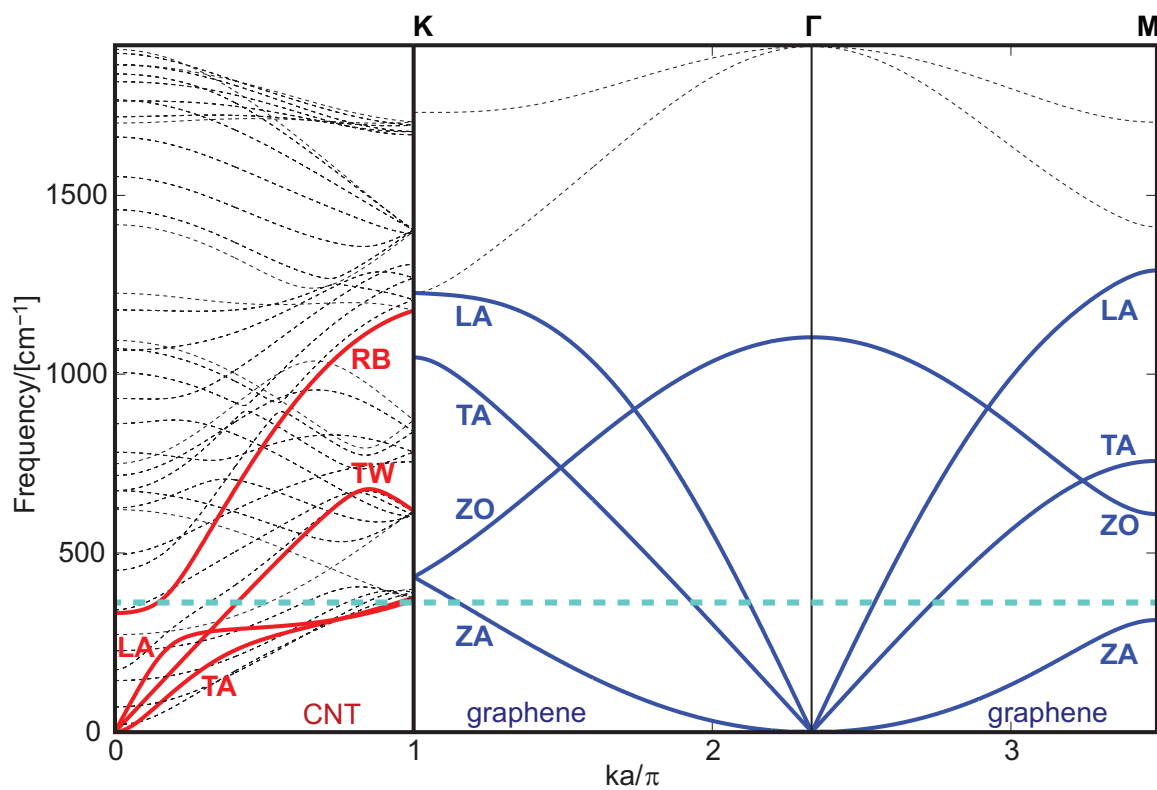


Figure 4.4. The phonon dispersion relation of CNT and graphene.

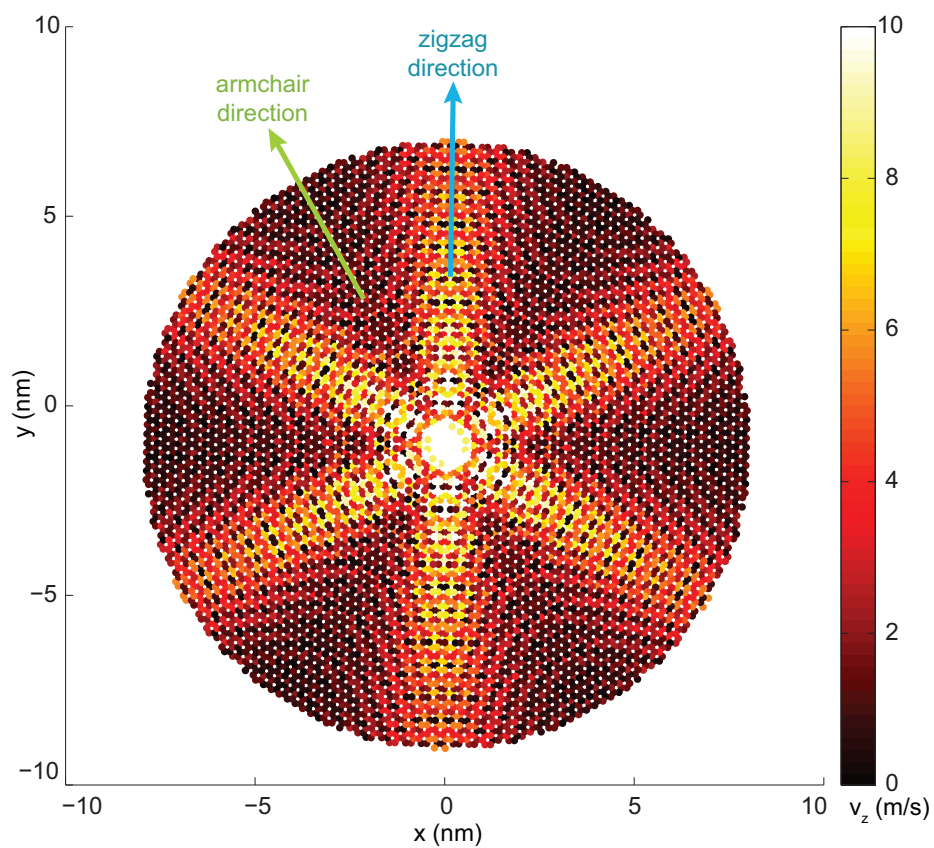


Figure 4.5. The out-of-plane velocity of atoms in graphene sheet during the incident LA mode wave packet transmission process. The phonon frequency is about  $355 \text{ cm}^{-1}$ .

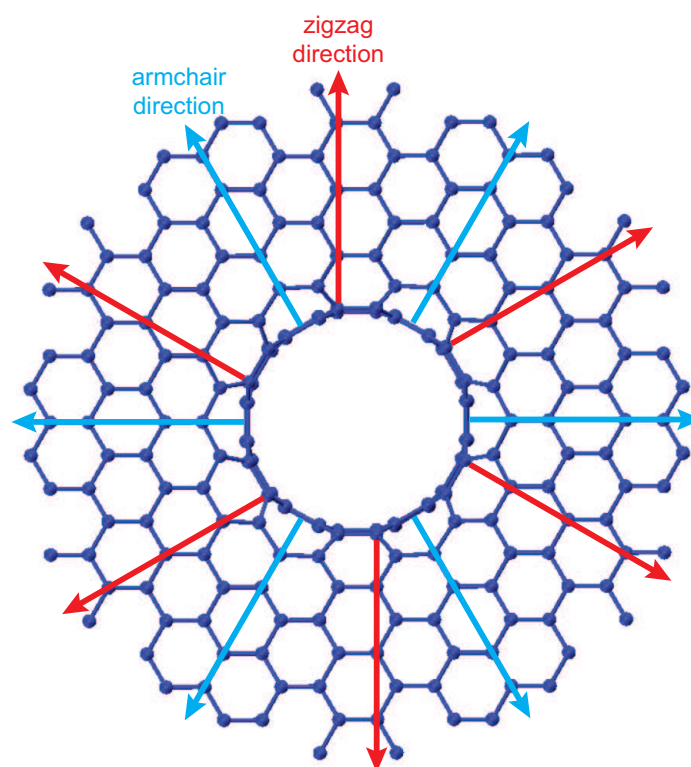


Figure 4.6. All the directions included for the averaging calculation of overall transmission coefficient.

the same as the incident mode, indicating an elastic reflection process. This can also be seen from Fig. 4.2(b), that the superposition of incident and reflected waves in the CNT near the interface has exactly the same wavelength as the incident wave packet.

However, the transmission shows surprising polarization conversion behavior, as shown in Fig. 4.2. The incident LA phonon polarization from CNT transmits into both LA and ZA polarizations in graphene, and the amplitude of the ZA polarization is much larger than that of the LA polarization, as shown clearly in Fig. 4.2(b) and (c). After the Fourier transform of modified atom velocities  $v \cdot \sqrt{r}$  at different positions in graphene, two transmitted modes with their respective wavenumbers are clearly seen as two peaks in graphene  $k$ -space as shown in Fig. 4.7(b). Since the phonon dispersion relation of graphene has been obtained, the polarizations can be confirmed according to their frequencies and wavenumbers. Using polarization and wavenumbers, we can identify these modes as two dots on LA and ZA branches of the graphene phonon dispersion relation respectively, as shown in Fig. 4.7(d). Despite polarization conversion, the frequency of these transmitted modes is the same as the incident LA mode in the CNT, as shown in Fig. 4.7(b) and (d), indicating that the transmission process is also elastic without anharmonic phonon scattering. Hence, the transmitted LA and ZA wave packets in graphene have different wavenumbers, wavelengths, and group velocities. Fig. 4.2(c) clearly shows that the LA and ZA wave packets propagate at different speeds. Fig. 4.2(d) and (e) show the in-plane and out-of-plane atomic displacements in graphene respectively, for an incident LA wave packet. Because the graphene LA polarization only has in-plane displacement and velocity, while the ZA polarization only has out-of-plane displacement and velocity, the decomposition in Fig. 4.2(d) and (e) indicates that both LA and ZA modes are indeed induced in graphene. Mode conversion behaviors have been observed before at silicon germanium interface with roughness [95], but that mode conversion is inelastic due to the anharmonic phonon scattering at the rough interface, and the effect is very small. Our polarization conversion due to dimensional mismatch is very different in that it is elastic and dominates the transmission.

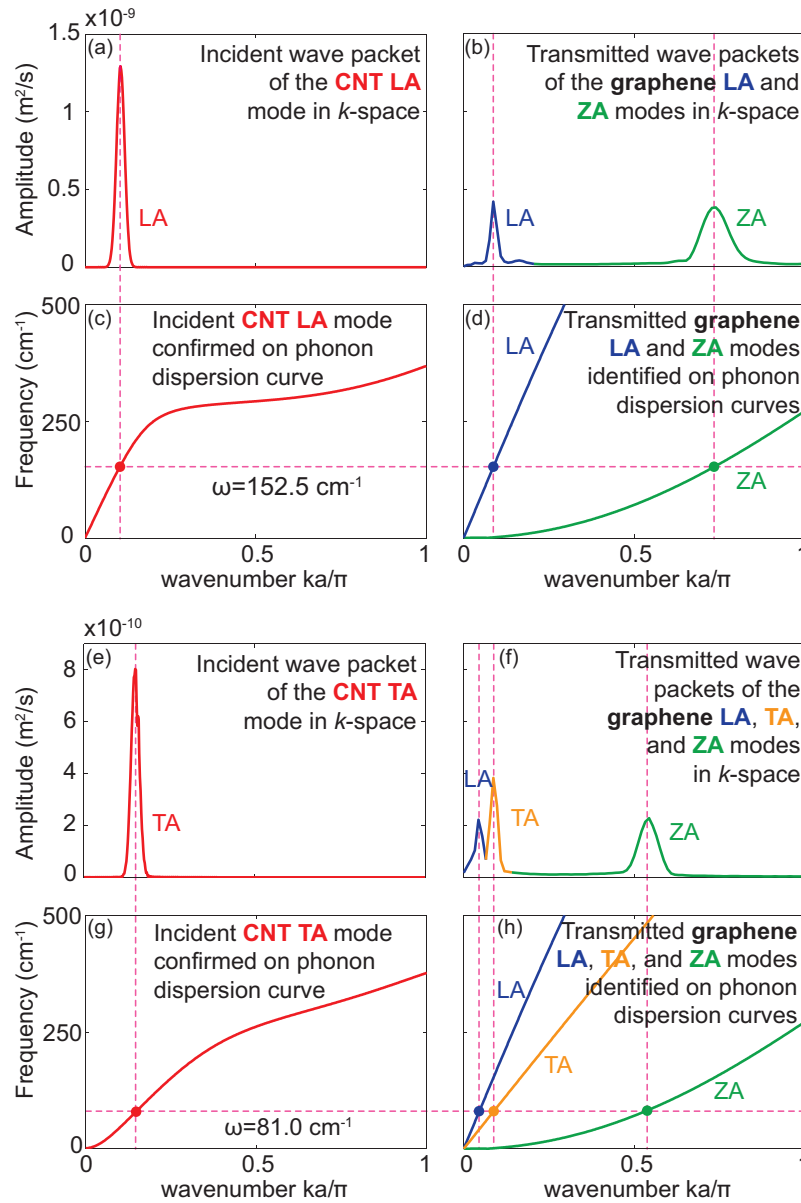


Figure 4.7. An incident CNT LA wave packet (a) and its transmitted graphene LA and ZA wave packets (b) in  $k$ -space, and the corresponding identified modes on CNT LA branch (c) and graphene LA and ZA branches (d), respectively. An incident CNT TA wave packet (e) and its transmitted graphene LA, TA, and ZA wave packets (f) in  $k$ -space, and the corresponding identified modes on CNT TA branch (g) and graphene LA, TA, and ZA branches (h), respectively.

Like the incident LA polarization from CNT, the incident TA and other polarizations also exhibit polarization conversion behavior after transmission. For the incident TA wave packet shown in Fig. 4.7(e), the transmission process is more complicated since the phonon eigenvector of the CNT TA polarization not only has axial and radial components like the LA, but also tangential component. The transmitted phonons into graphene are LA, TA, and ZA polarizations, as shown as three peaks in as shown in Fig. 4.7(f). The polarization conversion process is similar to the incident LA polarization, that the frequency does not change, and transmitted modes can be identified as three dots on the LA, TA, and ZA branches of the graphene dispersion relation, as shown in Fig. 4.7(g) and (h). For the incident TW polarization from the CNT, the transmitted polarizations are TA and ZA because the motion of the TW polarization in the CNT is along tangential direction, which has similar displacement as the TA polarization in graphene (in-plane transverse). For the incident RB polarization, the transmitted polarizations are LA and ZA just like the incident CNT LA polarization because the axial and radial displacements of the CNT RB polarization are similar to the displacement of the CNT LA polarization.

We attribute the unique polarization conversion behavior across the CNT-graphene to the special dimensionally mismatched structure of the system. During the transmission from one dimensional CNT to two dimensional graphene, the propagation direction of phonons must change 90 degrees as shown in Fig. 4.1. For a given incident mode such as an LA mode in CNT, some of the transmitted energy preserves the polarization without conversion, i.e. LA to LA, while the remaining transmitted energy preserves the direction of atomic vibrations and will change polarization, i.e. LA to ZA. We suspect that the polarization conversion behavior depends on the wavelength of the incident phonon wave; hence we investigate the transmission coefficient as a function of phonon frequency, which is directly related to wavelength.

In Fig. 4.8, we show the transmission coefficient of each individual incident phonon polarization, as well as the breakdown into different transmitted polarizations in graphene. The transmission coefficient  $\Gamma_{X_{\text{total}}}$  is defined as the transmitted energy

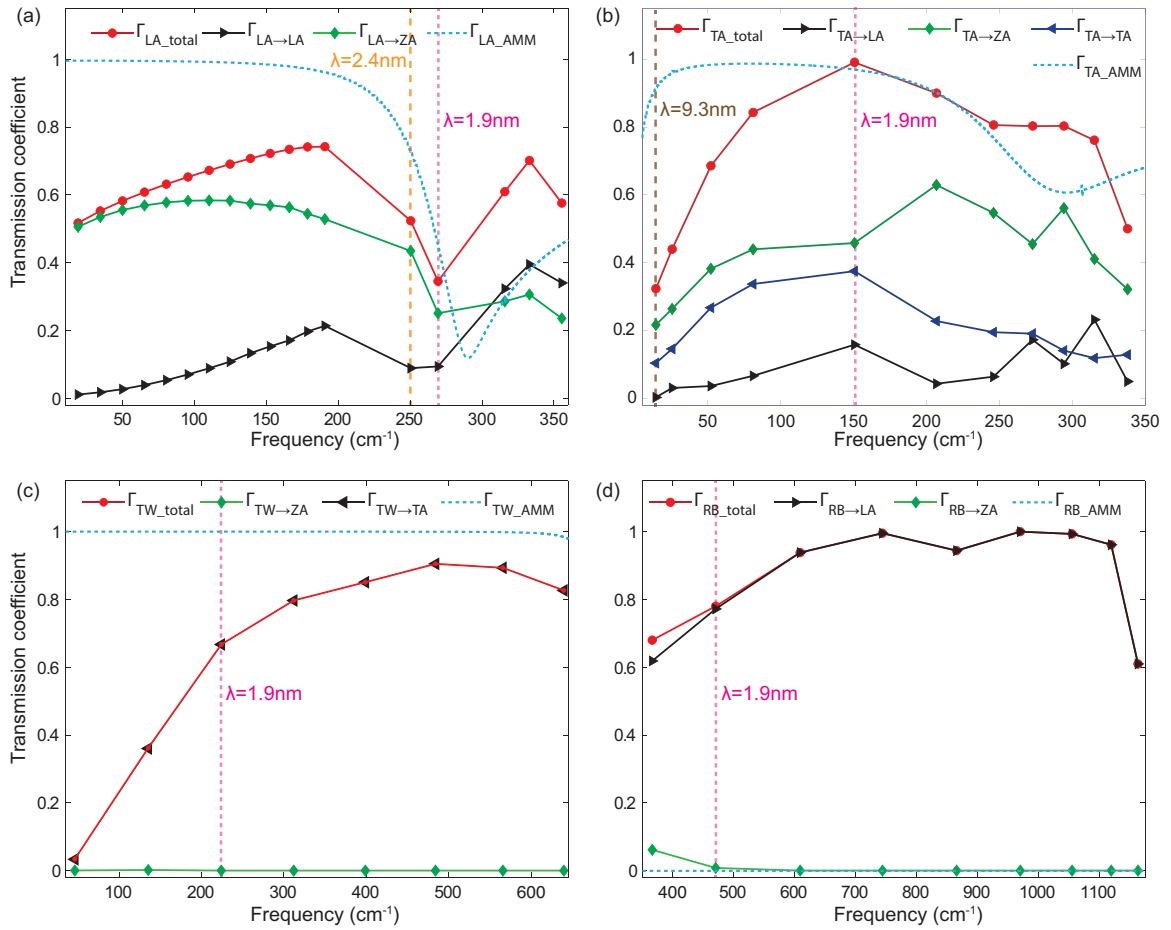


Figure 4.8. Transmission coefficients of incident LA (a), TA (b), TW (c), and RB polarization (d).

into the graphene over the incident energy from CNT in the polarization X. The notation  $\Gamma_{X \rightarrow Y}$  means the breakdown transmission coefficient into a specific graphene polarization Y from incident CNT polarization X. It is found that the polarization conversion is more significant for long incident wavelengths (small wavenumber). Fig. 4.8(a) shows that for long wavelength incident LA polarization, the transmission into the ZA polarization dominates over that into the LA polarization. It can be explained in this way. Long wavelength means the neighboring atoms in CNT vibrate almost in phase. When the motion propagates through the junction, the direction of atomic displacement (mainly along the axial direction in CNT) is largely preserved since the wavelength is much larger than the radius of curvature of the junction (about 0.5 nm). Therefore, most of the transmitted vibration becomes the ZA polarization. As the wavelength decreases, the neighboring atoms start to vibrate out of phase, and the wavelength becomes closer to the junction radius of curvature. Hence, the atomic motion originally along the axial direction in CNT can better adapt to the junction and induce more in plane ( $xy$  plane) motion in graphene. Therefore,  $\Gamma_{LA \rightarrow LA}$  increases with decreasing wavelength. For the incident TA polarization as shown in Fig. 4.8(b), the transmission into the ZA polarization dominates over that into other polarizations like the incident LA wave packet. In the long wavelength range, the polarization conversion is also more important. About 67% of the total transmitted energy is into the ZA polarization when the frequency is about  $14 \text{ cm}^{-1}$  (wavelength  $\lambda$  is around 9.3 nm), and about 46% of the total transmitted energy is into the ZA polarization when the frequency is about  $151 \text{ cm}^{-1}$  (wavelength  $\lambda$  is around 1.9 nm). For the incident TW polarization (in-plane transverse), polarization conversion to ZA (out-of-plane transverse) is more significant at long wavelength as shown in Fig. 4.8(c). For the incident RB polarization (atoms mainly vibrate perpendicularly to energy propagation direction), polarization conversion to LA (atoms mainly vibrate along energy propagation direction) dominates the transmission as shown in Fig. 4.8(d).

Next we compare our simulation results to those from analytical models. Acoustic mismatch and diffuse mismatch models are commonly used for interfacial thermal transport. Here the acoustic mismatch model (AMM) is used since the  $sp^2$  covalent bond is very strong and the interface is smooth. The transmission coefficient from AMM,  $\Gamma_{X\_AMM}$ , is generally higher than the total transmission coefficient  $\Gamma_{X\_total}$  from our wave packet method especially at long wavelengths, as shown in Fig. 4.8. The lower transmission from the wave packet simulation can be attributed to the non-planar interface and defects (six heptagons at the interface as shown in Fig. 4.1). The difference between  $\Gamma_{X\_AMM}$  and  $\Gamma_{X\_total}$  at longer incident wavelength is more significant, because the junction appears to be more abrupt for longer wavelength wave packets, while it is smoother for shorter wavelength packet when the wavelength is comparable or smaller than the junction radius of curvature.

On the other hand, from Fig. 4.8 (a) and (b),  $\Gamma_{X\_total}$  is sometimes higher than  $\Gamma_{X\_AMM}$  at certain short wavelengths (incident wavelength  $\lambda < 1.9$  nm as shown by pink dashed line). In fact, these higher  $\Gamma_{X\_total}$  are related to polarization conversion. AMM assumes that one polarization transmits into the same polarization. However, at the CNT-graphene junction, the existence of polarization conversion provides an additional channel to transfer heat, such that  $\Gamma_{X\_total}$  can be larger than  $\Gamma_{X\_AMM}$ . If we compare  $\Gamma_{LA\_AMM}$  to  $\Gamma_{LA \rightarrow LA}$  alone for the incident LA polarization, we can see that  $\Gamma_{LA\_AMM}$  is indeed generally higher than  $\Gamma_{LA \rightarrow LA}$  especially at long wavelength. The difference between  $\Gamma_{LA\_AMM}$  and  $\Gamma_{LA\_total}$  when  $\lambda < 1.9$  nm is completely from polarization conversion  $\Gamma_{LA \rightarrow ZA}$ . Interestingly, when compared with the transmission coefficient from one polarization to the same one, AMM can still capture some features of transmission.  $\Gamma_{LA \rightarrow LA}$  shows a minimum at around  $250 \text{ cm}^{-1}$  (wavelength  $\lambda=2.4$  nm).  $\Gamma_{LA\_AMM}$  also shows a minimum at around  $290 \text{ cm}^{-1}$ . The minimum from AMM is due to the large mismatch in the group velocity.

To understand how the polarization conversion affects thermal properties, we have applied Landauer formula [60] with the above transmission functions from wave packet

Table 4.1. The CNT-graphene interface thermal conductance results predicted from Landauer approach with transmission functions from wave packet (WP) method (without and with polarization conversion) and AMM of incident LA, TA, TW, and RB branches.

Polarization	$G_{\text{WPw/o}}$ (W/m <sup>2</sup> K)	$G_{\text{WPw/}}$ (W/m <sup>2</sup> K)	$G_{\text{AMM}}$ (W/m <sup>2</sup> K)
LA	$5.02 \times 10^7$	$2.14 \times 10^8$	$2.22 \times 10^8$
TA	$1.36 \times 10^8$	$4.35 \times 10^8$	$6.18 \times 10^8$
TW	$4.64 \times 10^8$	$4.65 \times 10^8$	$1.17 \times 10^{10}$
RB	0	$9.92 \times 10^8$	0

and AMM respectively to calculate thermal conductance at the pillared graphene interface, and compare the results. The Landauer formula is

$$q = \frac{1}{2\pi} \int_0^{+\infty} \hbar\omega [M_1(\omega)\tau_{1\rightarrow 2}(\omega)f(T_1) - M_2(\omega)\tau_{2\rightarrow 1}(\omega)f(T_2)]d\omega, \quad (4.9)$$

where  $M(\omega)$  is the number of modes at a given frequency  $\omega$ ,  $\tau(\omega)$  is the transmission coefficient at the interface from one material to the other, and  $f(T)$  is the Bose-Einstein distribution function at temperature  $T$ . The equivalent equilibrium temperature correction [98] is used since the transmission coefficients are high at CNT-graphene junction. As shown clearly in Table. 4.1, for the incident LA polarization, the polarization conversion adds the conductance from  $5.02 \times 10^7$  W/m<sup>2</sup>K to  $2.14 \times 10^8$  W/m<sup>2</sup>K. The contribution of polarization conversion is 76.5% of the total conductance. For the incident TA polarization as shown in Table. 4.1, the contribution of polarization conversion, which is 68.7% of the total also dominates. Interestingly, for the incident RB polarization, since there is no corresponding polarization in graphene, the conductance without polarization conversion is 0, and the contribution of polarization conversion is 100%. When compared with conductance results from AMM transmission coefficients,  $G_{\text{LA\_WP}}$  is comparable to  $G_{\text{LA\_AMM}}$  because  $\Gamma_{\text{LA\_total}}$  is generally smaller than  $\Gamma_{\text{LA\_AMM}}$ , but larger than  $\Gamma_{\text{LA\_AMM}}$  at high frequency. For TA and TW branches,  $G_{\text{WP}}$  is smaller than  $G_{\text{AMM}}$  since the transmission  $\Gamma_{\text{total}}$  is generally smaller than  $\Gamma_{\text{AMM}}$ . For RB branch, as we mentioned above, since there is no corresponding polarization in graphene,  $G_{\text{RB\_AMM}}$  is 0, and  $G_{\text{RB\_WP}}$  is much larger than it. From the interface thermal conductance calculation, it shows that polarization conversion dominates most incident phonon polarizations, and the interface conductance with transmission from wave packet  $G_{\text{WP}}$  can be smaller than  $G_{\text{AMM}}$  when the transmission is smaller, and can also exceed  $G_{\text{AMM}}$  because the former includes while the latter neglects polarization conversion. Therefore, the unique junction between 1D CNT and 2D graphene on one hand tends to reduce the transmission and interface conductance due to the defects and dimensional mismatch, while on the other hand tends to enhance the transmission and conductance due to polarization conversion. The overall effect depends on which mechanism dominates.

#### 4.4 Summary

To summarize, we have predicted the transmission function of individual phonon mode using the wave packet method at CNT-graphene junction, which is a dimensionally mismatched interface between 1D and 2D materials. Intriguing phonon polarization conversion behavior is observed for most incident phonon modes. It is found that the polarization conversion dominates the transmission and is more significant at larger phonon wavelength. We attribute such unique phonon polarization conversion behavior to the dimensional mismatch across CNT-graphene interface. The transmission coefficients of our wave packet method and AMM are compared with each other. It is found that the transmission functions at the junction cannot be predicted by the conventional acoustic mismatch models due to the existence of dimensional mismatch. Then we used Landauer formula with transmission functions from both wave packet method and AMM to predict the interface conductance. For the incident LA polarization, the results of two methods are similar, while for RB, the conductance from wave packet method is much larger, and for TA and TW, AMM predict larger conductance. The dimensionally mismatched interface, on one hand tends to reduce the transmission and conductance due to defects and the change of phonon propagation direction at the interface, while on the other hand tends to enhance the transmission and conductance due to the new phonon transport channel introduced by polarization conversion.

## 5. NONEQUILIBRIUM LANDAUER APPROACH FOR THERMAL INTERFACES

### 5.1 Introduction

As modern electronic devices shrink in size and increase in the use of heterostructures [99], heat dissipation becomes one of the biggest problems that limit their performance and reliability. Thermal resistances from interfaces were previously reported to be comparable to or dominant over those of the materials. For example, the thermal boundary resistance (TBR) at the CNT-graphene junction is comparable to the resistance of a 200 nm long pure CNT [24, 25]. Hence, understanding thermal interfacial transport and designing interfaces with high thermal conductance are urgent problems to study. The Landauer approach [60, 63, 100–106] has been widely used to predict the thermal boundary conductance  $G$ :

$$G = \frac{\sum_p \int_0^{+\infty} \frac{1}{4} D v_g \tau \hbar \omega (f(T_{e,1}) - f(T_{e,2})) d\omega}{T_{e,1} - T_{e,2}} = \sum_p \int_0^{+\infty} \frac{1}{4} D v_g \tau \hbar \omega \frac{df(T)}{dT} d\omega, \quad (5.1)$$

here the  $p$  – *sum* is over all the incident phonon branches,  $\hbar$  is the reduced Planck constant,  $\omega$  is the phonon frequency,  $D$  is the phonon density of states,  $v_g$  is the modal phonon group velocity,  $\tau$  is the modal transmission coefficient at the interface from one material to the other,  $f(T)$  is the carrier statistics at a certain temperature  $T$ , and  $T_{e,1}$  and  $T_{e,2}$  are the emitted phonon temperatures from two reservoirs.

However, experimental and molecular dynamics simulation results [61–63] often exceed the TBC predicted from the Landauer formula Eq.5.1 and even the radiation limit (when the transmission coefficients are set as 1 in Eq.5.1) [48, 107], which is usually considered as the upper limit of the thermal boundary conductance (TBC). Two possible mechanisms have been proposed, including inelastic scattering at the interface [64, 65] and cross-interface electron-phonon coupling [66–70]. However, be-

fore involving these mechanisms, we can examine whether Eq. 5.1 itself is a sound representation of the elastic conductance. In fact, Eq. 5.1 is clearly based on an important assumption that an interface is a local thermal equilibrium system, where the measurable temperatures of all phonon modes are the emitted phonon temperature  $T_e$ . Such an assumption may be reasonable for electron and photon interfacial transport, for which the Landauer approach was originally developed, since the temperature reservoirs can be held right adjacent to the interface or surface. However, it is questionable for phonons, since in standard measurements of interfacial thermal conductance such as the two-bar method [71], the reservoirs are placed far away from the interface, so as in molecular dynamics simulations of interfacial thermal transport [55]. It was pointed out in previous work of Zeng and Chen [98] that on the left side of the interface (as shown in Fig. 5.1(a)) there are three groups of phonons: incident phonons traveling toward the interface with  $T_{e,1}$ , reflected phonons with  $T_{e,1}$ , and transmitted phonons from the right-side with  $T_{e,2}$ . Clearly the incident, reflected, and transmitted phonons are not in equilibrium, and the measurable temperature near the interface should be affected by the transmitted phonons and different from the emitted phonon temperature  $T_e$ . A local equivalent equilibrium temperature was defined in Zeng and Chen's work [98], and it correctly predicts a zero resistance for an imaginary interface in a pure material rather than a finite resistance that would be predicted by Eq.5.1. However, the model was a gray approach so it did not consider different phonon modes and the consequences of their varied transmission coefficients. Recently, a modal non-equilibrium molecular dynamics approach has been developed and the results show that different phonon modes are in strong nonequilibrium near an interface. Such nonequilibrium effect needs to be incorporated in the Landauer approach.

In this work, we first apply the conventional Landauer approach Eq.5.1 to the CNT-graphene interface which is a matched interface. A comparison to the results from nonequilibrium molecular dynamics (NEMD) method shows that the conventional Landauer formula underestimates the TBC. To verify our observation, a

Si/heavy-Si system is studied with both Landauer formula and NEMD method, and it is found that with increased similarity between the two materials, the underestimation from the conventional Landauer approach increases. The underestimation is identified to come from the assumption that all phonon modes are at the emitted temperatures  $T_e$ . To modify the Landauer approach, we use the modal equivalent equilibrium temperature to calculate the modal conductance and show the local thermal nonequilibrium; we then define the overall equivalent lattice temperature to calculate the total thermal conductance. Our "nonequilibrium Landauer approach" is applied for the Si/heavy-Si interface, CNT-graphene junction, and ZnO/GaN interface, and the results agree much better with the NEMD method and experimental results [63]. A chart is also created to quickly estimate the correction of the interfacial conductance as a function of the mass ratio, and it will help determine whether our approach is needed for a given interface.

## 5.2 Failure of the conventional Landauer approach on the CNT-graphene Junction

We first use the conventional Landauer approach for the CNT-graphene junction. The TBC  $G$  is

$$G = \frac{q}{A_c \Delta T} = \frac{q}{A_c (T_{e,1} - T_{e,2})}, \quad (5.2)$$

where  $q$  is the net heat flow rate,  $A_c$  is the cross-sectional area of a CNT-graphene interface, and  $T_{e,1}$  and  $T_{e,2}$  are the emitted phonon temperatures. The net heat flow rate as shown in Fig. 5.1 usually takes the following form [60, 63, 100, 102],

$$q = \sum_p \int_0^{+\infty} \frac{1}{2\pi} M(\omega) \tau(\omega) \hbar \omega [f(T_{e,1}) - f(T_{e,2})] d\omega, \quad (5.3)$$

where  $M(\omega)$  is the number of modes of CNT at a given frequency  $\omega$ . The phonon properties are calculated from lattice dynamics with AIREBO potential. It should be noted that only the phonon properties of CNT is needed here because of the constraint from detailed balance, that the net heat flow rate is 0 when  $T_{e,1} = T_{e,2}$ ,

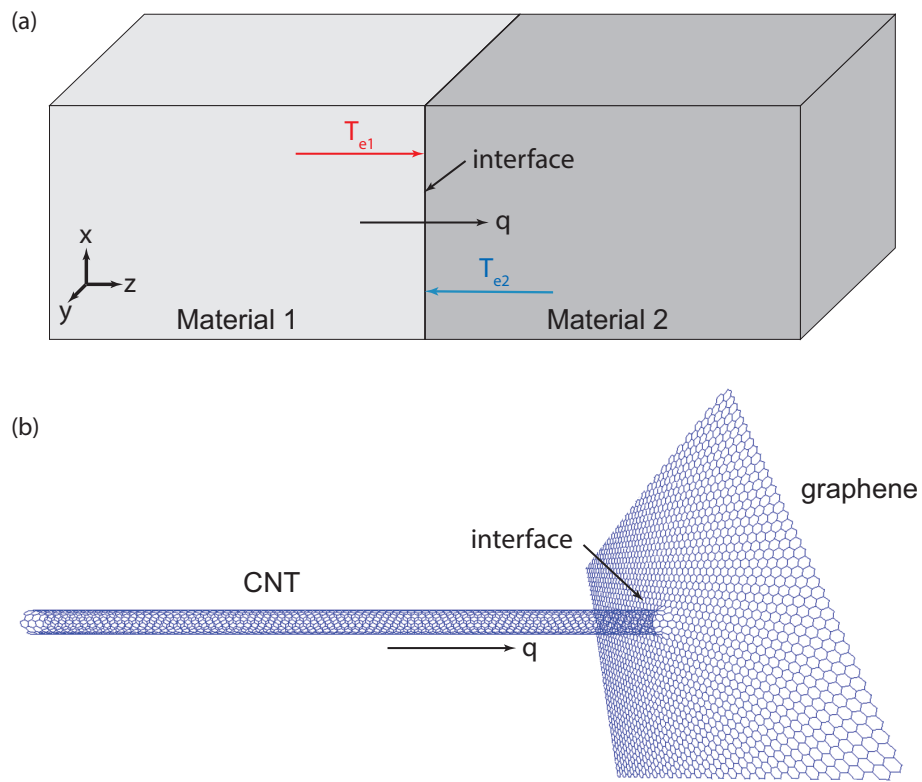


Figure 5.1. (a) The general structure of thermal transport considered in Landauer approach. (b) The CNT-graphene structure with a dimensionally mismatched 1D-2D interface.

and the graphene information is included in the transmission coefficients. The related proof is shown below:

At the CNT-graphene junction between a 1D CNT and two dimensional (2D) graphene as shown in Fig. 5.1(b), the expression of net heat flow rate across the dimensionally mismatched interface is:

$$q = \sum_p \int_0^{+\infty} \frac{1}{2\pi} \hbar\omega [M_{CNT}(\omega)\tau_{1\rightarrow 2}(\omega)f(T_{e,1}) - M_{graphene}(\omega)\tau_{2\rightarrow 1}(\omega)f(T_{e,2})]d\omega. \quad (5.4)$$

For the 1D CNT, the number of modes is:

$$M_{CNT} = 1. \quad (5.5)$$

For the 2D graphene, the number of modes is:

$$M_{graphene} = width \cdot \frac{k(\omega)}{\pi}. \quad (5.6)$$

At the CNT-graphene interface, the detailed balance always needs to be satisfied as mentioned above. The detailed balance at the interface gives that:

$$M_{CNT}(\omega)\tau_{1\rightarrow 2}(\omega) = M_{graphene}(\omega)\tau_{2\rightarrow 1}(\omega). \quad (5.7)$$

As a result, the Landauer formula equation 5.4 of  $q$  from 1D CNT to 2D graphene is simplified as:

$$q = \sum_p \int_0^{+\infty} \frac{1}{2\pi} \hbar\omega M_{CNT}(\omega)\tau_{1\rightarrow 2}(\omega)[f(T_{e,1}) - f(T_{e,2})]d\omega. \quad (5.8)$$

It should be noted that the equation 5.3 is for interfaces with incident angle-independent transmission coefficients or at least one of material 1 and 2 is one dimensional (1D). In our system, the CNT is 1D and as a result the equation 5.3 can be applied to our CNT-graphene interface as shown in Fig. 5.1(b).

We have applied both acoustic mismatch (AMM) and diffuse mismatch (DMM) models to calculate the frequency dependent transmission coefficients. The proof of that the detailed balance holds with AMM can be found below:

The heat flux across the interface from medium 1 to medium 2 due to phonons leaving medium 1 with different dimensions are:

$$J_{1,1D} = \sum_p \int_0^{+\infty} \frac{1}{2} D_{1,1D}(\omega) f(T_{e1}) \hbar \omega v_{g1}(\omega) \tau_{1 \rightarrow 2}(\omega) d\omega, \quad (5.9)$$

$$J_{1,2D} = \sum_p \int_0^{+\infty} \int_{-\frac{\pi}{2}}^{+\frac{\pi}{2}} \frac{1}{2\pi} D_{1,2D}(\omega) f(T_{e1}) \hbar \omega v_{g1}(\omega) \tau_{1 \rightarrow 2}(\theta, \omega) \cos \theta d\theta d\omega, \quad (5.10)$$

$$\begin{aligned} J_{1,3D} &= \sum_p \int_0^{+\infty} \int_0^{2\pi} \int_0^{\frac{\pi}{2}} \frac{1}{4\pi} D_{1,3D}(\omega) f(T_{e1}) \hbar \omega v_{g1}(\omega) \tau_{1 \rightarrow 2}(\theta, \omega) \cos \theta \sin \theta d\theta d\varphi d\omega \\ &= \sum_p \int_0^{+\infty} \int_0^{\frac{\pi}{2}} \frac{1}{2} D_{1,3D}(\omega) f(T_{e1}) \hbar \omega v_{g1}(\omega) \tau_{1 \rightarrow 2}(\theta, \omega) \cos \theta \sin \theta d\theta d\omega, \end{aligned} \quad (5.11)$$

where the  $p$ -sum is over all the incident phonon branches,  $D_1(\omega)$  and  $v_{g1}(\omega)$  are the phonon density of states per unit volume and group velocity at a given frequency  $\omega$  of the corresponding branch in medium 1,  $f(T_{e1})$  is the carrier statistics at emitted temperature  $T_{e1}$ ,  $\hbar$  is the reduced Planck constant, and  $\tau_{1 \rightarrow 2}$  is the transmission coefficient at the interface from medium 1 to medium 2. For 2D and 3D materials, the polar angle  $\theta$  is the incident angle between the wave vector of the incident phonon and the normal to the interface. For 3D materials,  $\varphi$  is the azimuthal angle, and the  $\sin \theta d\theta d\varphi$  is the solid angle. The  $\frac{1}{2}$  in the  $J_{1,1D}$  is because that phonons will propagate either forward or backward, the  $\frac{1}{2\pi}$  in the  $J_{1,2D}$  is because that the integration of plane angle is  $2\pi$  over the circle, and the  $\frac{1}{4\pi}$  in the  $J_{1,3D}$  is because that the integration of solid angle is  $4\pi$  over the sphere. It should be noted that these equations include the isotropic assumption that the phonon group velocity and number of phonons emitted from one point are not direction dependent.

For materials with different dimensions, the phonon density of states per unit volume are different as shown below:

$$D_{1D} = \frac{1}{v_g(\omega)\pi}, \quad (5.12)$$

$$D_{2D} = \frac{k(\omega)}{2\pi v_g(\omega)}, \quad (5.13)$$

$$D_{3D} = \frac{k(\omega)^2}{2\pi^2 v_g(\omega)}, \quad (5.14)$$

where  $k(\omega)$  is the wave vector at a given frequency  $\omega$  of the corresponding phonon branch.

If we insert the phonon density of states into the heat flux, the equations will be:

$$J_{1,1D} = \sum_p \int_0^{+\infty} \frac{1}{2\pi} f(T_{e1}) \hbar \omega \tau_{1 \rightarrow 2}(\omega) d\omega, \quad (5.15)$$

$$J_{1,2D} = \sum_p \int_0^{+\infty} \int_{-\frac{\pi}{2}}^{+\frac{\pi}{2}} \frac{1}{4\pi^2} k(\omega) f(T_{e1}) \hbar \omega \tau_{1 \rightarrow 2}(\theta, \omega) \cos \theta d\theta d\omega, \quad (5.16)$$

$$J_{1,3D} = \sum_p \int_0^{+\infty} \int_0^{\frac{\pi}{2}} \frac{1}{4\pi^2} k(\omega)^2 f(T_{e1}) \hbar \omega \tau_{1 \rightarrow 2}(\theta, \omega) \cos \theta \sin \theta d\theta d\omega. \quad (5.17)$$

If the transmission coefficient  $\tau_{1 \rightarrow 2}$  does not depend on incident angle,  $J_{1,1D}$  will not change, and the heat flux expressions of 2D and 3D materials will be:

$$J_{1,2D} = \sum_p \int_0^{+\infty} \frac{1}{2\pi^2} k(\omega) f(T_{e1}) \hbar \omega \tau_{1 \rightarrow 2}(\omega) d\omega, \quad (5.18)$$

$$J_{1,3D} = \sum_p \int_0^{+\infty} \frac{1}{8\pi^2} k(\omega)^2 f(T_{e1}) \hbar \omega \tau_{1 \rightarrow 2}(\omega) d\omega. \quad (5.19)$$

Adapting an idea from the calculation of electrical current, the phonon number of modes, which can be considered as the number of carrier half-wavelengths that fit into the interface, is defined as:

$$M_{1D} = 1, \quad (5.20)$$

$$M_{2D} = \frac{k(\omega)}{\pi}, \quad (5.21)$$

$$M_{3D} = \frac{k(\omega)^2}{4\pi}. \quad (5.22)$$

Then the heat flux leaving medium 1 with transmission independent of incident angle of 1D, 2D, and 3D will have the same general form:

$$J_1 = \sum_p \int_0^{+\infty} \frac{1}{2\pi} \hbar\omega M_1(\omega) f(T_{e1}) \tau_{1 \rightarrow 2}(\omega) d\omega, \quad (5.23)$$

and this expression can be used for any 1D material, or 2D and 3D materials with angle-independent transmission coefficient.

With the expressions of heat flux  $J_1$  and  $J_2$  leaving medium 1 and 2, the net heat flow rate across the interface from medium 1 to 2 is:

$$q = A_c \cdot (J_1 - J_2), \quad (5.24)$$

where  $A_c$  is the cross-sectional area of the interface.

The principle of detailed balance requires that the net heat flow rate across the interface  $q$  should be 0 when the temperatures of two mediums are the same. Taking the interface between 3D materials as an example, from equation 5.11 the net heat flow rate  $q_{3D}$  is:

$$q_{3D} = \sum_p \frac{A_c}{2} \int_0^{+\infty} \int_0^{\frac{\pi}{2}} D_1(\omega) f(T_{e1}) \hbar\omega v_{g1}(\omega) \tau_{12}(\theta, \omega) \cos \theta \sin \theta d\theta d\omega - \sum_p \frac{A_c}{2} \int_0^{\frac{\pi}{2}} \int_0^{+\infty} D_2(\omega) f(T_{e2}) \hbar\omega v_{g2}(\omega) \tau_{21}(\theta, \omega) \cos \theta \sin \theta d\theta d\omega.$$

Acoustic mismatch (AMM) and diffuse mismatch (DMM) models are usually used for the frequency dependent transmission coefficients calculation. The transmission function for interface between 3D materials from AMM is both incident angle and frequency dependent as shown in the following equation:

$$\tau_{12,AMM}(\theta_1, \omega) = \tau_{21,AMM}(\theta_2, \omega) = \frac{4 \frac{Z_2 \cos \theta_2}{Z_1 \cos \theta_1}}{\left(\frac{Z_2}{Z_1} + \frac{\cos \theta_2}{\cos \theta_1}\right)^2}. \quad (5.25)$$

Considering the phonons in medium 1 with incident polar angle from  $\theta_1$  to  $\theta_1 + d\theta_1$ , some of the phonons will be reflected at the interface and some will be refracted into the medium at an angle of refraction between  $\theta_2$  to  $\theta_2 + d\theta_2$ . Because of the Snell's law of acoustic refraction, we have:

$$d\theta_2 = \frac{v_{g2}(\omega) \cos \theta_1}{v_{g1}(\omega) \cos \theta_2} d\theta_1, \quad (5.26)$$

and

$$\sin \theta_2 = \frac{v_{g2}(\omega)}{v_{g1}(\omega)} \sin \theta_1. \quad (5.27)$$

Then

$$\begin{aligned} D_1(\omega) v_{g1}(\omega) \tau_{12}(\theta_1, \omega) \cos \theta_1 \sin \theta_1 d\theta_1 &= \frac{k_1(\omega)^2}{2\pi^2 v_{g1}(\omega)} v_{g1}(\omega) \tau_{12}(\theta_1, \omega) \cos \theta_1 \sin \theta_1 d\theta_1 \\ &= \frac{k_1(\omega)^2}{2\pi^2} \tau_{12}(\theta_1, \omega) \cos \theta_1 \sin \theta_1 d\theta_1, \end{aligned} \quad (5.28)$$

and

$$\begin{aligned} D_2(\omega) v_{g2}(\omega) \tau_{21}(\theta_2, \omega) \cos \theta_2 \sin \theta_2 d\theta_2 &= \frac{k_2(\omega)^2}{2\pi^2 v_g(\omega)} v_{g1}(\omega) \tau_{21}(\theta_2, \omega) \cos \theta_2 \sin \theta_2 d\theta_2 \\ &= \frac{k_2(\omega)^2}{2\pi^2} \tau_{12}(\theta_1, \omega) \cos \theta_2 \sin \theta_2 \frac{v_{g2}(\omega) \cos \theta_1}{v_{g1}(\omega) \cos \theta_2} d\theta_1 \\ &= \frac{k_2(\omega)^2}{2\pi^2} \tau_{12}(\theta_1, \omega) \cos \theta_1 \sin \theta_2 \frac{\sin \theta_2}{\sin \theta_1} d\theta_1 \\ &= \frac{k_2(\omega)^2}{2\pi^2} \tau_{12}(\theta_1, \omega) \cos \theta_1 \sin \theta_1 \left( \frac{\sin \theta_2}{\sin \theta_1} \right)^2 d\theta_1. \end{aligned} \quad (5.29)$$

The relation between wavenumber and frequency of medium 2 can be further expressed in the following form, since the acoustic mismatch model is from the Snell's law of light, whose velocity does not change with frequency,

$$\frac{k_2(\omega)}{\omega} = \frac{1}{v_{g2}(\omega)} = \frac{k_1(\omega) v_{g1}(\omega)}{\omega v_{g2}(\omega)} = \frac{k_1(\omega) \sin \theta_1}{\omega \sin \theta_2}. \quad (5.30)$$

Hence, we have

$$\begin{aligned} D_2(\omega) v_{g2}(\omega) \tau_{21}(\theta_2, \omega) \cos \theta_2 \sin \theta_2 d\theta_2 &= \frac{k_2(\omega)^2}{2\pi^2} \tau_{12}(\theta_1, \omega) \cos \theta_1 \sin \theta_1 \left( \frac{\sin \theta_2}{\sin \theta_1} \right)^2 d\theta_1 \\ &= \frac{k_1(\omega)^2}{2\pi^2} \left( \frac{\sin \theta_1}{\sin \theta_2} \right)^2 \tau_{12}(\theta_1, \omega) \cos \theta_1 \sin \theta_1 \left( \frac{\sin \theta_2}{\sin \theta_1} \right)^2 d\theta_1 \\ &= \frac{k_1(\omega)^2}{2\pi^2} \tau_{12}(\theta_1, \omega) \cos \theta_1 \sin \theta_1 d\theta_1 \\ &= D_1(\omega) v_{g1}(\omega) \tau_{12}(\theta_1, \omega) \cos \theta_1 \sin \theta_1 d\theta_1, \end{aligned} \quad (5.31)$$

and as a result, the detailed balance with  $T_{e1} = T_{e2}$  is fulfilled as:

$$\begin{aligned} q_{3D} &= \sum_p \frac{A_c}{2} \int_0^{+\infty} \int_0^{\frac{\pi}{2}} D_1(\omega) f(T_{e1}) \hbar \omega v_{g1}(\omega) \tau_{12}(\theta, \omega) \cos \theta \sin \theta d\theta d\omega - \\ &\quad \sum_p \frac{A_c}{2} \int_0^{+\infty} \int_0^{\frac{\pi}{2}} D_2(\omega) f(T_{e1}) \hbar \omega v_{g2}(\omega) \tau_{21}(\theta, \omega) \cos \theta \sin \theta d\theta d\omega \\ &= \sum_p \frac{A_c}{2} \int_0^{+\infty} \int_0^{\frac{\pi}{2}} D_1(\omega) f(T_{e1}) \hbar \omega v_{g1}(\omega) \tau_{12}(\theta, \omega) \cos \theta \sin \theta d\theta d\omega - \\ &\quad \sum_p \frac{A_c}{2} \int_0^{+\infty} \int_0^{\frac{\pi}{2}} D_1(\omega) f(T_{e1}) \hbar \omega v_{g1}(\omega) \tau_{12}(\theta, \omega) \cos \theta \sin \theta d\theta d\omega \\ &= 0. \end{aligned} \quad (5.32)$$

For the AMM model [48, 60], the transmission coefficient at 1D-2D interface is defined as:

$$\tau_{1 \rightarrow 2}(\omega) = \tau_{2 \rightarrow 1}(\omega) = \frac{4Z_1(\omega)Z_2(\omega)}{(Z_1(\omega) + Z_2(\omega))^2}, \quad (5.33)$$

where  $Z$  is the acoustic impedance which equals to the product of the material mass density  $\rho$  and the phonon group velocity  $v_g$ . The phonon group velocity is given by the slope of phonon dispersion relations. The transmission function of AMM is from a single mode of material 1 (CNT here) to a single mode of material 2 (graphene

here). There are 72 and 6 branches in the phonon dispersion relation of (6,6) CNT and graphene, respectively, because the number of atoms in the primitive cells of (6,6) CNT and graphene are 24 and 2. Hence, there will be polarization conversion during the transmission process. From the previous study of phonon transmission coefficients at CNT-graphene junction with phonon wave-packet method [108], we assume that a low frequency mode of CNT with largest radial component will become a LA mode of graphene, a low frequency mode of CNT with largest axial component will become a ZA mode of graphene, a low frequency mode of CNT with largest tangential component will become a TA mode of graphene, a high frequency mode of CNT with largest radial component will become a LO mode of graphene, a high frequency mode of CNT with largest axial component will become a ZO mode of graphene, and a high frequency mode of CNT with largest tangential component will become a TO mode of graphene. The radial, axial, tangential components are calculated from the phonon eigenvector of the corresponding mode of CNT.

The transmission coefficients from all 72 branches of different frequency are shown in Fig. 5.2 with the important longitudinal acoustic (LA), transverse acoustic (TA), and the twisting (TW) branches highlighted.

For the DMM model [48, 60], the transmission coefficient is defined as:

$$\tau_{1 \rightarrow 2}(\omega) = 1 - \tau_{2 \rightarrow 1}(\omega) = \frac{\sum_p M_2}{\sum_p M_1 + \sum_p M_2}. \quad (5.34)$$

The detailed balance of Landauer formula with transmission function from DMM is automatically satisfied because of the definition. The transmission coefficients from DMM of different frequency are shown as a green curve in Fig. 5.2. Because all the incident modes lose their memory during transmission process, the transmission coefficients of DMM only depend on frequency but not polarization unlike AMM. It should be noted that both AMM and DMM assume elastic transmission process without the change of phonon frequency.

After the heat flow rate  $q$  is calculated, the thermal boundary conductance  $G$  at the CNT-graphene junction can be calculated as shown in Eq. 5.2. The cross-sectional

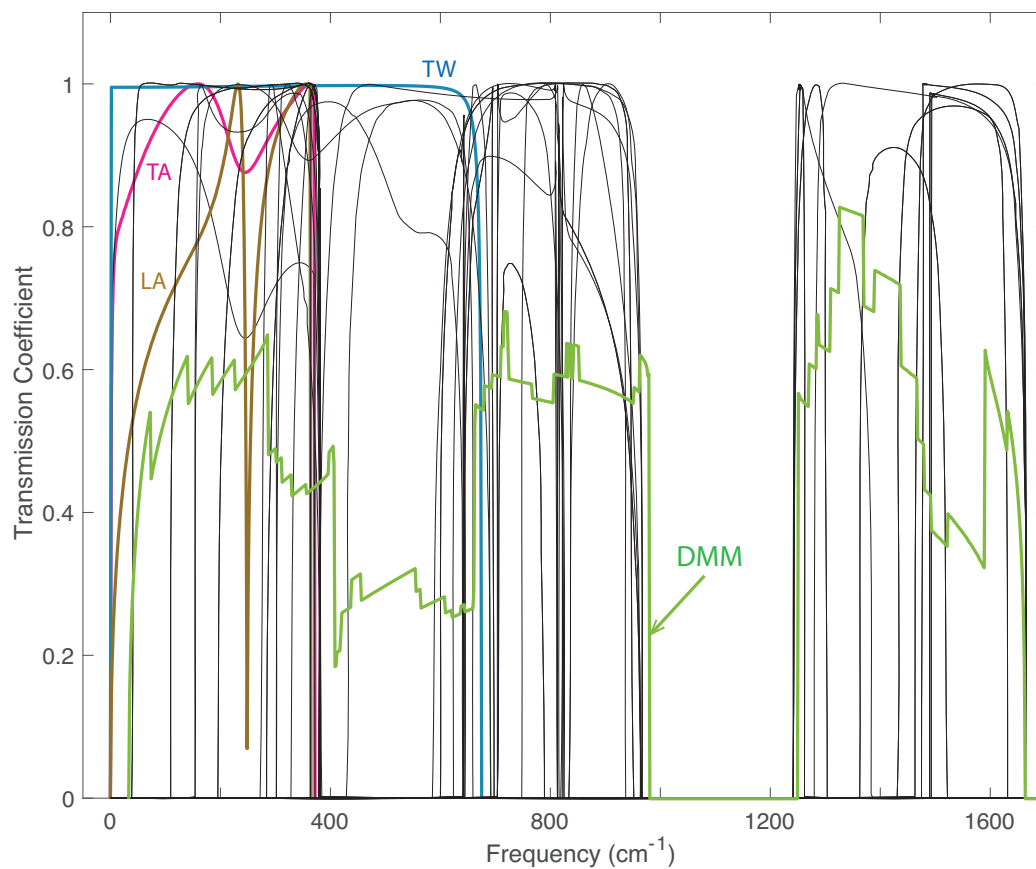


Figure 5.2. The transmission coefficients as a function of phonon frequency of different branches from CNT to graphene from acoustic and diffuse mismatch models. The AMM transmission curves of acoustic branches have been highlighted. The green curve is the DMM transmission coefficient.

area  $A_c$  equals to  $8.57 \times 10^{-19} \text{ m}^2$ , approximated as a circular ring of thickness 0.335 nm and radius 4.07 nm (average of inner and outer radius) which equals to the radius of the (6,6) CNT.

Compared to the TBC result from the previous molecular dynamics (MD) study [24, 25], which is  $1.3 \times 10^{10} \text{ W/m}^2\text{K}$ , the conductance from Landauer formula with AMM is  $2.5 \times 10^9 \text{ W/m}^2\text{K}$ , while the that with DMM is  $1.6 \times 10^9 \text{ W/m}^2\text{K}$ . The smaller conductance from DMM is due to the assumption of a rough and diffuse interface. Under such assumption, even at an imaginary interface in a pure material the transmission coefficient is 0.5 and half of the incident phonons will be reflected. Since the junction is relatively smooth, it is expected that AMM would give a better prediction. However, even the conductance with AMM is much smaller than that from MD. The underestimated  $G$  from the Landauer approach can come from either an underestimation of  $q$  or an overestimation of  $\Delta T$ . In fact, with the highest possible heat flow rate  $q$ , that the transmission coefficient being set to 1 assuming all phonons can transmit without reflection, the TBC  $G$ , which is the theoretical upper limit called the "radiation limit", equals to  $3.7 \times 10^9 \text{ W/m}^2\text{K}$ , and is still much lower than the TBC from MD. Hence, the underestimation from Landauer should mainly come from the overestimation of  $\Delta T$ .

CNT-graphene junction is a matched interface because the CNT is like rolled-up graphene, and the transmission coefficients are quite high as shown in Fig. 5.2. The transmitted phonons will affect the local temperature near the interface, such that the measurable temperature is no longer the same as the emitted temperature  $T_e$ . We suspect that with the increasing similarity between two materials across the interface, the effect will be stronger. Hence next we study a conceptual Si/heavy-Si system where we can systematically vary the mass ratio.

### 5.3 Si/heavy-Si interface

We use both the Landauer approach and non-equilibrium molecular dynamics (NEMD) to calculate the TBC at Si/heavy-Si interfaces. The silicon mass  $M_1$  on the left side is the real mass 28.085, while  $M_2$  of the right side is varied between  $(1-3) \times 28.085$ , in order to tune the similarity between the two materials. The Tersoff potential is applied in both Landauer and NEMD calculation to minimize the difference from interatomic potentials.

Since the interface of Si/heavy-Si is between 3D materials, the incident angles need to be considered. The heat flow rate from the Landauer approach is now [60]:

$$q_{3D} = \frac{A_c}{2} \int_0^{\frac{\pi}{2}} \int_0^{+\infty} \hbar\omega [D_1(\omega)v_{g1}(\omega)\tau_{12}(\theta_1, \omega)f(T_{e,1}) \sin\theta \cos\theta] d\omega d\theta - \frac{A_c}{2} \int_0^{\frac{\pi}{2}} \int_0^{+\infty} \hbar\omega [D_2(\omega)v_{g2}(\omega)\tau_{21}(\theta_2, \omega)f(T_{e,2}) \sin\theta \cos\theta] d\omega d\theta. \quad (5.35)$$

Because the conductance prediction from DMM is lower than that from AMM at interface between similar materials, here we will only apply the Landauer approach with transmission from AMM. At the 3D-3D interface, there will also be some adjustment to the transmission coefficient from AMM because of the oblique incidence. The transmission function is now:

$$\tau_{12,AMM}(\theta_1, \omega) = \tau_{21,AMM}(\theta_2, \omega) = \frac{4 \frac{Z_2 \cos\theta_2}{Z_1 \cos\theta_1}}{\left(\frac{Z_2}{Z_1} + \frac{\cos\theta_2}{\cos\theta_1}\right)^2}. \quad (5.36)$$

With the constraint of detailed balance,  $q$  can be simplified as:

$$q_{3D} = \frac{A_c}{2} \int_0^{\frac{\pi}{2}} \int_0^{+\infty} \hbar\omega [D_1(\omega)v_{g1}(\omega)\tau_{12}(\theta_1, \omega)(f(T_{e,1}) - f(T_{e,2})) \sin\theta \cos\theta] d\omega d\theta. \quad (5.37)$$

During the calculation of transmission coefficient, the isotropic assumption is made and only the information from phonon dispersion relation of silicon [100] direction is included because it is found that the contribution in different directions are nearly the same from atomistic Green's function (AGF) method [109] as shown in Fig. 5.3.

Now the TBC  $G$  across the Si/heavy-Si interface can be calculated together with the temperature jump at the interface  $\Delta T = T_{e,1} - T_{e,2}$  from Eq. 5.2.

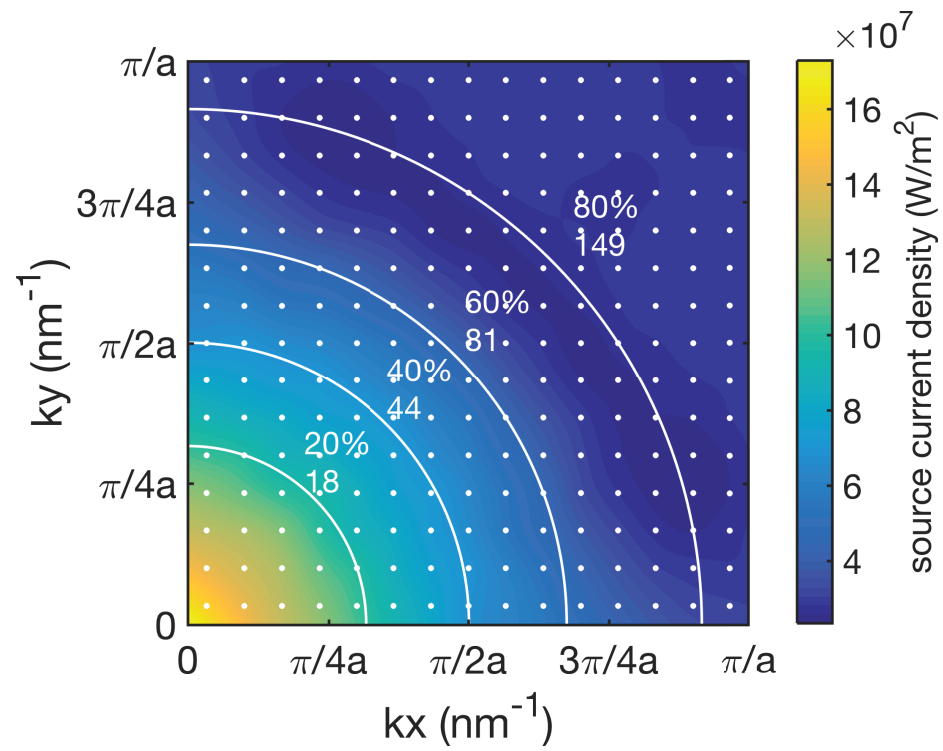


Figure 5.3. The directional thermal conductance contribution from NEGF at Si/heavy-Si interface.

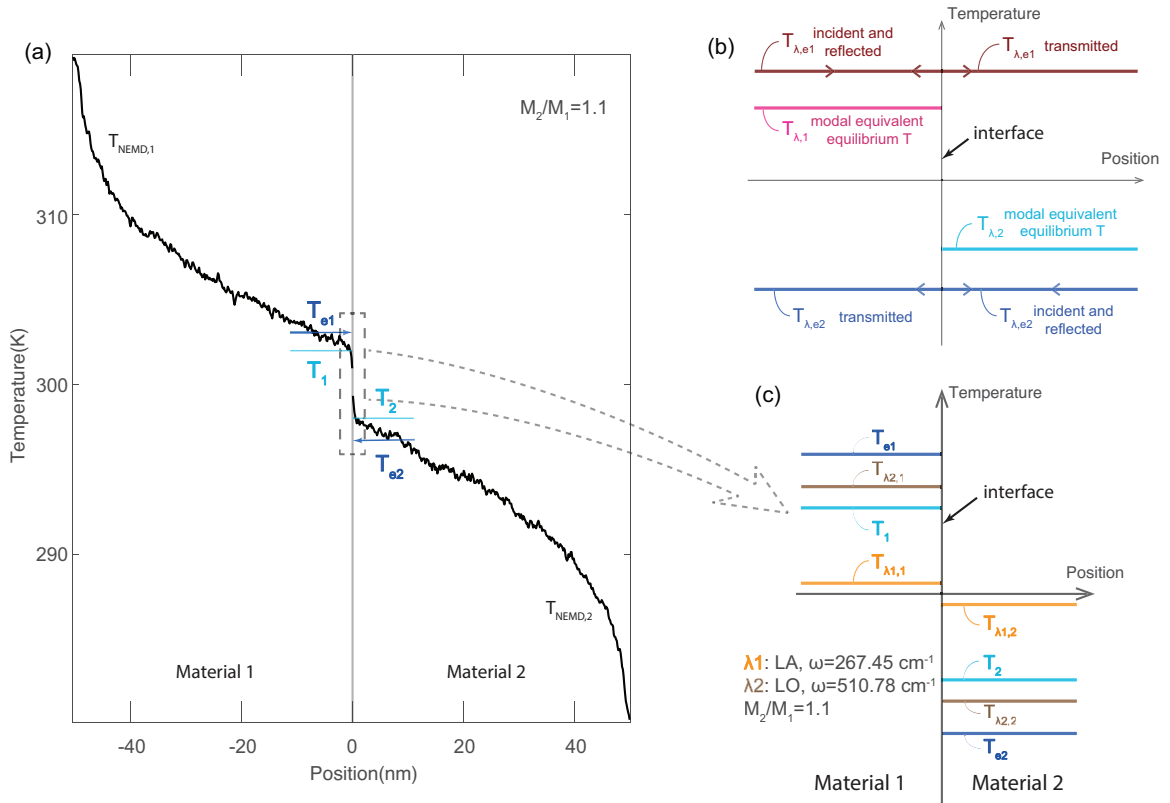


Figure 5.4. (a) The temperature profile from NEMD compared to  $T_\lambda$  from Landauer approach at Si/heavy-Si interface.  $\lambda$  is the phonon mode. The emitted temperatures  $T_{e,1}$  and  $T_{e,2}$  are carefully selected to make equivalent equilibrium temperatures  $T_1$  and  $T_2$  match the temperature jump at the interface from NEMD simulations. (b) The schematic of emitted temperature  $T_e$  and modal equivalent equilibrium temperature  $T_\lambda$ . (c) The details of temperatures near the interface at Si/heavy-Si interface.

To compare the TBC results from Landauer formula with the NEMD results, the NEMD simulations have been performed on Si/heavy-Si system with the LAMMPS package. The temperature profile of Si/heavy-Si from NEMD is shown in Fig. 5.4(a). The temperature jump  $\Delta T$  from NEMD is the difference between the extrapolation at the interface of the linear temperature fit in material 1 and 2, and  $\Delta T = T_1 - T_2$  as shown in Fig. 5.4(a).

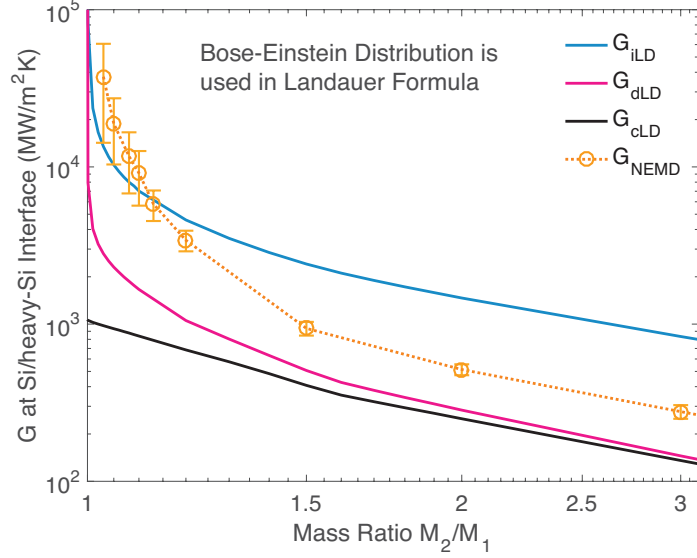


Figure 5.5. The intrinsic thermal boundary conductance  $G_{iLD}$ , dressed thermal boundary conductance  $G_{dLD}$ , and conventional thermal boundary conductance  $G_{cLD}$  from Landauer approach with Bose-Einstein distribution, and NEMD thermal boundary conductance  $G_{NEMD}$  from nonequilibrium molecular dynamics at Si/heavy-Si interface.

The conductance results from both the Landauer approach and NEMD of different mass ratios at 300 K are shown in Fig. 5.5 as  $G_{cLD}$  (cLD means conventional Landauer) and  $G_{NEMD}$ , respectively. It is clear that the Landauer approach predicts smaller interfacial conductances than NEMD, which is consistent with the case of CNT-graphene junction. Also, as the mass ratio decreases, i.e., the interface becomes more matched, the discrepancy increases.

## 5.4 The nonequilibrium Landauer approach

### 5.4.1 The nonequilibrium Landauer approach at Si/heavy-Si interface

In order to explain the discrepancy, we take a closer look at the temperatures in both approaches. NEMD, despite its classical nature and the use of empirical potentials, captures rich physics such as all orders of phonon anharmonicity as well as the

phonon local nonequilibrium across an interface. A modal NEMD approach has shown that the MD temperature can be decomposed into modal phonon temperatures which are in thermal nonequilibrium [110]. Moreover, the modes with high transmission coefficients show smaller modal  $\Delta T$  due to their smaller modal interfacial resistance. In contrast, in the Landauer approach all phonon modes are assumed to be in thermal equilibrium and at the emitted temperature  $T_e$ . Clearly, the Landauer approach misses some physics that NEMD captures. To remedy this, the impact of transmitted phonons on the local temperature should be considered. An equivalent equilibrium temperature, which is the average temperature considering incident, reflected and transmitted phonons, was defined in Ref. [98] to explain the zero resistance across an imaginary interface in a pure material. Here we extend the approach to include modal properties.

Assuming all phonon modes have the same emitted temperatures  $T_{e,1}$  and  $T_{e,2}$  on the two sides respectively, the modal equivalent equilibrium temperature  $T_\lambda$  of phonon mode  $\lambda$  on the two sides, as shown in Fig. 5.4(b), are

$$T_{\lambda,1} = T_{e,1} - \frac{1}{2}(T_{e,1} - T_{e,2}) \int_0^{\frac{\pi}{2}} \tau_{12,AMM}(\omega, \theta) \sin \theta d\theta, \quad (5.38)$$

$$T_{\lambda,2} = T_{e,2} + \frac{1}{2}(T_{e,1} - T_{e,2}) \int_0^{\frac{\pi}{2}} \tau_{21,AMM}(\omega, \theta) \sin \theta d\theta, \quad (5.39)$$

respectively. Here  $\omega$  is the frequency of the corresponding phonon mode  $\lambda$ . The  $T_\lambda$ 's of two representative silicon modes  $\lambda_1$  and  $\lambda_2$  are shown in Fig. 5.4(c). Considering all modes, the lattice equivalent equilibrium temperatures  $T_1$  and  $T_2$  are given by

$$T_1 = \frac{\sum \int_0^{+\infty} T_{\lambda,1} \hbar \omega D_1(\omega) f(T_{e,1}) d\omega}{\sum_p \int_0^{+\infty} \hbar \omega D_1(\omega) f(T_{e,1}) d\omega}, \quad (5.40)$$

$$T_2 = \frac{\sum \int_0^{+\infty} T_{\lambda,2} \hbar \omega D_2(\omega) f(T_{e,2}) d\omega}{\sum_p \int_0^{+\infty} \hbar \omega D_2(\omega) f(T_{e,2}) d\omega}, \quad (5.41)$$

and now these  $T_1$  and  $T_2$  are comparable to  $T_1$  and  $T_2$  in NEMD in Fig. 5.4(a). The local equivalent equilibrium temperature jump  $\Delta T$  becomes

$$\Delta T = T_1 - T_2 = \frac{\sum_p \int_0^{+\infty} T_{\lambda,1} \hbar \omega D_1(\omega) f(T_{e,1}) d\omega}{\sum_p \int_0^{+\infty} \hbar \omega D_1(\omega) f(T_{e,1}) d\omega} - \frac{\sum_p \int_0^{+\infty} T_{\lambda,2} \hbar \omega D_2(\omega) f(T_{e,2}) d\omega}{\sum_p \int_0^{+\infty} \hbar \omega D_2(\omega) f(T_{e,2}) d\omega}, \quad (5.42)$$

and now the TBC  $G$  across the Si/heavy-Si interface can be calculated together with the local equivalent equilibrium temperature jump at the interface as:

$$\begin{aligned} G &= \frac{\frac{A_c}{2} \int_0^{\frac{\pi}{2}} \int_0^{+\infty} \hbar \omega [D_1(\omega) v_{g1}(\omega) \tau_{12}(\theta_1, \omega) (f(T_{e,1}) - f(T_{e,2})) \sin \theta \cos \theta] d\omega d\theta}{T_1 - T_2} \\ &= \frac{\frac{A_c}{2} \int_0^{\frac{\pi}{2}} \int_0^{+\infty} \hbar \omega [D_1(\omega) v_{g1}(\omega) \tau_{12}(\theta_1, \omega) (f(T_{e,1}) - f(T_{e,2})) \sin \theta \cos \theta] d\omega d\theta}{\frac{\sum_p \int_0^{+\infty} T_{\lambda,1} \hbar \omega D_1(\omega) f(T_{e,1}) d\omega}{\sum_p \int_0^{+\infty} \hbar \omega D_1(\omega) f(T_{e,1}) d\omega} - \frac{\sum_p \int_0^{+\infty} T_{\lambda,2} \hbar \omega D_2(\omega) f(T_{e,2}) d\omega}{\sum_p \int_0^{+\infty} \hbar \omega D_2(\omega) f(T_{e,2}) d\omega}}, \end{aligned} \quad (5.43)$$

and the results are shown in Fig. 5.5 as  $G_{dLD}$  (dLD means dressed Landauer).

With the modal equivalent equilibrium temperature  $T_\lambda$ , When the transmission coefficients of all modes are 1, which is equivalent to an imaginary interface in pure material, we have

$$T_{\lambda,1} = T_{e,1} - \frac{1}{2}(T_{e,1} - T_{e,2}) \int_0^{\frac{\pi}{2}} \tau_{12,AMM}(\theta) \sin \theta d\theta = \frac{1}{2}(T_{e,1} + T_{e,2}) = T_{\lambda,2}, \quad (5.44)$$

and

$$T_1 = \frac{\sum_p \int_0^{+\infty} T_{\lambda,1} \hbar \omega D_1(\omega) f(T_{e,1}) d\omega}{\sum_p \int_0^{+\infty} \hbar \omega D_1(\omega) f(T_{e,1}) d\omega} = T_{\lambda,1} = T_{\lambda,2} = T_2, \quad (5.45)$$

which means that the equivalent equilibrium lattice temperatures  $T_1$  and  $T_2$  on the two sides of the interface are equal to each other, and  $\Delta T$  is 0 across the interface. Hence, the TBC becomes infinity when the transmission is set to be 1 for all incident phonon modes. This is also the radiation limit for an imaginary interface.

As shown in Fig. 5.5,  $G_{dLD}$  agrees much better with the results from NEMD than the conventional conductance  $G_{cLD}$  from Landauer approach with phonon emitted temperatures. Also, with equivalent equilibrium temperatures, the trend can now be captured by Landauer approach, that  $G$  is approaching infinity when the mass

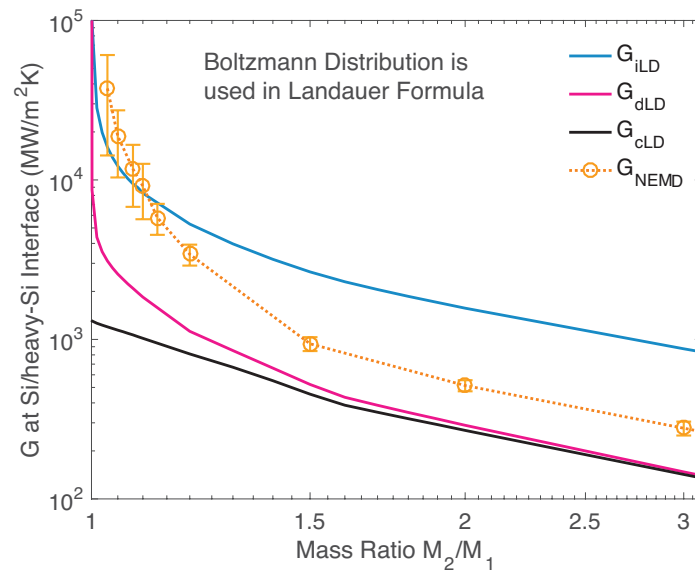


Figure 5.6. The intrinsic thermal boundary conductance  $G_{iLD}$ , dressed thermal boundary conductance  $G_{dLD}$ , and conventional thermal boundary conductance  $G_{cLD}$  from Landauer approach with classical Boltzmann distribution, and NEMD thermal boundary conductance  $G_{NEMD}$  from nonequilibrium molecular dynamics at Si/heavy-Si interface.

ratio  $M_2/M_1$  is approaching 1. However, there is still some difference between  $G_{dLD}$  and  $G_{NEMD}$ . One possible reason is that the phonon population is described by the classical Boltzmann distribution in MD, while the Bose-Einstein distribution is applied in our Landauer calculation. Hence, the Landauer formula has been applied with the classical Boltzmann distribution to compare with NEMD method, and the results are shown in Fig. 5.6. With the same phonon distribution, the results from  $G_{dLD}$  and  $G_{NEMD}$  agree better with each other, but the difference still exist.

In fact, the main reason of the difference between  $G_{dLD}$  and  $G_{NEMD}$  is from our assumption when calculating  $G_{dLD}$  using Landauer formula that all phonon modes have the same emitted temperature  $T_e$ . However, from a recent study [110], it is found that modal emitted temperatures are different for different phonon modes in NEMD simulations, and the difference can be quite large. For high transmission phonon mode, the temperature jump will be mainly at the contacts or inside the leads, which will lead to lower  $T_{e,1}$  and higher  $T_{e,2}$ . As a result, the  $\Delta T_\lambda$  will be smaller than  $T_{\lambda,1} - T_{\lambda,2}$  in Eq. 5.40 and 5.41, and the TBC from NEMD will be higher than the value  $G_{dLD}$  predicted from Landauer formula with lattice equivalent equilibrium temperature  $T_1$  and  $T_2$ .

Hence, the intrinsic TBC  $G_{iLD}$  from Landauer formula is defined to address the issue that phonon emitted temperatures are different for different modes. The intrinsic TBC  $G_{iLD}$  is the sum of all the modal conductance  $G_\lambda$ , and can be calculated as:

$$\begin{aligned} G &= \sum_\lambda G_\lambda = \sum_\lambda \frac{q_\lambda}{\Delta T_\lambda} = \sum_\lambda \frac{q_\lambda}{T_{\lambda,1} - T_{\lambda,2}} \\ &= \sum_\lambda \frac{\frac{A_e}{2} \hbar \omega D_1(\omega) v_{g1}(\omega) \tau_{12}(\theta_1, \omega) (f(T_{e,1}) - f(T_{e,2})) \sin \theta \cos \theta d\omega d\theta}{(T_{e,1} - T_{e,2}) \left(1 - \int_0^{\frac{\pi}{2}} \tau_{12,AMM}(\omega, \theta) \sin \theta d\theta\right)}. \end{aligned} \quad (5.46)$$

The results of  $G_{iLD}$  with Bose-Einstein distribution is shown in Fig. 5.5, while the results with Boltzmann distribution is shown in Fig. 5.6. The results from  $G_{iLD}$  generally give the largest TBC among  $G_{cLD}$ ,  $G_{dLD}$ , and  $G_{iLD}$ . It is because that modal temperature jump across the interface  $\Delta T_\lambda$  is generally smaller than lattice equivalent equilibrium temperature jump  $\Delta T = T_1 - T_2$ , which is mainly limited by the phonon modes existing but not transmitting. The  $G_{iLD}$  can be considered as

an upper limit of the TBC. With the intrinsic TBC  $G_{iLD}$ , the difference between Landauer approach with AMM and NEMD is much smaller now especially at small mass ratio. For larger mass ratio,  $G_{NEMD}$  falls between  $G_{dLD}$  and  $G_{iLD}$ , which is reasonable because part of the phonon modes have similar emitted temperatures, while some high transmission modes have smaller  $\Delta T_e$ . The remaining difference might come from inelastic phonon scattering and the large inaccuracy of TBC in NEMD when the mass ratio is close to 1.

The detailed modal contribution and spectral accumulation of these three TBCs with a mass ratio of 1.05 under Bose-Einstein distribution can be found in Fig. 5.7. For the calculation of  $G_{cLD}$  and  $G_{dLD}$ , the modal heat flow rate  $q_\lambda$  are always the same, each phonon mode shares the same temperature jump at the interface ( $\Delta T_e$  for  $G_{cLD}$  and  $\Delta T$  for  $G_{dLD}$ ), hence the shape of two curves are the same and the difference between them only comes from the amplitude, with a ratio of  $\frac{\Delta T_e}{\Delta T}$ . For the calculation of  $G_{iLD}$ , the modal heat flow rate  $q_\lambda$  are still the same with  $G_{cLD}$  and  $G_{dLD}$ , but the modal temperature jump at the interface  $\Delta T_\lambda$  are different for different modes. So the shape of modal and spectral curves from intrinsic TBC is different from that of  $G_{cLD}$  and  $G_{dLD}$  as shown in Fig. 5.7.

#### 5.4.2 The nonequilibrium Landauer approach at CNT-graphene junction

Then we applied the modal equivalent equilibrium temperature correction to the CNT-graphene interface. Since the incident phonons are one dimensional, the modal equivalent equilibrium temperature on each side of the interface is not incident angle dependent and can be simplified as:

$$T_{\lambda,1} = T_{e,1} - \frac{1}{2}(T_{e,1} - T_{e,2})\tau_{12,AMM}(\omega), \quad (5.47)$$

$$T_{\lambda,2} = T_{e,2} + \frac{1}{2}(T_{e,1} - T_{e,2})\tau_{21,AMM}(\omega). \quad (5.48)$$

From our calculation, it is found that the dressed TBC  $G_{dLD}$  from Landauer with AMM is  $7.7 \times 10^9$  W/m<sup>2</sup>K with the  $T_\lambda$  correction. However, there are still some

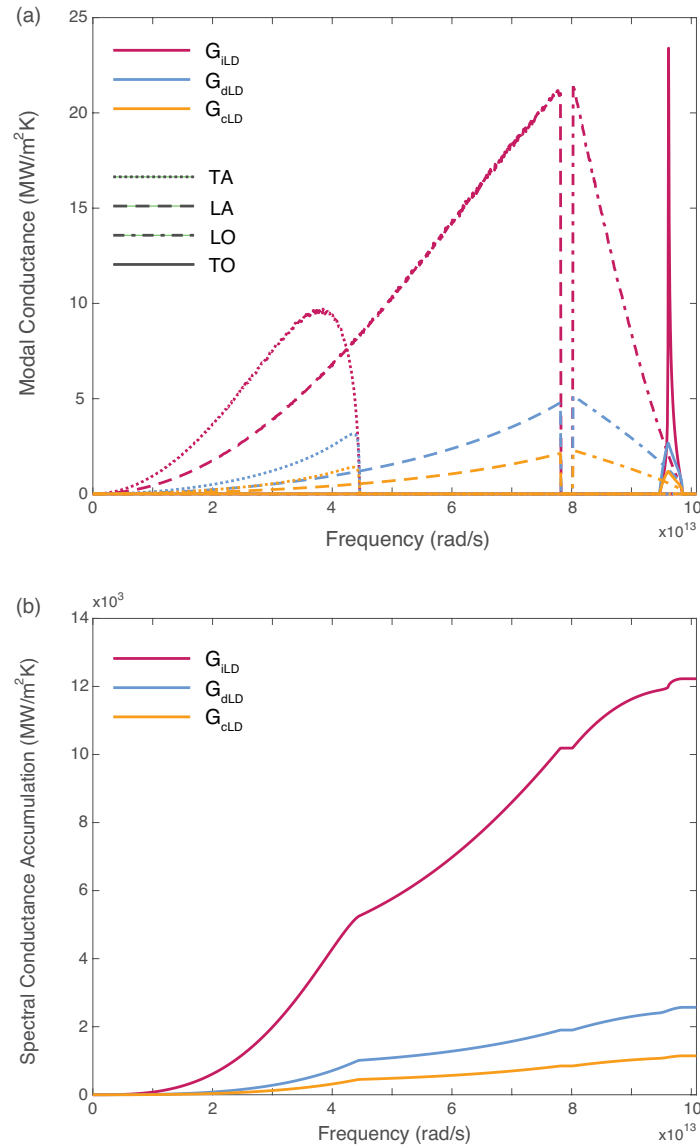


Figure 5.7. (a) Modal conductance and (b) spectral conductance accumulation of intrinsic TBC  $G_{iLD}$ , dressed TBC  $G_{dLD}$ , and conventional TBC  $G_{cLD}$  from Landauer approach with Bose-Einstein distribution at Si/heavy-Si interface with  $M_2/M_1 = 0.6$ .

difference between  $G_{NEMD}$  and  $G_{dLD}$  and the difference might come from the following two factors. The first factor is the carrier statistics difference, that the classical statistics are applied in MD without quantum effects, while Bose-Einstein statistics are applied in the Landauer integral. The second factor is the inaccuracy of transmission coefficient, since AMM assumes planar interface and elastic scattering, while our CNT-graphene interface is curved and there might be some inelastic scattering. To remove the influence of carrier statistics, a Landauer approach with classical statistics is applied between CNT and graphene, and the calculated junction TBC from  $G_{dLD}$  is  $9.0 \times 10^9$  W/m<sup>2</sup>K. Compared to the Bose-Einstein statistics result  $7.7 \times 10^9$  W/m<sup>2</sup>K, the conductance with classical distribution is 14% higher. The difference is because that at 300 K, which is much lower than CNT Debye temperature, some high frequency optical phonon modes are not activated, but the classical distribution function still includes the contribution of this part.

The result from  $G_{dLD}$  with classical statistics is closer to  $G_{NEMD}$ , which is  $1.3 \times 10^{10}$  W/m<sup>2</sup>K. However, there is still some discrepancy and the discrepancy might also come from that the modal phonon emitted temperatures  $T_{e,\lambda}$  are different. So the calculation of  $G_{iLD}$  has been performed for CNT-graphene junction with classical Boltzmann distribution, and this upper limit is  $2.9 \times 10^{13}$  W/m<sup>2</sup>K, which is quite high because CNT and graphene are extremely materials and the transmission of a lot of modes is very close to 1.

Some small difference between  $G_{dLD}$  and  $G_{NEMD}$  might also come from the difference of transmission coefficients from AMM and in NEMD. The difference of transmission coefficients can be divided into two parts. One is related to the inelastic scattering that even the incident phonon frequency is higher than the cut-off frequency on the other side, transmission can still happen. The other is that the phonon transmission at the vertical CNT-graphene (Fig. 5.1(b)) junction is different from that at a planar interface. Also, one incident mode might become multiple modes after transmission. At the CNT-graphene interface, the inelastic scattering should not be very important because 300 K is much lower than the Debye temperature of both CNT and graphene,

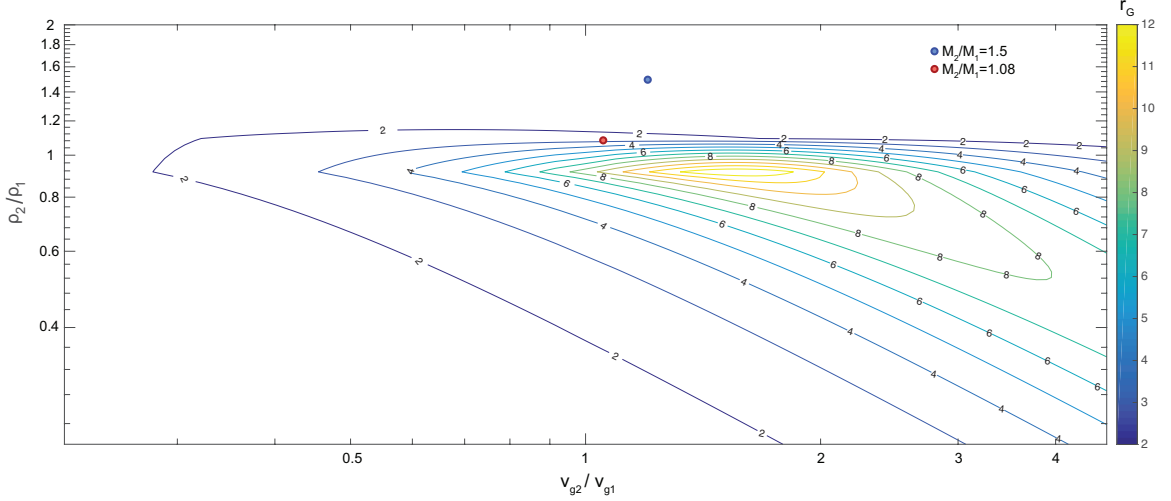


Figure 5.8. The conductance ratio  $r_G$  plot with different mass ratio and phonon group velocity ratio of material 1 and 2.

and the cut-off frequency of CNT and graphene are close to each other. So the difference of transmission coefficients should mainly come from the non-planar interface at the CNT-graphene junction as pointed out by a recent study [108].

#### 5.4.3 A chart to estimate the TBC correction

Now we know that the temperature jump at the interface between the local temperatures  $T_1$  and  $T_2$  across the interface should be smaller than that between the emitted temperatures  $T_{e,1}$  and  $T_{e,2}$  of two reservoirs as shown in Fig. 5.4(b). As a result, the prediction from Landauer formula with  $\Delta T_e$  from emitted temperatures  $T_{e,1}$  and  $T_{e,2}$  will underestimate the conductance across the interface. Because the higher the transmission coefficient, the smaller the temperature difference across the interface, the overestimation will be more important at the interface between highly matched materials like CNT and graphene. The  $T_\lambda$  is needed to correctly calculate  $\Delta T$  to obtain the TBC especially at the interface between highly matched materials. However, the calculation based on  $T_\lambda$  is very complicated because information of all the phonon modes are needed. Hence, a chart to estimate the difference between

TBC with and without correction is created as shown in Fig. 5.8. A TBC ratio  $r_G$  to estimate the difference is defined as:

$$r_G = \frac{G_{dLD}}{G_{cLD}}, \quad (5.49)$$

here  $G_{dLD}$  is the dressed TBC calculated with modal equivalent equilibrium temperature  $T_\lambda$  correction under the assumption that all the incident phonon modes have the same emitted temperature, while  $G_{cLD}$  is the TBC calculated with emitted temperatures  $T_{e,1}$  and  $T_{e,2}$  without  $T_\lambda$  correction.

The mass ratio and phonon group velocity ratio of material 1 and 2 is used to measure the similarity of two materials in the chart. The chart is only a coarse estimation because the phonon dispersion relations of different materials are very different and the group velocity ratio will not hold for all frequency. For Si/heavy-Si interface with mass ratio  $M_2/M_1 = 1.5$ , the  $r_G$  from the chart is 1.2, while the  $r_G$  from the  $T_\lambda$  correction is 1.1. For Si/heavy-Si interface with mass ratio  $M_2/M_1 = 1.08$ , the  $r_G$  from the chart is 2.8, while the  $r_G$  from the  $T_\lambda$  correction is 2.0.

## 5.5 Comparison with Experiments

In the thermal boundary conductance study of ZnO/GaN interface [63], it is found that the Landauer with transmission from DMM under-predicts the thermal boundary conductance measured from experiments by nearly a factor of two, which means  $r_G$  is about 1.6 to 2. From our  $r_G$  estimation chart, the  $r_G$  is found to be about 1.5. Even though the estimation of  $r_G$  from the chart is not exactly accurate, it is still a good approximation of how the similarity will affect the TBC. The TBC and TBR results from the conventional Landauer formula with emitted temperature can be easily corrected with the chart.

We have also applied the detailed Landauer formula calculation for thermal boundary conductance at ZnO/GaN interface with transmission from both AMM and DMM with modal equivalent equilibrium temperature correction. All the phonon properties are calculated from first principles calculation. The comparison between our results

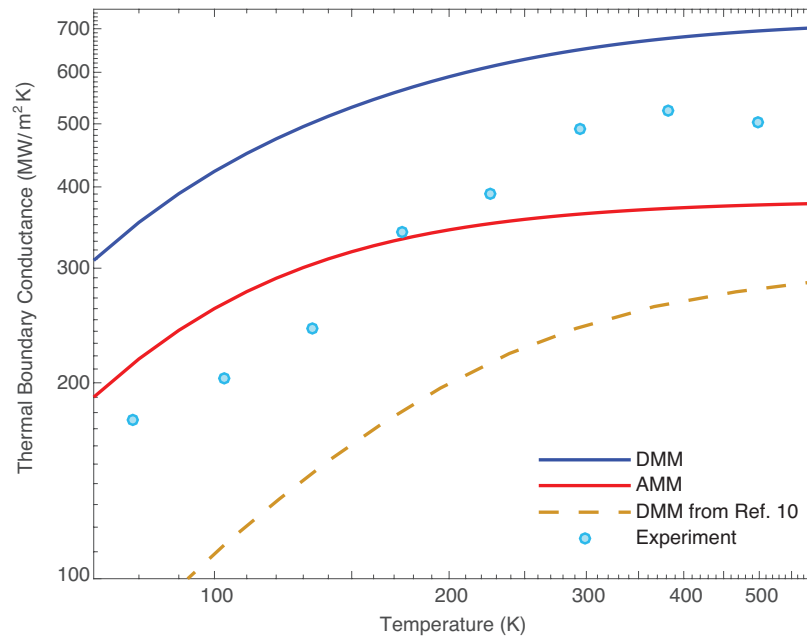


Figure 5.9. The comparison between TBC at ZnO/GaN interface from experiments and Landauer formula.

with the experimental and DMM results from Ref. 10 is shown in Fig. 5.9. With the temperature correction, the Landauer approach agrees much better with experimental results.

## 5.6 Summary

To summarize, the Landauer approach with transmission from mismatch models is often applied to predict the TBC at the interface, and it is usually considered as a good method because it is predictive and not time-consuming. However, sometimes there is a large difference between the Landauer results and experimental or modeling results. From the CNT-graphene and Si/heavy-Si interface, we found that for the application of Landauer, the  $\Delta T$  at the interface is very important and will lead to large discrepancy if not calculated properly. With the correction from modal equivalent equilibrium temperature  $T_\lambda$ , the Landauer formula works much better predicting the TBC. We need to be very careful when using Landauer formula, especially at the interface between highly matched materials. To easily estimate the difference between TBC with and without correction, a chart is created based on the mass ratio and phonon group velocity ratio of material 1 and 2 across the interface. The estimation from the chart is in good agreement with the observed discrepancy.

## 6. SUMMARY

In this work, we have explored thermal transport across dimensionally mismatched interfaces in pillared graphene. Because of the heat dissipation issue in nano-devices, low dimensional materials like CNT and graphene are promising for their extremely high thermal conductivity. For three dimensional thermal transport, 3D hierarchical structure like pillared graphene is proposed and synthesized. However, heat transfer in these materials is not well understood. We have studied the thermal transport of materials with dimensionally mismatched interfaces in the following three steps.

First, by recognizing that thermal resistance of the 3D pillared graphene architecture primarily comes from CNT-graphene junctions, a simple network model of thermal transport in pillared graphene structure is developed. Using non-equilibrium molecular dynamics, the resistance across an individual CNT-graphene junction with  $sp^2$  covalent bonds is found to be around  $6 \times 10^{-11}$  m<sup>2</sup>K/W, which is significantly lower than typical values reported for planar interfaces between dissimilar materials. In contrast, the resistance across a van der Waals junction is about  $4 \times 10^{-8}$  m<sup>2</sup>K/W. Interestingly, when the CNT pillar length is small, the interfacial resistance of the  $sp^2$  covalent junction is found to decrease as the CNT pillar length decreases, suggesting the presence of coherence effects. To explain this intriguing trend, the junction thermal resistance is decomposed into interfacial region and boundary components, and it is found that while the boundary resistance has little dependence on the pillar length, the interfacial region resistance decreases as the pillar length decreases. This is explained by calculating the local phonon density of states (LDOS) of different regions near the boundary. The LDOS overlap between the interfacial region and the center region of CNT increases as the pillar length decreases, leading to the decrease of interfacial region resistance. The junction resistance  $R_j$  is eventually used in the

network model to estimate the effective thermal conductivity, and the results agree well with direct MD simulation data, demonstrating the effectiveness of our model.

Then we study three different mechanisms which can lead to thermal resistances across the pillared graphene junction: the material mismatch (phonon propagates from CNT to graphene), the non-planar junction (the phonon propagation direction must change), and defects (there are six heptagons at each junction). The contributions of different mechanisms to the total junction thermal resistances are not clear from the previous NEMD simulation, which can only give an overall resistance. To understand the effects on the resistance of different mechanisms, we have decomposed the junction thermal resistance of pillared-graphene junction to different mechanisms and calculated the thermal resistance caused by each mechanism. We performed NEMD simulations to compare five types of different junctions corresponding for different mechanisms: unzipped CNT to isolate the effects of materials mismatch; CNT with single vacancy and Stone-Wales defects to isolate the effects of defects; vertical CNT-CNT junction, and 30 degree CNT-CNT junction to capture the effects of non-planar junction and other mechanisms. The NEMD results show that three mechanisms lead to similar resistance at the CNT-graphene junction.

Furthermore, we have predicted the transmission function of individual phonon mode using the wave packet method at CNT-graphene junction, which is a dimensionally mismatched interface between 1D and 2D materials. Intriguing phonon polarization conversion behavior is observed for most incident phonon modes. It is found that the polarization conversion dominates the transmission and is more significant at larger phonon wavelength. We attribute such unique phonon polarization conversion behavior to the dimensional mismatch across CNT-graphene interface. The transmission coefficients of our wave packet method and AMM are compared with each other. It is found that the transmission functions at the junction cannot be predicted by the conventional acoustic mismatch models due to the existence of dimensional mismatch. Then we used Landauer formula with transmission functions from both wave packet method and AMM to predict the interface conductance. For the incident

LA polarization, the results of two methods are similar, while for RB, the conductance from wave packet method is much larger, and for TA and TW, AMM predict larger conductance. The dimensionally mismatched interface, on one hand tends to reduce the transmission and conductance due to defects and the change of phonon propagation direction at the interface, while on the other hand tends to enhance the transmission and conductance due to the new phonon transport channel introduced by polarization conversion.

Finally, from the observation that the measured thermal boundary conductance from many recent experiments is much larger than those calculated from the theoretical Landauer approach, we find the assumption of local equilibrium of conventional is not valid and will lead to the discrepancy between Landauer and experiments. With the correction from modal equivalent equilibrium temperature  $T_\lambda$ , the Landauer formula works much better predicting the TBC. We need to be very careful when using Landauer formula, especially at the interface between highly matched materials. To easily estimate the difference between TBC with and without correction, a convenient chart is created to estimate the conductance correction based on our approach, and it yields quite accurate results. The correction of conventional Landauer approach will help to estimate TBC at interfaces with a fast and accurate method.

The results obtained in this thesis will provide a deeper understanding of nanoscale thermal transport across interfaces. This research also provides new perspectives of atomic- and nano-scale engineering of materials and structures to enhance performance of thermal management.

## REFERENCES

## REFERENCES

- [1] CHARLES M. LIEBER. The incredible shrinking circuit. *Scientific American*, 285(3):58–64, 2001.
- [2] Philip G. Collins and Phaedon Avouris. Nanotubes for Electronics. *Scientific American*, 283(6):62–69, dec 2000.
- [3] Max Schulz. The end of the road for silicon? *Nature*, 399(6738):729–730, jun 1999.
- [4] Chris A. Mack. Fifty Years of Moore’s Law. *IEEE Transactions on Semiconductor Manufacturing*, 24(2):202–207, may 2011.
- [5] M. Mitchell Waldrop. The chips are down for Moore’s law. *Nature*, 530(7589):144–147, feb 2016.
- [6] L. Lindsay, D. A. Broido, and T. L. Reinecke. First-Principles Determination of Ultrahigh Thermal Conductivity of Boron Arsenide: A Competitor for Diamond? *Physical Review Letters*, 111(2):025901, jul 2013.
- [7] Fei Tian, Bai Song, Xi Chen, Navaneetha K. Ravichandran, Yinchuan Lv, Ke Chen, Sean Sullivan, Jaehyun Kim, Yuanyuan Zhou, Te-Huan Liu, Miguel Goni, Zhiwei Ding, Jingying Sun, Geethal Amila Gamage Udalamatta Gamage, Haoran Sun, Hamidreza Ziyae, Shuyuan Huyan, Liangzi Deng, Jianshi Zhou, Aaron J. Schmidt, Shuo Chen, Ching-Wu Chu, Pinshane Y Huang, David Broido, Li Shi, Gang Chen, and Zhifeng Ren. Unusual high thermal conductivity in boron arsenide bulk crystals. *Science*, 8982(July):eaat7932, jul 2018.
- [8] Joon Sang Kang, Man Li, Huan Wu, Huuduy Nguyen, and Yongjie Hu. Experimental observation of high thermal conductivity in boron arsenide. *Science*, 5522(July):eaat5522, jul 2018.
- [9] S Li, Sheng Li, Qiye Zheng, Yinchuan Lv, Xiaoyuan Liu, Xiqu Wang, Pinshane Y Huang, G David, and Bing Lv. High thermal conductivity in cubic boron arsenide crystals. *Science*, 8982(July):1–9, 2018.
- [10] Zhiqiao Kuang, Yulong Chen, Yonglai Lu, Li Liu, Shui Hu, Shipeng Wen, Yingyan Mao, and Liqun Zhang. Fabrication of Highly Oriented Hexagonal Boron Nitride Nanosheet/Elastomer Nanocomposites with High Thermal Conductivity. *Small*, 11(14):1655–1659, apr 2015.
- [11] Gun-Ho Kim, Dongwook Lee, Apoorv Shanker, Lei Shao, Min Sang Kwon, David Gidley, Jinsang Kim, and Kevin P. Pipe. High thermal conductivity in amorphous polymer blends by engineered interchain interactions. *Nature Materials*, 14(3):295–300, mar 2015.

- [12] Jing Yang, Enwei Zhang, Xiaofeng Li, Yiting Zhang, Jin Qu, and Zhong-Zhen Yu. Cellulose/graphene aerogel supported phase change composites with high thermal conductivity and good shape stability for thermal energy storage. *Carbon*, 98:50–57, mar 2016.
- [13] Alexander A. Balandin. Thermal properties of graphene and nanostructured carbon materials. *Nature Materials*, 10(8):569–581, aug 2011.
- [14] Junichiro Shiomi and Shigeo Maruyama. Non-Fourier heat conduction in a single-walled carbon nanotube: Classical molecular dynamics simulations. *Physical Review B*, 73(20):205420, may 2006.
- [15] L Lindsay, D A Broido, and Natalio Mingo. Diameter dependence of carbon nanotube thermal conductivity and extension to the graphene limit. *Physical Review B*, 82(16):161402, oct 2010.
- [16] Bo Qiu, Yan Wang, Qing Zhao, and Xiulin Ruan. The effects of diameter and chirality on the thermal transport in free-standing and supported carbon-nanotubes. *Applied Physics Letters*, 100(23), 2012.
- [17] Alexander A Balandin, Suchismita Ghosh, Wenzhong Bao, Irene Calizo, Desalegne Teweldebrhan, Feng Miao, and Chun Ning Lau. Superior Thermal Conductivity of Single-Layer Graphene. *Nano Letters*, 8(3):902–907, mar 2008.
- [18] L Lindsay, D A Broido, and Natalio Mingo. Flexural phonons and thermal transport in graphene. *Physical Review B*, 82(11):115427, sep 2010.
- [19] Yan Wang, Bo Qiu, and Xiulin Ruan. Edge effect on thermal transport in graphene nanoribbons: A phonon localization mechanism beyond edge roughness scattering. *Applied Physics Letters*, 101(1):13101, jul 2012.
- [20] Jiuning Hu, Xiulin Ruan, and Yong P Chen. Thermal Conductivity and Thermal Rectification in Graphene Nanoribbons: A Molecular Dynamics Study. *Nano Letters*, 9(7):2730–2735, jul 2009.
- [21] Georgios K Dimitrakakis, Emmanuel Tylianakis, and George E Froudakis. Pillared Graphene: A New 3-D Network Nanostructure for Enhanced Hydrogen Storage. *Nano Letters*, 8(10):3166–3170, oct 2008.
- [22] Zhen Yao, Henk W Ch. Postma, Leon Balents, and Cees Dekker. Carbon nanotube intramolecular junctions. *Nature*, 402(6759):273–276, nov 1999.
- [23] Vikas Varshney, Ajit K Roy, George Froudakis, and Barry L Farmer. Molecular dynamics simulations of thermal transport in porous nanotube network structures. *Nanoscale*, 3(9):3679–3684, 2011.
- [24] Jingjing Shi, Yalin Dong, Timothy Fisher, and Xiulin Ruan. Thermal transport across carbon nanotube-graphene covalent and van der Waals junctions. *Journal of Applied Physics*, 118(4):044302, 2015.
- [25] Jingjing Shi, Yang Zhong, Timothy S Fisher, and Xiulin Ruan. Decomposition of the Thermal Boundary Resistance across Carbon Nanotube-Graphene Junctions to Different Mechanisms. *ACS Applied Materials & Interfaces*, 10(17):15226–15231, may 2018.

- [26] Y. B. Shi, S. Mei, O. Jonasson, and I. Knezevic. Modeling quantum cascade lasers: Coupled electron and phonon transport far from equilibrium and across disparate spatial scales. *Fortschritte der Physik*, 65(6-8):1600084, jun 2017.
- [27] Yu Yao, Anthony J. Hoffman, and Claire F. Gmachl. Mid-infrared quantum cascade lasers. *Nature Photonics*, 6(7):432–439, jul 2012.
- [28] Jerome Faist, Federico Capasso, Deborah L Sivco, Carlo Sirtori, Albert L Hutchinson, and Alfred Y Cho. Quantum Cascade Laser. *Science*, 264(5158):553–556, apr 1994.
- [29] Eric Pop. Energy dissipation and transport in nanoscale devices. *Nano Research*, 3(3):147–169, mar 2010.
- [30] Eric Pop, Sanjiv Sinha, and K.E. Goodson. Heat Generation and Transport in Nanometer-Scale Transistors. *Proceedings of the IEEE*, 94(8):1587–1601, aug 2006.
- [31] David G. Cahill, Wayne K. Ford, Kenneth E. Goodson, Gerald D. Mahan, Arun Majumdar, Humphrey J. Maris, Roberto Merlin, and Simon R. Phillpot. Nanoscale thermal transport. *Journal of Applied Physics*, 93(2):793–818, jan 2003.
- [32] T. C. Harman. Quantum Dot Superlattice Thermoelectric Materials and Devices. *Science*, 297(5590):2229–2232, sep 2002.
- [33] Ihtesham Chowdhury, Ravi Prasher, Kelly Lofgreen, Gregory Chrysler, Sridhar Narasimhan, Ravi Mahajan, David Koester, Randall Alley, and Rama Venkatasubramanian. On-chip cooling by superlattice-based thin-film thermoelectrics. *Nature Nanotechnology*, 4(4):235–238, apr 2009.
- [34] R. Venkatasubramanian, E. Siivola, T. Colpitts, and B. O’Quinn. Thin-film thermoelectric devices with high room-temperature figures of merit. *Nature*, 413(6856):597–602, 2001.
- [35] Yan Wang, Haoxiang Huang, and Xiulin Ruan. Decomposition of coherent and incoherent phonon conduction in superlattices and random multilayers. *Physical Review B*, 90(16):165406, oct 2014.
- [36] Jialong Zhao, Julie A. Bardecker, Andrea M. Munro, Michelle S. Liu, Yuhua Niu, I-Kang Ding, Jingdong Luo, Baoquan Chen, Alex K.Y. Jen, and David S. Ginger. Efficient CdSe/CdS Quantum Dot Light-Emitting Diodes Using a Thermally Polymerized Hole Transport Layer. *Nano Letters*, 6(3):463–467, mar 2006.
- [37] Shuji Nakamura, Takashi Mukai, and Masayuki Senoh. Candelaclass highbrightness InGaN/AlGaN doubleheterostructure bluelightemitting diodes. *Applied Physics Letters*, 64(13):1687–1689, mar 1994.
- [38] Yuan Ma, Zhilong He, Xueyuan Peng, and Ziwen Xing. Experimental investigation of the discharge valve dynamics in a reciprocating compressor for transcritical CO2 refrigeration cycle. *Applied Thermal Engineering*, 32:13–21, jan 2012.

- [39] Jonghoon Lee, Vikas Varshney, Joshua S Brown, Ajit K Roy, and Barry L Farmer. Single mode phonon scattering at carbon nanotube-graphene junction in pillared graphene structure. *Applied Physics Letters*, 100(18):183111, may 2012.
- [40] Yuhua Xue, Yong Ding, Jianbing Niu, Zhenhai Xia, Ajit Roy, Hao Chen, Jia Qu, Zhong Lin Wang, and Liming Dai. Rationally designed graphene-nanotube 3D architectures with a seamless nodal junction for efficient energy conversion and storage. *Science Advances*, 1(8):e1400198, 2015.
- [41] Ivan Duchemin and Davide Donadio. Atomistic calculation of the thermal conductance of large scale bulk-nanowire junctions. *Physical Review B - Condensed Matter and Materials Physics*, 84(11):1–6, 2011.
- [42] Baratunde A. Cola, Jun Xu, Changrui Cheng, Xianfan Xu, Timothy S. Fisher, and Hanping Hu. Photoacoustic characterization of carbon nanotube array thermal interfaces. *Journal of Applied Physics*, 101(5), 2007.
- [43] Ming Hu, Pawel Koblinski, Jian Sheng Wang, and Nachiket Raravikar. Interfacial thermal conductance between silicon and a vertical carbon nanotube. *Journal of Applied Physics*, 104(8), 2008.
- [44] Yan Wang, Xiulin Ruan, and Ajit K Roy. Two-temperature nonequilibrium molecular dynamics simulation of thermal transport across metal-nonmetal interfaces. *Physical Review B*, 85(20):205311, may 2012.
- [45] Ravi Prasher, Tao Tong, and Arun Majumdar. An acoustic and dimensional mismatch model for thermal boundary conductance between a vertical mesoscopic nanowire/nanotube and a bulk substrate. *Journal of Applied Physics*, 102(10):104312, nov 2007.
- [46] Jae Hun Seol, Insun Jo, Arden L Moore, Lucas Lindsay, Zachary H Aitken, Michael T Pettes, Xuesong Li, Zhen Yao, Rui Huang, David Broido, Natalio Mingo, Rodney S Ruoff, and Li Shi. Two-dimensional phonon transport in supported graphene. *Science (New York, N.Y.)*, 328(5975):213–6, 2010.
- [47] Zuyuan Wang, Tianli Feng, and Xiulin Ruan. Thermal conductivity and spectral phonon properties of freestanding and supported silicene. *Journal of Applied Physics*, 117(8), 2015.
- [48] E. T. Swartz and R. O. Pohl. Thermal boundary resistance. *Reviews of Modern Physics*, 61(3):605–668, 1989.
- [49] P Kim, L Shi, A Majumdar, and P L McEuen. Thermal Transport Measurements of Individual Multiwalled Nanotubes. *Physical Review Letters*, 87(21):215502, oct 2001.
- [50] Eric Pop, David Mann, Qian Wang, Kenneth Goodson, and Hongjie Dai. Thermal Conductance of an Individual Single-Wall Carbon Nanotube above Room Temperature. *Nano Letters*, 6(1):96–100, jan 2006.
- [51] Alexander A Balandin. Thermal properties of graphene and nanostructured carbon materials. *Nature Materials*, 10(8):569–581, jul 2011.

- [52] Jianwei Che, Tahir Cagin, and Wa Goddard. Thermal conductivity of carbon nanotubes. *Nanotechnology*, 11:65–69, 2000.
- [53] Vikas Varshney, Soumya S Patnaik, Ajit K Roy, George Froudakis, and Barry L Farmer. Modeling of Thermal Transport in Pillared-Graphene Architectures. *ACS Nano*, 4(2):1153–1161, feb 2010.
- [54] Jungkyu Park and Vikas Prakash. Thermal transport in 3D pillared SWCNT-graphene nanostructures. *Journal of Materials Research*, 28(07):940–951, 2013.
- [55] Patrick K. Schelling, Simon R. Phillpot, and Pawel Koblinski. Comparison of atomic-level simulation methods for computing thermal conductivity. *Physical Review B*, 65(14):144306, April 2002.
- [56] Florian Müller-Plathe. A simple nonequilibrium molecular dynamics method for calculating the thermal conductivity. *The Journal of Chemical Physics*, 106(14):6082–6085, apr 1997.
- [57] P. K. Schelling, S. R. Phillpot, and P. Koblinski. Phonon wave-packet dynamics at semiconductor interfaces by molecular-dynamics simulation. *Applied Physics Letters*, 80(14):2484–2486, apr 2002.
- [58] Alan J H Mcgaughey and Jason M Larkin. CHAPTER 3 PREDICTING PHONON PROPERTIES FROM EQUILIBRIUM MOLECULAR DYNAMICS SIMULATIONS 1 . 1 Motivation : Thermal Conductivity Prediction. *Annual Review of Heat Transfer*, 17(N/A):49–87, 2014.
- [59] Kouichi Tanaka, Shuji Ogata, Ryo Kobayashi, Tomoyuki Tamura, and Takahisa Kouno. A molecular dynamics study on thermal conductivity of thin epoxy polymer sandwiched between alumina fillers in heat-dissipation composite material. *International Journal of Heat and Mass Transfer*, 89:714–723, oct 2015.
- [60] Timothy S. Fisher. Landauer transport formalism. In *Thermal Energy at the Nanoscale*, pages 87–111. WORLD SCIENTIFIC, dec 2013.
- [61] M. L. Huberman and A. W. Overhauser. Electronic Kapitza conductance at a diamond-Pb interface. *Physical Review B*, 50(5):2865, 1994.
- [62] Ming Hu, Pawel Koblinski, and Patrick K. Schelling. Kapitza conductance of siliconamorphous polyethylene interfaces by molecular dynamics simulations. *Physical Review B*, 79(10):104305, mar 2009.
- [63] John T. Gaskins, George Kotsonis, Ashutosh Giri, Christopher T. Shelton, Edward Sachet, Zhe Cheng, Brian M. Foley, Zeyu Liu, Shenghong Ju, Junichiro, Mark S. Goorsky, Samuel Graham, Tengfei Luo, Asegun Henry, Jon-Paul Maria, and Patrick E. Hopkins. Thermal boundary conductance across epitaxial ZnO/GaN interfaces: Assessment of phonon gas models and atomistic Green’s function approaches for predicting interfacial phonon transport. (Dmm):1–7, oct 2017.
- [64] Patrick E. Hopkins. Multiple phonon processes contributing to inelastic scattering during thermal boundary conductance at solid interfaces. *Journal of Applied Physics*, 106(1):013528, jul 2009.

- [65] Magnus Paulsson, Thomas Frederiksen, and Mads Brandbyge. Modeling inelastic phonon scattering in atomic- and molecular-wire junctions. *Physical Review B*, 72(20):201101, nov 2005.
- [66] Sridhar Sadasivam, Ning Ye, Joseph P. Feser, James Charles, Kai Miao, Tillmann Kubis, and Timothy S. Fisher. Thermal transport across metal silicide-silicon interfaces: First-principles calculations and Green's function transport simulations. *Physical Review B*, 95(8):1–15, 2017.
- [67] Tingyu Lu, Jun Zhou, Tsuneyoshi Nakayama, Ronggui Yang, and Baowen Li. Interfacial thermal conductance across metal-insulator/semiconductor interfaces due to surface states. *Physical Review B*, 93(8):085433, feb 2016.
- [68] Zexi Lu, Yan Wang, and Xiulin Ruan. Metal/dielectric thermal interfacial transport considering cross-interface electron-phonon coupling: Theory, two-temperature molecular dynamics, and thermal circuit. *Physical Review B*, 93(6):064302, feb 2016.
- [69] Keng-Hua Lin and Alejandro Strachan. Role of direct electron-phonon coupling across metal-semiconductor interfaces in thermal transport via molecular dynamics. *The Journal of Chemical Physics*, 143(3):034703, jul 2015.
- [70] Patrick E. Hopkins, Jared L. Kassebaum, and Pamela M. Norris. Effects of electron scattering at metal-nonmetal interfaces on electron-phonon equilibration in gold films. *Journal of Applied Physics*, 105(2):023710, jan 2009.
- [71] M. Rosochowska, K. Chodnikiewicz, and R. Balendra. A new method of measuring thermal contact conductance. *Journal of Materials Processing Technology*, 145(2):207–214, jan 2004.
- [72] Donald W Brenner, Olga a Shenderova, Judith a Harrison, Steven J Stuart, Boris Ni, and Susan B Sinnott. A second-generation reactive empirical bond order (REBO) potential energy expression for hydrocarbons. *Journal of Physics: Condensed Matter*, 14(4):783–802, feb 2002.
- [73] Steven J. Stuart, Alan B. Tutein, and Judith A. Harrison. A reactive potential for hydrocarbons with intermolecular interactions. *The Journal of Chemical Physics*, 112(14):6472–6486, April 2000.
- [74] Tienchong Chang, Juan Hou, and Xingming Guo. Reversible mechanical bistability of single-walled carbon nanotubes under axial strain. *Applied Physics Letters*, 88(21):211906, 2006.
- [75] S.-M. Lee and David G. Cahill. Heat transport in thin dielectric films. *Journal of Applied Physics*, 81(6):2590, 1997.
- [76] Patrick E. Hopkins, Pamela M. Norris, Robert J. Stevens, Thomas E. Beechem, and Samuel Graham. Influence of Interfacial Mixing on Thermal Boundary Conductance Across a Chromium/Silicon Interface. *Journal of Heat Transfer*, 130(6):062402, 2008.
- [77] Mark D. Losego, Martha E. Grady, Nancy R. Sottos, David G. Cahill, and Paul V. Braun. Effects of chemical bonding on heat transport across interfaces. *Nature Materials*, 11(6):502–506, April 2012.

- [78] Seungha Shin, Massoud Kaviani, Tapan Desai, and Richard Bonner. Roles of atomic restructuring in interfacial phonon transport. *Physical Review B*, 82(8):081302, August 2010.
- [79] H. Bao, X. L. Ruan, and M. Kaviani. Theory of the broadening of vibrational spectra induced by lowered symmetry in yttria nanostructures. *Physical Review B*, 78(12):125417, September 2008.
- [80] S Ghosh, I Calizo, D Teweldebrhan, E P Pokatilov, D L Nika, A A Balandin, W Bao, F Miao, and C N Lau. Extremely high thermal conductivity of graphene: Prospects for thermal management applications in nanoelectronic circuits. *Applied Physics Letters*, 92(15):151911–151913, apr 2008.
- [81] Bo Qiu and Xiulin Ruan. Reduction of spectral phonon relaxation times from suspended to supported graphene. *Applied Physics Letters*, 100(19):193101, may 2012.
- [82] Guangli Che, Brinda B Lakshmi, Ellen R Fisher, and Charles R Martin. Carbon nanotubule membranes for electrochemical energy storage and production. *Nature*, 393(6683):346–349, may 1998.
- [83] Cathie Vix-Guterl, Elzbieta Frackowiak, Krzysztof Jurewicz, Marcin Friebe, Julien Parmentier, and François Béguin. Electrochemical energy storage in ordered porous carbon materials. *Carbon*, 43(6):1293–1302, may 2005.
- [84] Da-Wei Wang, Feng Li, Min Liu, Gao Qing Lu, and Hui-Ming Cheng. 3D Aperiodic Hierarchical Porous Graphitic Carbon Material for High-Rate Electrochemical Capacitive Energy Storage. *Angewandte Chemie International Edition*, 47(2):373–376, jan 2008.
- [85] Seyed Hamed Aboutalebi, Rouhollah Jalili, Dorna Esrafilzadeh, Maryam Salari, Zahra Gholamvand, Sima Aminorroaya Yamini, Konstantin Konstantinov, Roderick L. Shepherd, Jun Chen, Simon E. Moulton, Peter Charles Innis, Andrew I. Minett, Joselito M. Razal, and Gordon G. Wallace. High-Performance Multifunctional Graphene Yarns: Toward Wearable All-Carbon Energy Storage Textiles. *ACS Nano*, 8(3):2456–2466, mar 2014.
- [86] Steven L. Mielke, Diego Troya, Sulin Zhang, Je-Luen Li, Shaoping Xiao, Roberto Car, Rodney S. Ruoff, George C. Schatz, and Ted Belytschko. The role of vacancy defects and holes in the fracture of carbon nanotubes. *Chemical Physics Letters*, 390(4-6):413–420, jun 2004.
- [87] N. Chandra, S. Namilae, and C. Shet. Local elastic properties of carbon nanotubes in the presence of Stone-Wales defects. *Physical Review B*, 69(9):094101, mar 2004.
- [88] Dmitry V Kosynkin, Amanda L Higginbotham, Alexander Sinitskii, Jay R Lomeda, Ayrat Dimiev, B Katherine Price, and James M Tour. Longitudinal unzipping of carbon nanotubes to form graphene nanoribbons. *Nature*, 458(7240):872–876, apr 2009.
- [89] Ji-hang Zou, Zhen-qiang Ye, and Bing-yang Cao. Phonon thermal properties of graphene from molecular dynamics using different potentials. *The Journal of Chemical Physics*, 145(13):134705, 2016.

- [90] L. Lindsay and D. A. Broido. Optimized Tersoff and Brenner empirical potential parameters for lattice dynamics and phonon thermal transport in carbon nanotubes and graphene. *Physical Review B*, 81(20):205441, may 2010.
- [91] Robert J. Stevens, Leonid V. Zhigilei, and Pamela M. Norris. Effects of temperature and disorder on thermal boundary conductance at solid-solid interfaces: Nonequilibrium molecular dynamics simulations. *International Journal of Heat and Mass Transfer*, 50(19-20):3977–3989, 2007.
- [92] Richard N. Salaway and Leonid V. Zhigilei. Molecular dynamics simulations of thermal conductivity of carbon nanotubes: Resolving the effects of computational parameters. *International Journal of Heat and Mass Transfer*, 70:954–964, 2014.
- [93] Zhi Liang and Pawel Koblinski. Finite-size effects on molecular dynamics interfacial thermal-resistance predictions. *Physical Review B - Condensed Matter and Materials Physics*, 90(7):1–12, 2014.
- [94] Z. T. Tian, B. E. White, and Y. Sun. Phonon wave-packet interference and phonon tunneling based energy transport across nanostructured thin films. *Applied Physics Letters*, 96(26):263113, 2010.
- [95] Lin Sun and Jayathi Y. Murthy. Molecular Dynamics Simulation of Phonon Scattering at Silicon/Germanium Interfaces. *Journal of Heat Transfer*, 132(10):102403, 2010.
- [96] Huai Sun, Stephen J Mumby, Jon R Maple, and Arnold T Hagler. An ab Initio CFF93 All-Atom Force Field for Polycarbonates. *Journal of the American Chemical Society*, 116(3):2978–2987, 1994.
- [97] H Sun. COMPASS: An ab Initio Force-Field Optimized for Condensed-Phase Applications Overview with Details on Alkane and Benzene Compounds. *Journal of Physical Chemistry B*, 5647(98):7338–7364, 1998.
- [98] Taofang Zeng, Gang Chen. NONEQUILIBRIUM PHONON AND ELECTRON TRANSPORT IN HETEROSTRUCTURES AND SUPERLATTICES. *Microscale Thermophysical Engineering*, 5(2):71–88, apr 2001.
- [99] J.-H. Ahn, H.-S. Kim, Keon Jae Lee, Seokwoo Jeon, Seong Jun Kang, Yungang Sun, Ralph G Nuzzo, and John a Rogers. Heterogeneous Three-Dimensional Electronics by Use of Printed Semiconductor Nanomaterials. *Science*, 314(5806):1754–1757, dec 2006.
- [100] W. A. Little. THE TRANSPORT OF HEAT BETWEEN DISSIMILAR SOLIDS AT LOW TEMPERATURES. *Canadian Journal of Physics*, 37(3):334–349, mar 1959.
- [101] R J Stoner and H J Maris. Kapitza conductance and heat flow between solids at temperatures from 50 to 300 K. *Physical Review B*, 48(22):16373–16387, dec 1993.
- [102] John C. Duda, Thomas E. Beechem, Justin L. Smoyer, Pamela M. Norris, and Patrick E. Hopkins. Role of dispersion on phononic thermal boundary conductance. *Journal of Applied Physics*, 108(7):073515, oct 2010.

- [103] Xiaobo Li and Ronggui Yang. Effect of lattice mismatch on phonon transmission and interface thermal conductance across dissimilar material interfaces. *Physical Review B - Condensed Matter and Materials Physics*, 86(5), 2012.
- [104] Pamela M. Norris, Nam Q. Le, and Christopher H. Baker. Tuning Phonon Transport: From Interfaces to Nanostructures. *Journal of Heat Transfer*, 135(6):061604, may 2013.
- [105] Yanguang Zhou, Zheyong Fan, Guangzhao Qin, Jia-Yue Yang, Tao Ouyang, and Ming Hu. Methodology Perspective of Computing Thermal Transport in Low-Dimensional Materials and Nanostructures: The Old and the New. *ACS Omega*, 3(3):3278–3284, mar 2018.
- [106] Changwook Jeong, Supriyo Datta, and Mark Lundstrom. Thermal conductivity of bulk and thin-film silicon: A Landauer approach. *Journal of Applied Physics*, 111(9), 2012.
- [107] Ho Ki Lyeo and David G. Cahill. Thermal conductance of interfaces between highly dissimilar materials. *Physical Review B - Condensed Matter and Materials Physics*, 73(14):1–6, 2006.
- [108] Jingjing Shi, Jonghoon Lee, Yalin Dong, Ajit Roy, Timothy S Fisher, and Xiulin Ruan. Dominant phonon polarization conversion across dimensionally mismatched interfaces: Carbon-nanotubegraphene junction. *Physical Review B*, 97(13):134309, apr 2018.
- [109] K. Miao, S. Sadasivam, J. Charles, G. Klimeck, T. S. Fisher, and T. Kubis. Büttiker probes for dissipative phonon quantum transport in semiconductor nanostructures. *Applied Physics Letters*, 108(11):113107, mar 2016.
- [110] Tianli Feng, Wenjun Yao, Zuyuan Wang, Jingjing Shi, Chuang Li, Bingyang Cao, and Xiulin Ruan. Spectral analysis of nonequilibrium molecular dynamics: Spectral phonon temperature and local nonequilibrium in thin films and across interfaces. *Physical Review B*, 95(19):1–13, 2017.

VITA

## VITA

Jingjing Shi obtained her B.S. degree from the School of Aerospace of Tsinghua University, Beijing, China, in 2012. Currently she is a graduate research assistant in the Nanoscale Energy Transport and Conversion Lab at Purdue University, West Lafayette, USA. She is pursuing Ph.D. degree in Mechanical Engineering at Purdue University, West Lafayette, USA. Her primary research interest lies in energy transport across interfaces for thermal applications, and developing theoretical and computational approaches to model and simulate thermal transport processes in nanostructures.